

Optimization of 3D+t Light Sheet Fluorescence Microscopy and its Application to the Study of Cellular Dynamics

Zur Erlangung des akademischen Grades eines

DOKTORS DER INGENIEURWISSENSCHAFTEN
(Dr.-Ing.)

von der KIT-Fakultät für
Elektrotechnik und Informationstechnik des
Karlsruher Instituts für Technologie (KIT)
angenommene

DISSERTATION

von
M. Sc. Hao Jia
geb. in Shanxi, P.R.China

Tag der mündlichen Prüfung: 6.6.2023

Hauptreferent: Prof. Dr. Uli Lemmer

Korreferent: Prof. Dr. Gerd Ulrich Nienhaus



This document is licensed under a Creative Commons
Attribution-NonCommercial-ShareAlike 4.0 International License (CC BY-NC-SA 4.0):
<https://creativecommons.org/licenses/by-nc-sa/4.0/deed.en>

Contents

1	Introduction	1
1.1	Introduction	1
1.2	Thesis outline	2
2	Theory	3
2.1	Fluorescence	3
2.1.1	Light and matter interaction	3
2.1.2	State evolution in time	4
2.1.3	Spontaneous emission	6
2.2	Microscopy	10
2.2.1	Principle of microscopy	10
2.2.2	Fluorescence microscopy	14
2.2.3	Single plane illumination microscopy	15
2.2.4	Single molecule localization microscopy	22
2.3	Fluorophores	28
2.3.1	Fluorescent proteins	28
2.3.2	Organic dyes	29
3	Methods and materials	35
3.1	The focal field	35
3.2	Optimization of the lattice light sheet	37
3.3	Experimental implementation	40
3.3.1	Wave front engineering	40
3.3.2	Phase mask designing	41
3.3.3	Experimental setup	42
3.3.4	Control strategy	45
3.3.5	Setup alignment	46
3.3.6	Environmental chamber	51
3.4	Microscope characterization	54
3.4.1	Stability evaluation	54
3.4.2	PSF evaluation	57
3.5	SMLM algorithms	60

3.5.1	sCMOS camera pixel reading model	60
3.5.2	Global segmentation algorithm	65
3.5.3	Global single molecule fitting algorithm	72
3.5.4	Simulation results of global fitting algorithm	79
3.6	Software implementation	82
3.6.1	Post-processing features for SPIM data	82
3.6.2	Segmentation features for SMLM data	83
3.6.3	GPU accelerated fitter	85
3.7	Sample preparation	87
3.7.1	Sample insert	87
3.7.2	Coverslip pre-treating	88
3.7.3	Dye sample in PDMS microchannel	89
3.7.4	Fixed beads sample	89
3.7.5	Imaging buffer	91
3.7.6	Transfection and staining	92
3.7.7	Cell fixation and immunolabeling	94
4	Applications	97
4.1	Time-lapse imaging of Wnt signaling	97
4.1.1	Background of Wnt signaling	97
4.1.2	Results of Wnt signaling measurement	98
4.2	Uptake of surface-modified nanoparticles	101
4.2.1	Background	101
4.2.2	Hard protein corona formation and characterization	102
4.2.3	Time-lapse imaging	104
4.2.4	Discussion	107
4.3	Imaging of microtubules	107
4.3.1	Localization precision examination	108
4.3.2	Piezo stage movement modeling	112
4.3.3	Data correction pipeline	115
4.3.4	Visualization and evaluation of the 3D reconstruction of the microtubules	116
4.3.5	Discussion and conclusion	120
5	Summary and outlook	123
5.1	Summary	123
5.2	Outlook	124
	Appendix	127
	List of Abbreviations	131
	Acknowledgements	147

Dedicated to Jinwen and Shujing...

Chapter 1

Introduction

1.1 Introduction

Seeing is believing is a central tenet in biology when it comes to the study of microscopic organisms since the microscope's debut. Over the last two decades, the blooming progress of microscopy technologies in concert with data science and advanced chemical and gene engineering methods has reshaped the biological research paradigms, heralding a new era of interdisciplinary research in a wide spectrum of the life sciences ranging from determining the intricate conformations of biomolecules with atomic precision [1] to the macroscopic domain such as investigating embryo development of a whole organism in real-time [2, 3].

Light microscopes, by virtue of their non-invasive and easily accessible properties, are widely found in modern biology laboratories. As an indispensable member of the light microscope family, fluorescence microscopy renders extraordinary contrast to the structure of interest tagged with biocompatible fluorophores in live organisms by using generalized labeling techniques.

Since life emerged in a 4D space-time in itself, observing biological activities in the matched dimensions is necessary for better understanding the essence of life. Selective plane illumination microscopy (SPIM) is a powerful fluorescence microscopy technique enabling 3D imaging with high spatio-temporal resolution while minimizing photobleaching and phototoxicity compared to its peers. Shortly after its birth, SPIM became ubiquitous in a diversity of life science research fields such as resolving subcellular dynamics in cell biology [4, 5], investigating the interaction between cells in immunology and oncology [6, 7], whole-brain profiling and functional imaging in neuroscience [8–12], modeling whole-embryo evolutionary patterns in developmental biology [3, 13] as well as quantitatively analyzing tissues in histopathology [14–16]. Despite its recognized power and comprehensive capabilities in the outlined fields, SPIM cannot resolve fine structures below a hundred nanometers due to the diffractive nature of light.

Single molecule localization microscopy (SMLM) is an epochal invention in

that it allows fluorescence light microscopy being able to resolve structures of nanometer scale, which was believed achievable only with electron microscopes. Biologists are capable of studying the dynamics of biomolecules [17], resolving subcellular structures [18, 19] and examining their interactions even in live cells [20, 21].

New biological findings are always boosted by the invention of new observation techniques. To answer the ultimate question of how the genome shapes what we are and regulates our physiological activities, a unified microscope with multi-modalities that simultaneously meets the observation requirements at varying scales needs to be built. In this regard, the combination of SPIM and SMLM is a pioneer [22], potentially bridging the gap between molecular biology and cell biology. Because of the lack of awareness and technical difficulties, this attempt is in stagnation. The most relevant work published recently reported the plasma membrane receptor map on a whole cell by using state-of-art SPIM equipment and advanced SMLM algorithm although the resolution is unsatisfactory [23].

1.2 Thesis outline

In this thesis, I will further the fusion of the nascent SPIM and SMLM techniques and show the superior performance and versatility of our homemade microscope through several biological applications. The thesis is organized into five chapters. In the second chapter, the foundation of the fluorescence microscope including the physical background of fluorescence, the general and specific principles for different microscopes and the basis of various fluorophores are introduced. The third chapter contains the methods and materials used in my work. The optimization and implementation of a homemade lattice light sheet microscope as well as SMLM algorithms based on the established setup comprise the main sections of this chapter. In the remainder of this chapter are introductions to software developed for this microscope and sample preparation protocols. The results for time-lapse imaging of Wnt signaling and uptake kinetics of surface-modified nanoparticles by live cells are shown in the fourth chapter to demonstrate the high spatio-temporal resolution of the SPIM modality. Imaging of microtubules serving as a proof-of-principle experiment for the proposed SMLM algorithms can be found at the end of this chapter. The fifth chapter concludes the presented methods and results and gives a perspective on possible applications in biological research.

Chapter 2

Theory

2.1 Fluorescence

2.1.1 Light and matter interaction

In the context of quantum mechanics, the probability of finding an electron in space is depicted by the modular square of its wave function. An electron bound to a proton can be described with a family of orthogonal wave functions known as orbitals of the hydrogen atom. In which orbital the electron resides depends on the energy of the nuclear-electron system. A necessary condition allowing for a transition between orbitals is the energy difference of the concerned electronic states being equal to that carried by the photon absorbed or emitted during the transition.

Although the orbital wavefunction of organic molecules, specifically fluorophores involved in this thesis, do not have an analytical solution as opposed to the hydrogen atom, a linear combination of the entire set of eigenfunctions of the hydrogen atom can in principle approximate the molecular orbitals of interest, which are typically the highest occupied molecular orbital (HOMO) and the lowest unoccupied molecular orbital (LUMO). In the light-matter interaction process, the electron residing in the HOMO or ground state will be promoted by absorbing a photon to the LUMO or excited state and vice versa. For instance, the electronic orbital of the π bond, which is a typical covalent chemical bond occurring in fluorophores, can be represented by the sum of atomic $2p_z$ orbitals of N carbon atoms contributing to the bond

$$\psi_{\pi}(\mathbf{x}) = \sum_{n=1}^N C_n \psi_{2p_z}^n(\mathbf{x}, \mathbf{X}_n), \quad (2.1)$$

where \mathbf{X}_n denotes the coordinate of n^{th} carbon nucleus.

If two electrons are found in the HOMO, the orbital wavefunction must include both electrons not only because the transition could occur on any of the electrons but also because the spins, $|+\rangle$ for spin $+1/2$ and $|-\rangle$ for spin $-1/2$, of both electrons need to be considered. Most molecules in their ground state have two electron spin states in an antisymmetric configuration, thus the total spin is zero. Such a spin state is known as the singlet state, whereas a symmetric spin configuration leads to the triplet state with a total spin of 1. Transitions between singlet and triplet states are forbidden for the sake of angular momentum conservation unless the intersystem crossing occurs.

Apart from the electronic wavefunction, translation, vibration and rotation of the involved nuclei can also give rise to molecular energy change. Therefore, the complete molecular wavefunction must take into account the nucleus distribution. Since nuclei move much slower than electrons in a molecule, on the timescale of electronic movement, the nuclear position can be viewed as a static parameter in the electronic wavefunction. On the contrary, the nuclear wavefunction does not rely on the transient electron position but on the average electron cloud, *i.e.*, the electronic wavefunction. This assumption leads to the Born-Oppenheimer approximation, which allows for solving the Schrödinger equation for electron and nucleus separately. It is reasonable to write the complete molecular wavefunction in position space, given that the transition process has an appreciable effect merely on both the HOMO and LUMO and pertinent atoms,

$$\Psi_{i,n}(\mathbf{x}, \mathbf{X}) = \psi_i(\mathbf{x})\chi_{n(i)}(\mathbf{X}). \quad (2.2)$$

The subscript of the atomic wavefunction $\chi_{n(i)}$ denotes the n^{th} energy eigenstate conditioned on the i^{th} electronic orbital. One can envision the nucleus in an equilibrium state being balanced under the attractive force of the electron cloud and the repulsive force of the conjugate nuclei. A slight offset will then trigger a restorative force proportional to the displacement to the first-order approximation. Thus the nuclear wavefunction can be formulated as a harmonic oscillator with typical vibrational frequencies varying from 10^{13} Hz to 10^{14} Hz.

2.1.2 State evolution in time

The probability to observe the molecular state $|\Psi_{i',n'}\rangle$ at time t in a time-evolving state initially residing on state $|\Psi_{i,n}\rangle$ and being subjected to a time-dependent potential is denoted by $|c_{i',n'}(t)|^2$. The complex coefficient in the modular bracket is written as

$$c_{i',n'}(t) = \frac{iq_e\omega_{i'i}\mu_{12}}{\hbar} \left[\frac{1 - e^{i(\omega_{12}-\omega)t}}{\omega_{12} - \omega} A + \frac{1 - e^{i(\omega_{12}+\omega)t}}{\omega_{12} + \omega} A^* \right], \quad (2.3)$$

where ω and A are the angular frequency and the complex amplitude of the vector potential of the external field, respectively. And $\omega_{12} = (E_{i',n'} - E_{i,n})/\hbar$, with $E_{i',n'}$ and $E_{i,n}$ being the energy of molecular state $|\Psi_{i',n'}\rangle$ and $|\Psi_{i,n}\rangle$, while $\omega_{ii'} = (E_i - E_{i'})/\hbar$, where E_i and $E_{i'}$ characterize the energy of electronic eigenstate $\psi_i(\mathbf{x})$ and $\psi_{i'}(\mathbf{x})$ alone. The charge of the electron is represented by q_e . The overall transition dipole moment is defined as

$$\mu_{12} = \langle \chi_{n'(i')} | \chi_{n(i)} \rangle \langle \psi_{i'} | x | \psi_i \rangle. \quad (2.4)$$

The amplitude of the second factor is dominated by the selection rule determining if an electronic transition is forbidden according to the symmetry of electronic states along the x direction, to which the polarization of the external field is oriented. As illustrated in Fig. 2.1, the electronic transition re-configures nuclei rest positions, resulting in shifted potential and thus the shifted vibrational wavefunctions in terms of those when the electron resides on the ground state. Consequently, the broken orthogonality of vibrational wavefunctions allows the transition from one vibrational level to another in concert with the electronic transition, the probability of which is described by the Franck-Condon factor $\langle \chi_{n'(i)} | \chi_{n(i)} \rangle$. The hybrid transition process provides a diversity of possible transition pathways as opposed to a one-to-one mapping scheme and thus partly accounts for the continuous absorption spectrum, whose peak corresponds to the maximum Franck-Condon factor, as will be elaborated later.

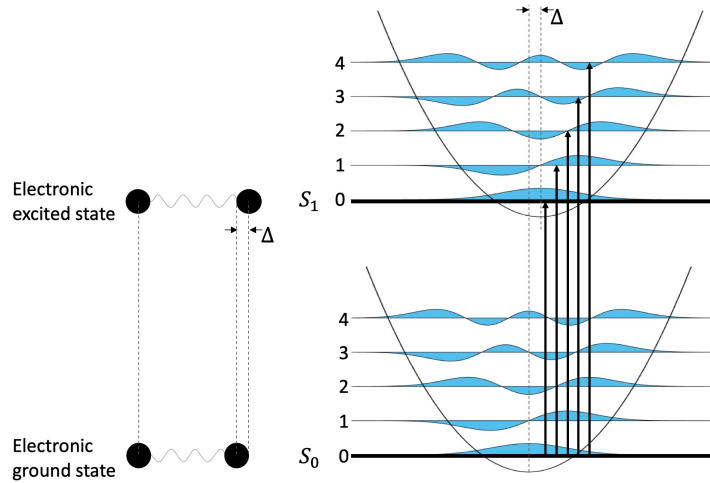


Figure 2.1: Vibrational wavefunctions at different electronic energy levels. The distance between two atoms increases by Δ due to electronic transitions. The vibrational wavefunctions shift by Δ in response, breaking down the orthogonality of harmonic wavefunctions. Therefore transitions from vibrational sublevel 0 to other sublevels are allowed.

Whereas the transition dipole moment gives a necessary condition for allowed transitions, two terms inside the square bracket of Eq. 2.3 oscillate with t and destructively interfere only if the following energy condition is met to render appreciable transition probability,

$$E_{i',n'} \simeq E_{i,n} \pm \hbar\omega. \quad (2.5)$$

The plus and minus signs represent absorption and stimulated emission, respectively. For instance, when absorption occurs, the first term in the bracket of Eq. 2.3 approximately increases as $-iAt$ while the second oscillating term is negligible as far as the transition probability $|c_{i',n'}(t)|^2$ is concerned. Regarding $|c_{i',n'}(t)|^2$ as a function of ω_{12} with parameter $t \rightarrow \infty$, $|c_{i',n'}(t)|^2$ varies as a Dirac delta function multiplied by t , indicating that the initial state transits to a continuum of final states, whose energies center about $E_{i',n'}$ even though the molecule is exposed to a monochromatic field. The phenomenon can be explained by the fact that the Fourier spectrum of a monochromatic wave train exhibits a dispersion during the course of the interaction with its width inversely proportional to the interaction time. This is a special case of the time-energy uncertainty principle.

In light of the state density being the function of energy, the overall transition rate, defined as the transition probability per unit of time, from an initial state $|\Psi_{i,n}\rangle$ to a group of final states similar to $|\Psi_{i',n'}\rangle$ is given by Fermi's golden rule,

$$\omega_{1 \rightarrow [2]} = \frac{2\pi q_e^2 |A|^2 \overline{|\omega_{i'i}\mu_{12}|^2}}{\hbar} \rho(E_{i',n'}) \Big|_{E_{i',n'} \simeq E_{i,n} \pm \hbar\omega}, \quad (2.6)$$

where $\overline{|\omega_{i'i}\mu_{12}|^2}$ represents the average over the vicinity of state $|\Psi_{i,n}\rangle$. One can learn from this relationship that the transition rate is synergically determined by the external field intensity, the dipole moment strength as well as the transition condition Eq. 2.5. For more detailed derivations of formulas in this section, I refer the reader to the book by Sakurai [24] and Parson [25].

2.1.3 Spontaneous emission

In Einstein's theory the transition rate is parameterized as

$$B_{12} = B_{21} = \frac{2\pi q_e^2 |A|^2 \overline{|\omega_{i'i}\mu_{12}|^2}}{\hbar}, \quad (2.7)$$

the unit of which is the probability per unit time per state. Note that only two molecular states are considered here for simplicity. To mediate the conflict

between the biased population distribution under the thermal equilibrium condition and the unmatched numbers of molecules undergoing upward and downward transitions per unit of time depending on the state populations, a spontaneous downward transition process with the parameterized rate of A_{21} in the absence of an external field is proposed,

$$A_{21} = B_{21} \frac{2\hbar n^3 \omega^3}{\pi c^3}, \quad (2.8)$$

where n denotes the refractive index of the medium. This process is also known as the fluorescence process, the parameterized rate of which is proportional to the absorption rate and the cube of the external field frequency.

More formally, spontaneous fluorescence can be described by the quantum theory of matter-light interaction. The total wavefunction incorporating the state of the light field is

$$|\Psi\rangle = |\Psi_{i,n}\rangle \otimes |N_{i,n}\rangle, \quad (2.9)$$

where $|N\rangle$ is the Fock state of the quantized light field. Instead of the quantities reporting on the field amplitudes A and A^* in Eq. 2.3, here they are replaced by annihilation and creation operators a and a^\dagger . The expansion coefficient is rewritten

$$\begin{aligned} c_{i',n'}(t) &= iq_e \omega_{i'i} \mu_{12} \sqrt{\frac{2\pi}{\hbar\omega V}} \left[\frac{1 - e^{i(\omega_{12}-\omega)t}}{\omega_{12} - \omega} \langle N_{i',n'} | a | N_{i,n} \rangle + \frac{1 - e^{i(\omega_{12}+\omega)t}}{\omega_{12} + \omega} \langle N_{i',n'} | a^\dagger | N_{i,n} \rangle \right] \\ &= iq_e \omega_{i'i} \mu_{12} \sqrt{\frac{2\pi N_{i,n}}{\hbar\omega V}} \frac{1 - e^{i(\omega_{12}-\omega)t}}{\omega_{12} - \omega} \langle N_{i',n'} | N_{i,n} - 1 \rangle \\ &\quad + iq_e \omega_{i'i} \mu_{12} \sqrt{\frac{2\pi(N_{i,n} + 1)}{\hbar\omega V}} \frac{1 - e^{i(\omega_{12}+\omega)t}}{\omega_{12} + \omega} \langle N_{i',n'} | N_{i,n} + 1 \rangle \end{aligned} \quad (2.10)$$

where V denotes the volume of the cavity. When absorption occurs, the light field gives up a photon to the molecule such that $N_{i,n} - 1 = N_{i',n'}$. Hence $\langle N_{i',n'} | N_{i,n} - 1 \rangle$ equals 1 while $\langle N_{i',n'} | N_{i,n} = 1 \rangle = 0$, in accordance with the treatment when evaluating the transition probabilities Eq. 2.3 and vice versa. As for the transition rate, one only needs to substitute $2c^2\pi\hbar N_{n,i}/(\omega V)$ (absorption) or $2c^2\pi\hbar(N_{n,i} + 1)/(\omega V)$ (emission) for $|A|^2$ in Eq. 2.6. The dependency of the transition rate on the photon density per unit volume $N_{n,i}/V$ is consistent with the dependency on the light field intensity in the semi-classical theory.

Contrary to the semi-classical theory when the molecule is in vacuum, the second term of Eq. 2.10 could still amount to an appreciable value, predicting the existence of spontaneous fluorescence. Note that, as the external field is

not necessary for spontaneous transition, the downward transition should not be limited to the excited state - ground state transition, meaning a range of different transition pathways are allowed. In practice, under the equilibrium condition, the fluorophore molecule population in the energy level qualifying for stimulated emission is much less than that at the ground level. The stimulated emission is then negligible relative to other downward transition pathways, as illustrated in the Jablonski diagram.

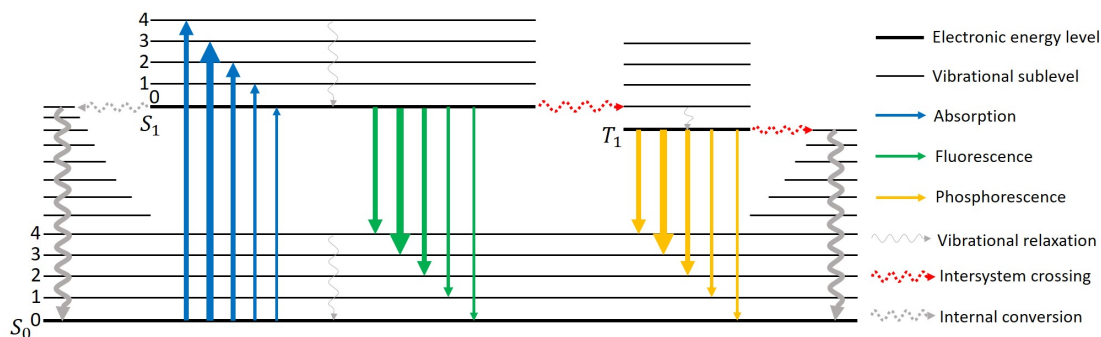


Figure 2.2: Jablonski diagram. The radiative transition probability is encoded in the thickness of straight arrows. S_0 , S_1 and T_0 represent singlet ground state, singlet excited state and triplet excited state, respectively.

Upward transitions from the vibrational ground state 0-electronic ground state S_0 to the combination of the first excited electronic state S_1 and a set of vibrational states 0 – 4 as labeled by blue arrows in Fig. 2.2 have to be mediated by an external field with the condition Eq. 2.5 met. The absorption process occurs within 10^{-15} s, in which the nuclei re-configuration and electronic transition can be considered to occur simultaneously. Populations of vibrational sublevels are jointly decided by the state density, the spectral density of the external field and the Franck-Condon factor.

As for downward transitions, the vibrational state and electronic state have to be treated separately since the former features a shorter lifetime ($10^{-12} - 10^{-10}$ s) compared to the latter one ($10^{-10} - 10^{-7}$ s). This discrepancy can be explained by the time-energy uncertainty principle asserting that the product of a superposition state's decoherence time or decay time with the width of its energy density spectrum should be around \hbar . As the local vibrational states are characterized by a group of uniformly spaced energy levels populated according to transition rate, they will rapidly relax to the equilibrium state, typically the vibrational ground state in the form of non-radiative relaxation marked by the solid grey wavy arrows in Fig. 2.2. By the symmetry of the Franck-Condon factor the electronic downward transitions from $S_1 - 0$ state will populate the vibrational states in the same way as with the upward transition and emit fluorescence photons labeled with green arrows. Because of the symmetry in vibrational states, the absorption

and emission spectra of a molecule are not single lines but extended curves that are mutually mirrored. The distance between two peaks is called the Stokes shift.

Another mechanism, known as the dynamic Stokes shift[26], accounting for a significant part of the Stokes shift is the polar solvent reorientation induced energy variance to the fluorophore molecule. A fluorophore in the ground state (S_0) labeled in light green in Fig. 2.3 has its surrounding solvent molecules oriented to minimize the system energy. As with vibrational decay occurring right after excitation, polar solvent molecules lower the overall energy from S_1^* to S_1 by adapting orientation to the dipole moment direction. Once again, the fluorescence emission occurs prior to solvent molecule re-orientation from S_0^* to S_0 state.

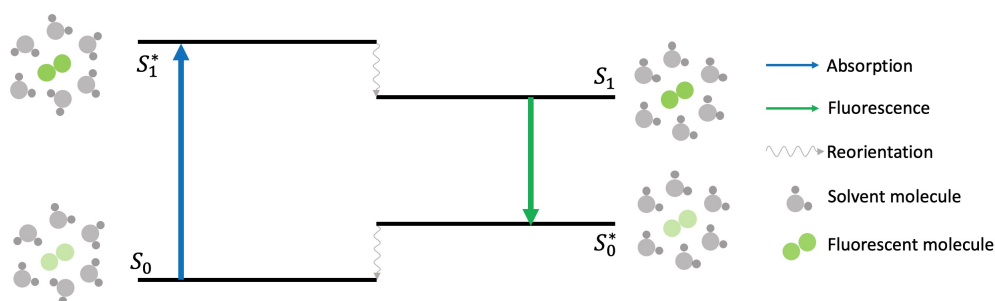


Figure 2.3: Dynamic Stokes shift diagram. Fluorophore molecules in the ground and excited states are labeled in light and dark green, respectively. Energy levels marked with an asterisk represent solvent molecule unstable states.

Notably, electronic transitions are allowed only if the involved states are both singlet or triplet to conserve angular momentum unless intersystem crossing occurs, such as spin-orbit coupling and angular momentum exchange with ambient molecules. In those cases, the system can transit from the excited singlet state to the excited triplet state T_1 , remaining in the state for an extended time of up to 10 s before transiting to the S_0 state by emitting phosphorescence. The triplet state is involved in photobleaching as its intersystem crossing with oxygen in the triplet ground state turns the latter into an excited singlet state, one form of a reactive oxygen species, that will oxidize fluorophore molecules in the excited singlet state and permanently form non-fluorescent products.

Alternatively, the excited electron can internally convert to a high vibrational sublevel of the ground state without losing energy and decay to the $S_0 - 0$ state in a non-radiative way. All of the outlined transition pathways compete with the fluorescence pathway, leading to a decreased fluorescence quantum yield (QY)

$$\eta_{\text{fluo}} = \frac{k_{\text{fluo}}}{k_{\text{fluo}} + k_{\text{isc}} + k_{\text{ic}} + \dots}, \quad (2.11)$$

where k_{fluo} , k_{isc} and k_{ic} are rate coefficients for fluorescence, intersystem crossing and internal conversion, respectively.

2.2 Microscopy

2.2.1 Principle of microscopy

Historically, a microscope refers to an apparatus constructed from a set of optical lenses that magnifies microscopic objects the naked eye cannot see. The last decades have witnessed the blooming of microscopy techniques, among which scanning tunneling microscopy [27] and cryogenic electron microscopy [28] stand out in their sublime resolution on the atomic scale. However, those techniques are too destructive for tasks involving live cell measurements.

In virtue of its non-invasive and bio-compatible properties, the optical microscope is the most prevalent technique for biological studies such as the investigation of morphological change in the developing embryo and intra- and extracellular signaling. In this thesis, I will concern myself with the optical microscope.

A modern optical microscope is an infinity-corrected optical system schematically shown in Fig. 2.4. By infinity-corrected, the image of the object at the focal plane of the objective lens is infinitely far away from the objective lens. From the geometric optics perspective, divergent light rays emitted from an arbitrary point source on the object are converted to parallel rays after propagating through the objective lens. A tube lens freely positioned along the optical axis focuses the parallel rays at its back focal plane. Compared to the object, the coordinate of each refocused point scales up by a factor of the focal length ratio of f_2 to f_1 , reflecting the magnification rate of f_2/f_1 . This arrangement leaves ample space between the objective and tube lenses, allowing for inserting filters or wavefront engineering elements without substantially changing the parallelly propagating rays.

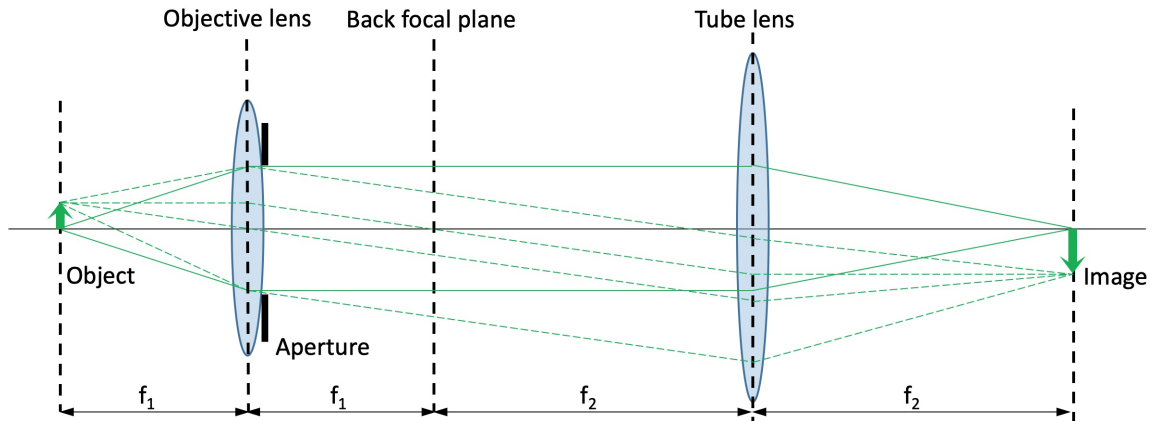


Figure 2.4: Schematic of an infinity-corrected optical system. The object located at the front focal plane of the objective lens, which is equivalent to a single lens confocal with the tube lens, is imaged on the back focal plane of the tube lens. The light rays emitted from the object are clipped by the aperture of the detection objective lens.

The simple relationship between magnification rate and focal length ratio does not imply an infinitely resolvable structure given an unlimited focal length ratio. This is because an imaged point source does not appear as an ideal point, but rather an extended spot called the point spread function (PSF). The extent to which the PSF spreads out depends on both the back focal aperture size and the focal length of the objective lens. In the classical electromagnetic field theory, this phenomenon is the diffractive nature of a clipped electromagnetic wave.

Representing the parallel rays with a plane wave multiplied by a circular aperture function and omitting the polarization and the time-dependent factor, the resulting electromagnetic field is a constant value with a circular area as shown in Fig. 2.5. According to Fresnel's paraxial approximation[29], the field at the focal plane of the objective lens is the Fourier transform of the incident field

$$\begin{aligned} E_{\parallel}(\rho) &= \iint_{S_{\parallel}} \exp(i2\pi r \cos\varphi \cdot n \frac{\rho}{\lambda f_1}) r dr d\varphi \\ &= 2\pi r_0^2 \frac{J_1(k\rho NA)}{k\rho NA}, \end{aligned} \quad (2.12)$$

where (r, φ) and (ρ, ϕ) are coordinates of the back focal aperture (BFA) and the focal plane of the objective lens, respectively. r_0 is the aperture radius and n denotes the refractive index of the medium, in which the light travels. Wavevector k is defined as $2\pi/\lambda$, where λ is the wavelength. J_1 is the first order Bessel function of the first kind. The numerical aperture NA contains physical information of the objective lens in one quantity such that $NA = n\sin\theta_0$ with θ_0 being the maximum angle of the light ray to the optical axis. The second equality is derived using identities for Bessel functions, $\int_0^x \xi J_0(\xi) d\xi = xJ_1(x)$ and $J_0(x) = \frac{1}{2\pi} \int_0^{2\pi} \exp(ix\cos\varphi) d\varphi$.

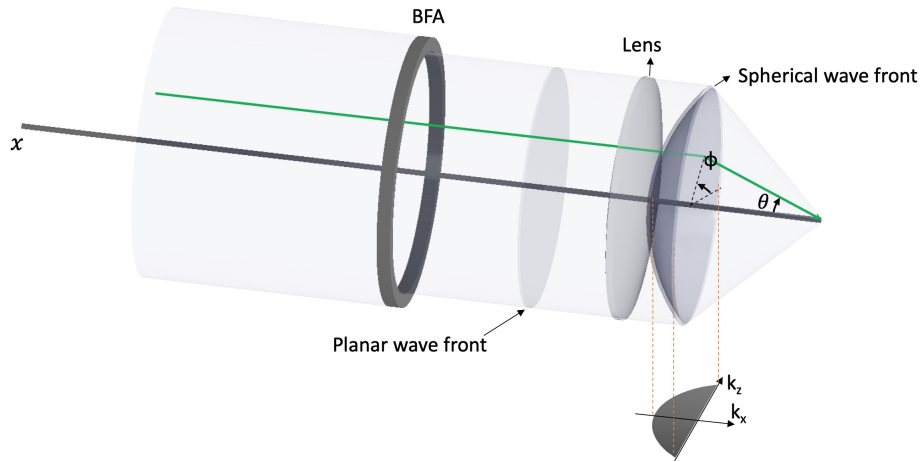


Figure 2.5: Propagating and focusing of a clipped plane wave. The light propagates along the x axis.

Considering the incoherence of the fluorescence light, the PSF takes the modular square of Eq. 2.12, known as the Airy disk. The resolution limit is defined as the minimal distance between two adjacent PSFs that can be discerned from each other. In this regard, the most commonly used Rayleigh criterion asserts that the peak-to-peak distance of two Airy disks is the resolution limit when one peak of the Airy disk is aligned to the first valley of the other Airy disk as shown in Fig. 2.6. One can relate NA and λ to the lateral resolution limit ρ_{lim} by straightforward arithmetic calculation

$$\rho_{\text{lim}} = 0.61 \frac{\lambda}{NA}. \quad (2.13)$$

Either decreasing λ or increasing NA can thus improve the lateral resolution.

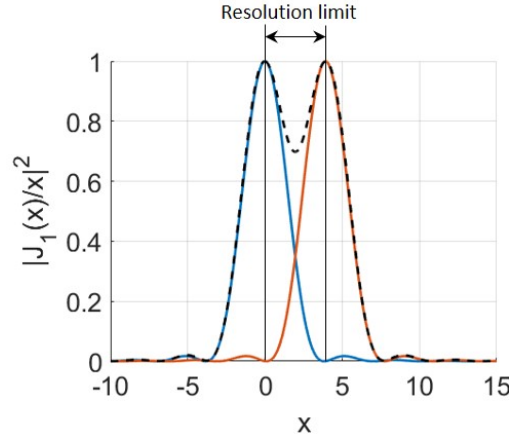


Figure 2.6: Illustration of the Rayleigh criterion.

Essentially, the PSF is constructed from the interference of all allowed plane wave components with varying k , which expands to a part of a continuous spherical surface as shown in Fig. 2.5. In this sense, the 3D PSF can be presented by the integral of plane waves over the 2D hypersurface in k space, or in mathematical language, by the Fourier transform of the 2D hypersurface. Indeed Eq. 2.12 in Cartesian coordinate is obtained by setting z to zero and integrating over k_x and k_y . Similarly, setting y to zeros and integrating over k_x and k_z gives the axial plane representation of the PSF

$$E_{\perp}(x, z) = \iint_{S_{\perp}} \mp \frac{2k_z}{\sqrt{k^2 - k_x^2 - k_z^2}} \exp[i(k_x x + k_z z)] dk_x dk_z. \quad (2.14)$$

The integrating area S_{\perp} is the projection of the spherical shell onto the $k_x k_z$ plane, as shown in Fig. 2.5. The coordinate of wavevector space k_y and k_z are mapped

to the real space Cartesian coordinate y_0 and z_0 at BFA such that $ky_0/f_1 \approx k_y$ and $kz_0/f_1 \approx k_z$. Therefore $k_x = \sqrt{k^2 - k_y^2 - k_z^2}$. Although this integral does not have an analytical expression, it is useful in calculating the PSF intensity distribution in the axial plane for any given aperture function.

An alternative way to evaluate the axial resolution is using the uncertainty principle between the momentum and position of the photon

$$\langle(\Delta x)^2\rangle\langle(\Delta p_x)^2\rangle \geq \frac{1}{4}|\langle[x, p_x]\rangle|^2 = \frac{\hbar^2}{4}, \quad (2.15)$$

where $\langle\cdot\rangle$ presents the ensemble average. Measurement of the position for an ensemble of photons is realized by focusing them to a point. The PSF can then be understood as the uncertainty of the measured position. Sticking to the assumption made before that the photons are uniformly distributed over a spherical surface in k space, which is related to the momentum by the De Broglie equation $p = \hbar k$, $\langle(\Delta p_z)^2\rangle$ is written as

$$\begin{aligned} \langle(\Delta p_z)^2\rangle &= \langle p_z^2 \rangle - \langle p_z \rangle^2 \\ &= \hbar^2 k^2 \int_0^{2\pi} \int_0^{\theta_0} \frac{\cos^2\theta \sin\theta}{2\pi(1 - \cos\theta_0)} d\theta d\phi \\ &\quad - \left[\hbar k \int_0^{2\pi} \int_0^{\theta_0} \frac{\cos\theta \sin\theta}{2\pi(1 - \cos\theta_0)} d\theta d\phi \right]^2, \end{aligned} \quad (2.16)$$

where the probability density per unit solid angle is $1/2\pi(1 - \cos\theta_0)$. Substituting this result into Eq. 2.15 yields

$$\sqrt{\langle(\Delta z)^2\rangle} \geq \frac{\hbar}{2} / \sqrt{\langle(\Delta p_z)^2\rangle} = \frac{\sqrt{3}\lambda}{2\pi \left(n - \sqrt{n^2 - \text{NA}^2} \right)} \quad (2.17)$$

The lateral momentum uncertainty is given by

$$\begin{aligned} \langle(\Delta p_x)^2\rangle &= \langle p_x^2 \rangle - \langle p_x \rangle^2 \\ &= \hbar^2 k^2 \int_0^{2\pi} \int_0^{\theta_0} \frac{\sin^3\theta \cos^2\phi}{2\pi(1 - \cos\theta_0)} d\theta d\phi. \end{aligned} \quad (2.18)$$

Hence the radial position uncertainty evaluates to

$$\begin{aligned} \sqrt{\langle(\Delta \rho)^2\rangle} &\geq \frac{\sqrt{2}\hbar}{2} / \sqrt{\langle(\Delta p_x)^2\rangle} = \frac{\sqrt{2}\lambda}{4\pi n \sqrt{1 - \frac{1}{3}(\cos^2\theta_0 + \cos\theta_0 + 1)}} \\ &\approx \frac{\lambda}{2\pi \text{NA}}, \end{aligned} \quad (2.19)$$

where $\cos\theta_0 = \sqrt{1 - \sin^2\theta_0} \approx 1 - \sin^2\theta_0/2$. This result is equivalent to the Rayleigh criterion (Eq.2.13) only to a constant scaling factor, which is reasonable because different standards are employed in the definition of the resolution.

2.2.2 Fluorescence microscopy

As an indispensable member of the optical microscope family, the fluorescence microscope detects fluorescence emitted from the sample. Illumination light, typically monochromatic laser light, is introduced to the specimen to elicit fluorescence light, the wavelength of which is longer than the excitation light due to the Stokes shift and therefore can be separated from the illumination light by a longpass dichroic mirror as shown in Fig. 2.7. The geometry of the excitation and emission light sharing the same objective lens is called epi-illumination design. Fluorescence light passing through the dichroic mirror is further filtered by a bandpass filter matched to the fluorophore's emission spectrum before propagating to the camera. Two filters, together with an epi-illumination geometry, confer a fluorescence microscope with remarkably high signal-to-noise (SNR) and contrast compared to other optical microscopes that generate images out of the reflected or scattered light from the specimen.

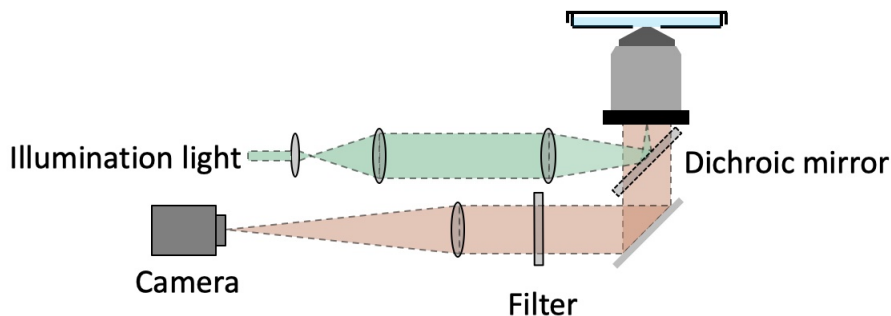


Figure 2.7: Schematic of a fluorescence microscope in the epi-illumination geometry.

In general, the structures of interest in wild-type biological samples do not exhibit natural fluorescence. If anything, the autofluorescence originated from the extracellular matrix [30] or amino acids like tryptophan, tyrosine, and phenylalanine[31], which are ubiquitous in large molecules comprising the organism, is non-specific and can not be leveraged for targeted imaging. Therefore exogenous fluorophores have to be introduced to specifically label the structures. A diversity of labeling techniques varying from conventional methods such as fluorescent protein (FP) transfection and immunofluorescence to recently emerged DNA-PAINT [32], SNAP [33], and aptamer [34] render biologists flexible experimental design. Apart from that, customized excitation/emission spectrum and the Stokes shift

of fluorophores in combination with proper filter sets allow for simultaneous multichannel measurements, which is especially useful for the investigation of the interactions of multiple functional structures in live cells.

It is worthwhile to note that the excitation and emission spectra for a candidate fluorophore marker should reside in the visible window mainly for two reasons. Firstly, because the autofluorescence appears within 300-400 nm, the emission spectrum of the fluorophore marker should be away from this range to avoid crosstalk. More importantly, ultraviolet excitation is devastating for the organism as the energy carried by the photon will directly prompt the covalently bonding electron to the free state and irreversible break constituent molecules. On the other hand, due to the linear dependency on the wavelength of the resolution (Eq. 2.13), the peak of the emission spectrum should not be beyond near-infrared to guarantee a resolution comparable to the scale of the structures to be imaged in the cell. More information about the selection of fluorophores can be found in section 2.3.

2.2.3 Single plane illumination microscopy

Principle

Already in the early 1900s, chemist Richard Zsigmondy invented an apparatus introducing a slit of collimated light to the sample at right angle with respect to the detection axis to study colloidal particles by the scattered light[35]. With the development of fluorescence microscopy and labeling techniques, the orthogonal-plane illumination strategy found its application in optical sectioning microscopy through resolving the three-dimensional structure of a fluorescent dye-stained guinea pig cochlea [36]. What took this geometry in the field of fluorescent microscopy by storm is time-lapse observation of the development of live embryos by SPIM in 2004[37]. Similar to its predecessors, rather than uniformly shining collimated light into the focal plane and collecting fluorescence emission through the same objective lens, SPIM adopts two objective lenses with their optical axes perpendicular to one another. Two objective lenses are arranged in a way that the intersection point of the two axes is the shared focal point where the sample is located, as shown in Fig. 2.8. A thin sheet of light, normally created by either focusing a collimated beam spot through a cylindrical lens[38] or by dithering a thin Gaussian beam[2], is projected onto the sample by the excitation objective lens, while the detection objective lens has its focal plane coincident with the light sheet and collects emitted photons to form an image on the camera sensor located in the focal plane of the tube lens.

Since all photons used to constitute the image exclusively come from the focal plane, background excitation is inherently suppressed and, thus, the signal to background ratio (SBR) and contrast are enhanced. By either scanning the

sample across the light sheet or synchronously scanning the light sheet and the detection objective lens, optical sectioning of the sample can be readily achieved with reduced photobleaching and phototoxicity [39], as each absorption-emission cycle of an excited fluorophore contributes to the focal signal. Therefore SPIM provides an ideal solution to resolve 3D structures compared to other imaging modalities such as confocal microscopy[40], spinning disk microscopy[41] and conventional non-SPIM 3D structured illumination microscopy (SIM) [42], especially in terms of in-vivo imaging of embryonic development of entire organisms, *e.g.*, zebrafish or *Drosophila* over days[43].

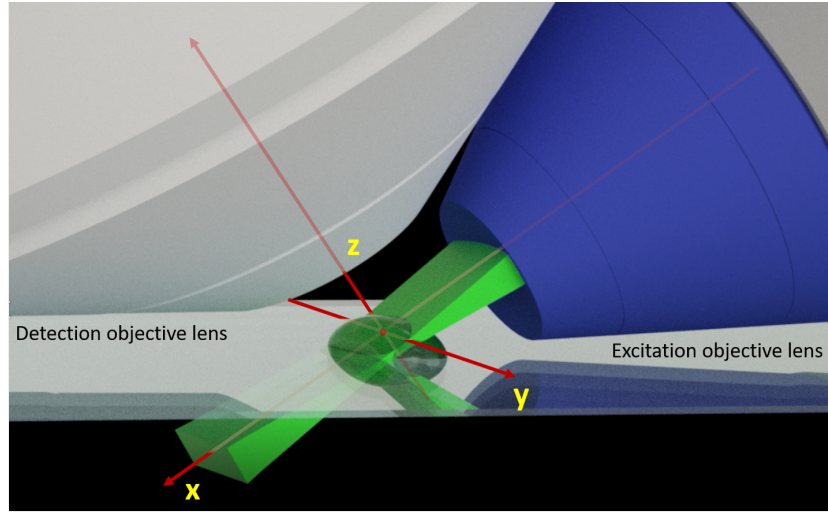


Figure 2.8: selective plane illumination microscope geometry. Light sheet and detection objective lens are synchronously scanned along the z axis. Figure adapted with courtesy from a report by Dr. Petr Pospíšil, 2019.

Furthermore, SPIM substantially improves the axial resolution as a result of the unique geometry with two objective lenses[44]. Consider the fluorescence labeling density on the biological sample as $o(\mathbf{r} - \hat{\mathbf{r}})$, where \mathbf{r} represents the sample space coordinates and $\hat{\mathbf{r}}$ represents the displacement of the sample. For the purpose of explaining the principle of SPIM, a sample is scanned across the fixed light sheet to realize optical sectioning. The object to be imaged by the detection objective lens is

$$o_{\text{fluor}}(\mathbf{r}) = o(\mathbf{r} - \hat{\mathbf{r}}) \cdot \eta \cdot h_{\text{exc}}(\mathbf{r}), \quad (2.20)$$

where η is the QY of the fluorescent molecule multiplied by the detection efficiency and $h_{\text{exc}}(\mathbf{r})$ is the excitation light sheet pattern. In the vicinity of the detection objective focal point the detection point spread function h_{det} is approximately spatially invariant, hence, an optical system can generate a 3D image of an object

at the focal point of the tube lens where the array detector, a scientific complementary metal-oxide semiconductor (sCMOS) camera for instance, is placed. The recorded 2D image in camera space, \mathbf{r}' , is

$$IMA_{3D}(\mathbf{r}') \Big|_{z'=0} = \int (o_{\text{fluo}} * h_{\text{det}}) \cdot \delta(z') dz', \quad (2.21)$$

where $*$ denotes the convolution operation and $\delta(z')$ is the Dirac δ function. Here I define the z axis of the object coordinate system pointing toward the direction that the emission light propagates. For simplicity, I assume h_{exc} to be a function of z , and symmetric with respect to the origin, which is normally the case. Substituting Eq. 2.20 into Eq. 2.21 and using the definition of the convolution operation, one can rewrite Eq. 2.21 in quad integral form. The second equality holds by exchanging the integral order to eliminate the delta function and making use of the symmetry property of the excitation light sheet pattern, $h_{\text{exc}}(z) = h_{\text{exc}}(-z)$. Finally, I re-arrange the terms in triple integral form and again write them in a compact form similar to Eq. 2.21,

$$\begin{aligned} IMA_{3D}(\mathbf{r}') \Big|_{z'=0} &= \int \iiint o(x' - x, y' - y, z' - z + \hat{z}) \cdot \eta \cdot h_{\text{exc}}(z' - z) \cdot \\ &\quad h_{\text{det}}(x, y, z) dx dy dz \cdot \delta(z') dz' \\ &= \iiint o(x' - x, y' - y, -z + \hat{z}) \eta \cdot h_{\text{exc}}(z) h_{\text{det}}(x, y, z) dx dy dz \\ &= \int o(\mathbf{r}' - \hat{\mathbf{r}}) * [h_{\text{exc}}(\mathbf{r}') \cdot h_{\text{det}}(\mathbf{r}')] \cdot \eta \cdot \delta(z') dz'. \end{aligned} \quad (2.22)$$

From Eq. 2.22, one can appreciate that the final image is equivalent to the convolution of a structure labeled with fluorophores and an overall PSF h_{tot} being the product of h_{det} and h_{exc} . For an infinity-corrected detection objective lens, the transverse PSF intensity $h_{\text{det}\parallel}$ is simply the modular square of Eq.2.12. Therefore, the transverse resolution is governed by Rayleigh criterion, Eq.2.13.

The full width at half maximum (FWHM) of the PSF in z direction takes the same form as Eq. 2.17 to a constant scaling factor for consistency with Rayleigh's criterion [45, 46]

$$\text{FWHM}_z = \frac{0.88\lambda_{\text{em}}}{n - \sqrt{n^2 - NA_{\text{det}}^2}}, \quad (2.23)$$

where subscript em and det represent emission and detection, respectively, to distinguish them from excitation (ex). Exemplarily, if the FWHM of $h_{\text{det}\perp}$ is defined as the axial resolution for a $NA = 1.1$ water immersion objective lens at wavelength

515 nm, $h_{\text{det}\perp}$ is 2.7 times as large as $h_{\text{det}\parallel}$. In the SPIM context, due to the perpendicular arrangement of two objective lenses, $h_{\text{eff}\perp}$ is $h_{\text{det}\perp} \cdot h_{\text{exc}\parallel}$. Provided the excitation objective lens has the same NA as the detection objective lens, h_{eff} takes advantage of $h_{\text{exc}\parallel}$ to compress $h_{\text{det}\perp}$ and thus approaching quasi-isotropic 3D resolution.

Unlike the assumption made before that h_{exc} is only a function of z , in practice the light sheet profile along the propagation direction (x axis) varies on the scale depending on the filled BFA size of the excitation objective lens. The effective NA , NA_{eff} , is the product of the nominal NA and the ratio of the beam diameter at the BFA to the diameter of the BFA itself. In wavevector space, NA_{eff} can also be written as the ratio of the wavevector transversal component to k . Given a Gaussian light sheet, if NA_{eff} of the excitation objective lens is small enough that the paraxial approximation condition is valid, h_{exc} can be analytically expressed as the $\text{TEM}_{0,0}$ mode, the simplest form of Hermite-Gauss beams[47], which is one of the solutions of the paraxial Helmholtz equation,

$$E_G(x, y, z) = \frac{E_0}{w(x)} \cdot \exp\left(-\frac{y^2 + z^2}{w(x)^2}\right) \cdot \exp(-i\Phi), \quad (2.24)$$

where $\Phi = kx + \frac{k(y^2+z^2)}{2x(1+(Z_R/x)^2)} - \arctan(x/Z_R)$ and $w(x) = w_0\sqrt{1+(x/Z_R)^2}$. The waist of a Gaussian beam at the focal point is characterized by w_0 as shown in Fig. 2.9. An essential measure to evaluate the uniformity of a Gaussian beam is the Rayleigh length, $Z_R = kw_0^2/2$, which describes the distance to the waist, where the diameter of the beam spot is $\sqrt{2}$ times the waist diameter. For a propagation distance, $x \gg kw_0^2$, the Gaussian beam asymptotically diverges at an angle of $\theta = w_0/Z_R = \frac{\lambda}{\pi w_0}$ is a good metric in terms of the basic optical sectioning performance. A small w_0 yields a higher overall axial resolution by narrowing the Gaussian beam. However, it also leads to an undesired short Rayleigh length and a large divergent angle that in turn compromises the covered field of view (FOV), in which h_{tot} is approximately constant.

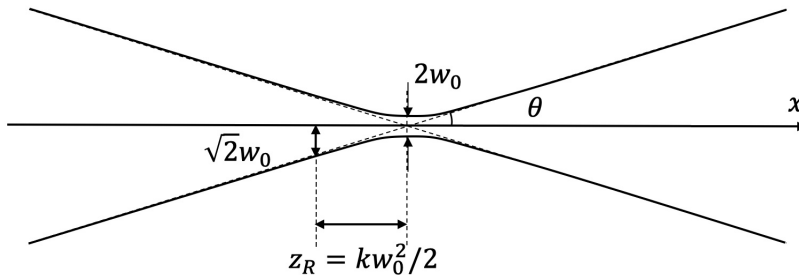


Figure 2.9: Diagram of Gaussian beams.

Diffraction free beam

One way to circumvent the conflict between the covered FOV and the axial resolution is to introduce diffraction-free beams whose transverse modes do not change over the propagation distance [48, 49]. Among those, the Bessel beam is a common choice and typically used in SPIM[50]. It is an analytical solution of the Helmholtz equation in cylindrical coordinates,

$$E_B(r, \phi, x) = J_n(k_{\parallel}r)\exp(in\phi)\exp(ik_{\perp}x), \quad (2.25)$$

where k_{\parallel} and k_{\perp} are the k decompositions in transverse and axial directions with $k_{\parallel}^2 + k_{\perp}^2 = k^2$. The term $J_n(k_{\parallel}r)$ directly shows that h_{\parallel} is independent of axial coordinate x , indicating a globally invariant h_{tot} . To get more insight into the diffraction-free property, one can compute the Fourier transform of its transverse part,

$$\begin{aligned} \tilde{E}_B(k_r, \varphi) &= \mathcal{F}\{J_n(kr)\exp(in\phi)\} \\ &= \frac{2\pi}{i^{-n}}\exp(in\varphi)\delta(k_r - k_{\parallel}). \end{aligned} \quad (2.26)$$

A δ function around the annular line with a radius of k_{\parallel} reveals the essence of a Bessel beam, which is nothing but the interference of plane waves with their wave vectors sharing the same component k_{\perp} . As a result, the common term $\exp(ik_{\perp}x)$ factorizes and then exclusively contributes to the propagation term containing the x argument in Eq. 2.25.

In fact, an ideal diffraction-free Bessel beam requires the superposition of infinitely wide plane waves and therefore does not exist. Experimentally generated Bessel beams will consequently be confined in a rhomboid area with a ratio of axial to transversal diagonal being k_{\perp}/k_{\parallel} , while the rhomboid height is the width of the real plane waves that comprise the Bessel beam, as shown in Fig. 2.10a. An approach to create a plane wave in the laboratory can be found in chapter 3. The reader should bear in mind that all plane waves mentioned in the following text refer to the plane waves confined in a limited lateral area, within which the light field can be expressed by the plane wave solution of the Helmholtz equation. Although a finite Bessel beam transverse range is beneficial with regard to lowering the background excitation, the side lobes of a Bessel beam nevertheless contribute significantly upon scanning. The first side lobe of a Bessel beam accounts for 16% of the main lobe in amplitude, while for a scanned Bessel beam, this ratio is above 50% (Fig. 2.10b-d). Another property that makes the Bessel beam a poor choice compared to a Gaussian beam is its gently dropping slopes flanking the main lobe of the light sheet that give rise to a relatively low axial resolution, high background

excitation, and high photobleaching and phototoxicity when compared to other excitation beams.

Of various methods proposed to address the high background excitation problem, the confocal slit detection strategy has been introduced[51, 52]. This approach makes use of a single line rolling shutter exposure mode of the sCMOS camera to create a virtual slit on the camera sensor, therefore allowing for synchronous scanning of a Bessel beam and exposing pixel rows.

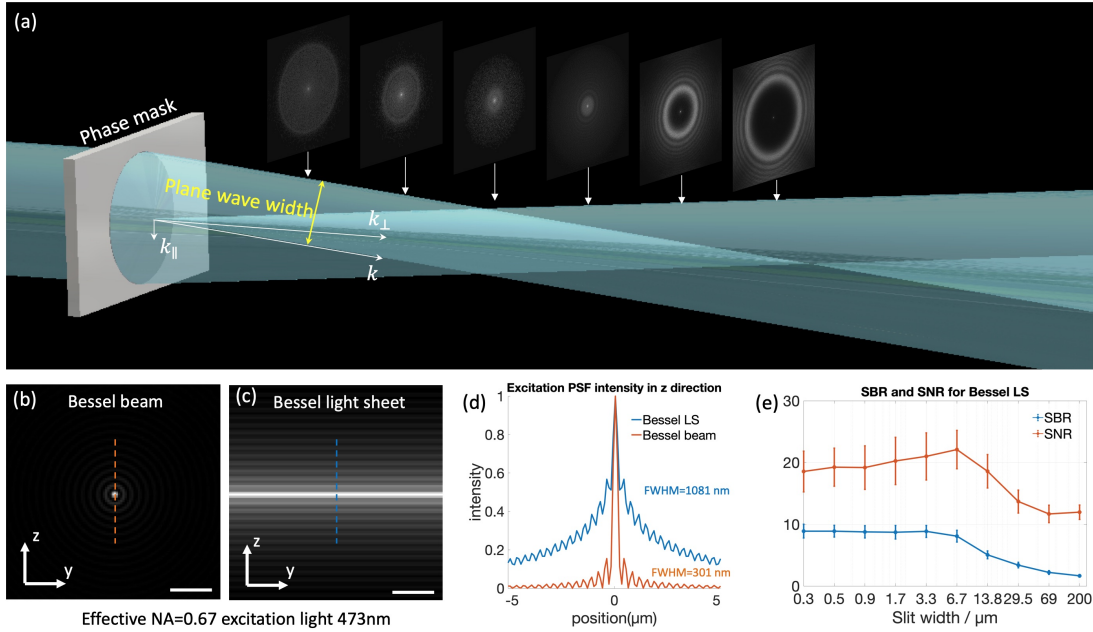


Figure 2.10: Bessel beam properties. (a) Experimentally created Bessel beam by illuminating an axicon phase plate. The Bessel beam is quasi-diffraction-free only within a rhomboid area. (b) Cross-section of an ideal Bessel beam. (c) Cross-section of a scanned Bessel light sheet. Scale bar $2 \mu\text{m}$. (d) Comparison between profiles across Bessel beam and light sheet. (e) Signal-to-noise ratio and signal-to-background ratio of images for a bead sample acquired by synchronously scanning a Bessel beam and using a digital slit on the camera with different slit widths.

I imaged 100 times diluted green-yellow polystyrene beads sample fixed in agarose gel (see section 3.7.4) and evaluated the SNR and SBR for images acquired with different slit widths in confocal slit detection mode. I define the global signal level for an image as the average peak intensity of localized emitters and the background level as the average pixel value of the image with the segmented emitters clipped. The SBR is therefore the ratio of the global signal level to the background level. The SNR is defined as the ratio of the global signal level to the variance of the background pixels.

Theoretically, the narrowest slit results in the best background rejection and the highest resolution improvement. Practically, the thin slit not only rejects the background but also weakens the signal. As suggested in the literature, the optimal slit that maximizes the SNR and SBR is not the narrowest slit [51]. Fig. 2.10e shows that a peak occurs at 6.73 μm slit for SNR, while a plateau appearing at 3.31 μm slit extends all the way to the narrowest slit in terms of the SBR. Further investigation indicates that the different definitions for SNR and SBR lead to distinct peak positions for the same dataset, rendering the calibration of the optimal slit width subjective. In conclusion, high background excitation and the consequent phototoxicity pose a challenge to the application of the Bessel light sheet in SPIM despite its diffraction-free nature.

Optical lattice

Back in 2005, Eric Betzig characterized a series of optical lattices generated from wavevector sets featuring finite elements[53], the microscopic application of which in digital scanned LSM can achieve quasi-isotropic 3D resolution [5]. The general principle is to create a lattice by coherently superimposing a finite number of plane waves with the same k_{\perp} , implying that the lattice is an analogue of the Bessel beam that will not change its shape along the propagation direction. Quite a few distinct lattice patterns are readily determined by selecting a different number of points out of the annular spectrum of the Bessel beam and varying their relative positions on the annulus. Among these, the hexagonal lattice stands out and proved to be the optimal candidate for the excitation light sheet.

The hexagonal lattice consists of six plane waves, whose wavevectors in k space are vertices on a regular hexagon. Rotating this hexagon to align an arbitrary diagonal parallel to the k_z axis, Fig. 2.11 gives analytical expressions of the hexagonal lattice,

$$\begin{aligned} E_{\text{hex}}(x, y, z) &= \sum_{n=1}^{n=6} \exp(i\mathbf{k}_n \cdot \mathbf{r}) \\ &= \left[4 \cos\left(\frac{k_{\parallel}}{2}z\right) \cos\left(\frac{\sqrt{3}k_{\parallel}}{2}y\right) + 2 \cos(k_{\parallel}z) \right] \cdot \exp(ik_{\perp}x) \quad (2.27) \end{aligned}$$

It can be seen that the ideal lattice does not attenuate but instead expands a hexagonal point array periodically to infinite space. As the lattice is a special case of the Bessel beam, it inherits its properties in the experiment implementation. The lattice domain, which is no longer a regular rotating rhomboid as for the Bessel beam but still is similar in shape in the xz plane, can be delineated by the size of plane waves (Fig. 2.11c). In practice, only two to three pairs of side lobes are retained to support the diffraction-free property of the main lobe in a sufficiently large area, for instance, to cover a whole cell to be imaged, while

reducing adverse effects to the largest extent, such as background excitation and photobleaching (Fig. 2.11b and e). A most remarkable feature of the lattice is its high fringe contrast in the axial direction when being scanned, such that the deterioration of axial resolution (axially elongated h_{det}) and SBR due to spherical aberration will be partially canceled out upon multiplication by the lattice light sheet with steep main lobe and deep valleys between the main lobe and first side lobes (Fig. 2.11d-h).

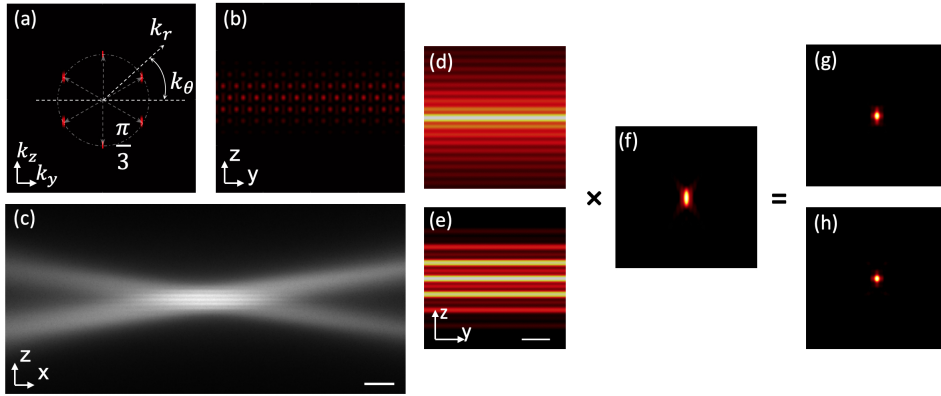


Figure 2.11: Characterization of the lattice beam and comparison between lattice light sheet and Bessel light sheet. (a) Spectrum of a hexagonal lattice. (b) Cross-section of a bound hexagonal lattice. (c) Axial profile of a lattice beam observed in a dye sample. Scale bar 10 μm . (d)-(e) The scanned lattice light sheet (e) presents a high contrast pattern compared to the scanned Bessel light sheet (d). Scale bar 2 μm . (f) The detection PSF in the axial plane. (g)-(h) The overall PSF of the lattice light sheet (h) features higher axial resolution and lower background compared with that of a Bessel light sheet (g). (f)-(g) share the same scale bar with (e).

2.2.4 Single molecule localization microscopy

Introduction to workflow

Despite the high axial resolution of light sheet excitation, SPIM is essentially a diffraction-limited method, the imaging principle of which obeys the convolution law restricting the highest achievable resolution to approximately 300 nm for an objective lens with $NA = 1.1$, while subcellular structures are typical of sub-100 nm scale. Over the past two decades, researchers have developed quite a few techniques devoted to circumventing this resolution limit. Those techniques mainly fall into three categories, stimulated emission depletion (STED) microscopy [54],

SIM [55] and SMLM, among which SMLM and STED are marked with theoretically unlimited resolution enhancement provided that the detected photon number for SMLM or the depletion power for STED is sufficiently high.

In this thesis, I will focus on SMLM, which is, by definition, a method to resolve fine biological structures through localizing the center position of the PSF for individual fluorophores attached to a target of interest to yield precision on the molecular scale. The localization of fluorophores samples the structure of interest, and a super-resolution image can be formed by reconstructing the fluorophore map from the localized coordinates of the fluorophores. However, if all fluorescent probes simultaneously irradiate photons, the acquired raw image will be nothing more than the convolution between the labeled structure and the detection PSF, making it impossible to differentiate PSFs stemming from individual probes (Fig. 2.12). This difficulty is overcome by utilizing emitters featuring an on and an off state, also known as bright and dark states. When an emitter resides in the on state, it can be excited and irradiates the desired fluorescence, whereas the emitter in the dark state is optically inactive.

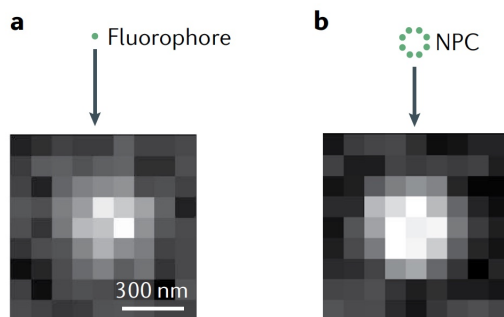


Figure 2.12: Raw wide-field images of a single fluorophore (a) and a nuclear pore complex (NPC) with all labeling fluorophores in the on state simultaneously (b). Adapted from Ref. [56] with permission from Springer Nature, Copyright 2021.

Depending on the mechanisms behind state transitions the most widely used SMLM techniques fall into two categories, photoactivated localization microscopy (PALM)[57] and stochastic optical reconstruction microscopy (STORM) [58]. Photoactivatable fluorophores featured with low fluorescence QY irreversibly switch absorbance spectrum to long wavelengths with enhanced fluorescence QY by at least 100 fold upon light-induced chemical reaction, typically 400-nm light [59]. Both synthetic dyes such as photochromic rhodamine amides [60], the silicon rhodamine PA Janelia Fluor[®] 646 [61] and fluorescent proteins, *e.g.*, PA-GFP [59] can serve as a photoactivatable fluorophore. Instead of being activated to a bright state, photoconvertible fluorophores including EosFP [62, 63] and its relative Dendra2[64] irreversibly switch from a green-emitting to a red-emitting state upon

400-nm light irradiation and, therefore, can be used for PALM as well. In comparison, photoswitchable fluorophores employed in STORM can switch reversibly between dark and bright states for several cycles under certain conditions contingent on specific fluorophores. The underlying blinking mechanism and fluorophore selection will be discussed in the next section.

In practice, the bright state lifetime and conversion or activation rate should be meticulously controlled by chemical or optical means such that, during the course of one exposure, only a subset of the emitter ensemble, in which emitters are spatially sparse and well separated, is in the on state, while the rest of the emitters being in the dark state remain invisible (Fig. 2.13). Each PSF occurring in the raw data is considered to represent one single molecule and thus can be segmented. The localization algorithm is then applied to the segmentation to extract the position information. These imaged emitters will be bleached and a new subset of emitters will be active over time. After thousands of frames of exposure, each probe fluorophore is localized at least once. Eventually, the localizations of those probes are scattered in a coordinate system with continuous axes (Fig. 2.14a) followed by convolution with a virtual PSF, whose FWHM depends on the localization precision contingent on the number of photons per localization. The reconstructed super-resolution image is shown in Fig. 2.14b.

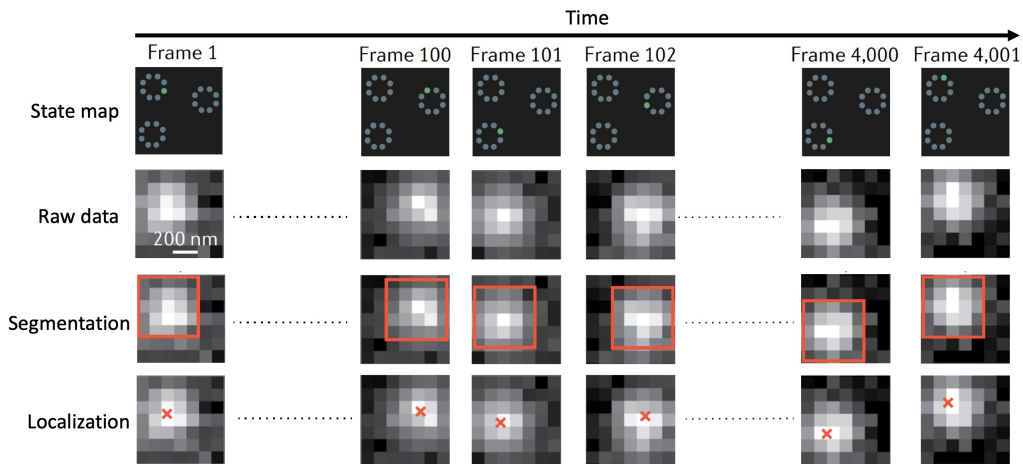


Figure 2.13: The workflow of SMLM. Fluorophores in the on state are marked with bright green dots. Red inserts represent segmented sub-images from the raw data. Crosses in the last row of images denote the corresponding localizations of segmented fluorophores. Adapted from Ref. [56] with permission from Springer Nature, Copyright 2021.

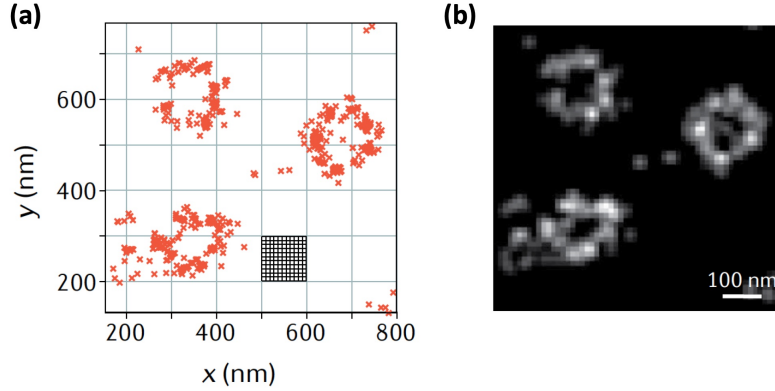


Figure 2.14: The localizations of accumulatively imaged single molecules (a) and the rendered super-resolution image of three NPCs (b). Adapted from Ref. [56] with permission from Springer Nature, Copyright 2021.

Estimation of the theoretical resolution

The localization precision, which defines the variance of a repeatedly localized single emitter, is a key parameter in the field of SMLM as it largely determines the resolution of the reconstructed image. Although the localization precision varies for specific estimators used in practice, the basic law is that the localization precision is inversely proportional to the square root of the detected number of photons. From this law, one can gain insights into the power and limitations of SMLM and thereafter be able to optimize configurations for different tasks.

For conventional fluorescence microscopy, the image of a single molecule is characterized by a PSF, which is, when the number of photons is sufficiently large, well approximated by a Gaussian function with a standard deviation of σ as a measure of resolution and \mathbf{r}_c as a measure of the emitter position. The PSF can be considered as the probability density function describing the chance of finding photons in space. Thus, each recorded photon is actually an independent sample of an observation \mathbf{r}_i taken from this pre-defined distribution. The mean value of samples $\bar{\mathbf{r}}$, which is the centroid of the PSF generated from N photons in SMLM, is an unbiased estimator of \mathbf{r}_c with standard error or uncertainty of σ/\sqrt{N} . Rigorous derivation of the localization position through least-squares fitting analysis of a Gaussian PSF model is given in the literature, where pixelation noise, photon noise as well as background noise are accounted for[65]. The final two-dimensional localization error is written as

$$\langle(\Delta x)^2\rangle = \frac{(\sigma^2 + a^2/12)}{N} + \frac{8\pi \cdot \sigma^4 \cdot bg^2}{a^2 \cdot N^2}, \quad (2.28)$$

where a is the pixel size and bg is the global background noise in units of photon

number. It can be learned from this equation that the background noise induced localization uncertainty decreases faster than $1/N$ and thus becomes negligible when N is much larger than bg . The pixelation noise can also be ignored as long as the pixel size a is much smaller, typically at least 3 times, than the resolution σ , as is the case in conventional fluorescence microscopy where the Nyquist sampling condition is met to achieve a physical resolution limit determined by the NA .

Up to now, I have only talked about localization precision, which is one of the fundamental factors in evaluating the resolution of a reconstructed image. Conventionally, a super-resolution image is rendered by the convolution of the localization scatter plot and a Gaussian PSF with its standard deviation equaling the localization precision to give an intuitive impression of the image resolution in the first place. Notably, all localizations are due to the probes tagged to a structure of interest. This can lead to difficulties in evaluating the resolution, especially when the labeling density is too low to resolve the structure regardless of the high localization precision. More to the point, even though the labeling density might not be an issue, a low sampling rate could also impact the resolution. For brevity, the labeling density is used to describe the resulting reconstructed image and arises from the physical labeling density and the number of frames. A heuristic analysis of the resolution dependency on the labeling density concludes that the image resolution asymptotically approaches the localization precision with increasing labeling density at the cost of temporal resolution[66, 67]. Therefore, filters need to be applied to the reconstructed scattergram to improve the fidelity of the SMLM result when the labeling density is at a modest level.

Fitzgerald *et al.* [68] have introduced an optimal linear filter achieving as low variance as what can be derived from the Cramer-Rao lower bound (CRLB). The fluorescence labeled structure of interest is denoted $o(\mathbf{r})$ and the reconstructed scattergram $d_E(\mathbf{r}) = \sum_{i=1}^M \delta(\mathbf{r} - \hat{\mathbf{r}}_i)$, where M is the total number of detected emitters and $\hat{\mathbf{r}}_i$ represents the estimated i^{th} localization. The continuous form of the expected structure density is then written as $\bar{d}_E = \bar{M}(h_{\text{eff}} * o)$, where h_{eff} is the effective PSF of the SMLM version approximately written as $h_{\text{det}}^{\bar{N}}$, with \bar{N} being the mean photon count of the single localization event. And \bar{M} is the expected number of detected emitters modeled as a Poisson distribution. A frequency-dependent SNR of the expected structure density can then be defined as

$$f(k) =: \frac{|\bar{D}_E(k)|^2}{\text{Var}[D_E(k)]} = \bar{M} \cdot |H_{\text{eff}}(k)|^2 \cdot |O(k)|^2, \quad (2.29)$$

where the capital letters stand for Fourier transforms of the corresponding functions. It can be seen from Eq. 2.29 that the SNR is proportional to the averaged number of emitters \bar{M} , fluorescence labeled specimen spectrum energy density $|O(k)|^2$ as well as the optical transfer function of the SMLM version $|H_{\text{eff}}(k)|^2$. The task is to find the optimal estimation $\hat{o}(\mathbf{r})$ of the real structure information

$o(\mathbf{r})$ from the measured emitter density function $d_E(\mathbf{r})$ with the aid of a filter \hat{g} so that

$$\hat{o} =: \hat{g} * d_E. \quad (2.30)$$

The optimal filter takes into consideration the labeling density, the localization precision and the SNR, and is formulated in the frequency domain as

$$\hat{G}_{\langle |O|^2 \rangle}(k) = \frac{1}{\bar{M}_{\text{eff}}(k) H_{\text{eff}}(k) (1 + \langle f(k) \rangle^{-1})}, \quad (2.31)$$

where $\langle \cdot \rangle$ represents the ensemble average and $\bar{M}_{\text{eff}}(k) =: \langle \bar{M} |O(k)|^2 \rangle / \langle |O(k)|^2 \rangle$. It reduces to a simple deconvolution filter for sufficiently high SNR within the concerned frequency range, while for sparse labeling, the filter takes the form $\langle |O|^2 \rangle H_{\text{eff}}^*$. Heterogeneous modulation of the true specimen spectrum of the filter naturally leads to a metric to quantify the ability of SMLM to resolve the fine structure under a specific experimental configuration. The cutoff frequency is defined as

$$k_M =: \min \left\{ k | \bar{M} \leq \frac{\beta}{|H_{\text{eff}}(k)|^2 \langle |O(k)|^2 \rangle} \right\}, \quad (2.32)$$

beyond which the SNR drops below the chosen value of β . This metric has a profound significance as it quantitatively sheds light on how the labeling density, localization precision and specimen features affect the resolution in a joint way. Hence it can guide the selection of imaging parameters such as the number of frames, the exposure time and the labeling fluorophores, *etc.*, provided a certain resolution is required. It is worth noting that the filter needs a priori information of the specimen, meaning $O(k)$ is iteratively computed with an initial estimation of $D_E(k)/M$.

Principle of 3D SMLM

Since data analysis underlies SMLM, over the last decade, a wealth of algorithms were developed to improve the localization precision, the computational efficiency and to expand the covered FOV [69–74]. The most remarkable progress can be appreciated in the field of three-dimensional localization techniques, whose basic idea is employing wavefront engineering techniques to encode depth information in the shape of the image of a detected emitter. Fitting a unique emitter pattern to an axially asymmetric 3D PSF model can resolve the axial position of the emitter. The mainstream 3D localization methods are all based on this principle, either by introducing astigmatism aberration into the detection PSF [75, 76] or by

modulating the detection PSF to a designed pattern such as a double helix [77] or a tetrapod [78].

Technically, the complex PSF patterns carry more information and will thus provide higher localization precision. However, resolving sophisticated patterns in a diffraction-limited system requires a larger PSF while the photon budget per photoswitching event is limited, implying less photon quota per pixel and hence low SNR. As the simplest asymmetric pattern, PSF with astigmatism aberration exhibits superior efficiency in photon utilization and will be used in my experiment.

2.3 Fluorophores

2.3.1 Fluorescent proteins

Fluorophores for labeling are an essential constituent in fluorescence microscopy. The rule of thumb for a properly selected type of fluorophore is a high absorption cross-section to avoid high excitation power induced phototoxicity and high QY. Apart from that, specific requirements are imposed on different measurement conditions. For live cell imaging, a prime consideration is that fluorophores should be non-invasive and biocompatible to minimize interference and disturbance to the cell. FPs are the most commonly used tags in live cell labeling, as they are endogenously synthesized together with the proteins of interest as a whole.

The wild-type green FP (GFP) was first purified from the jellyfish *Aequorea victoria* and studied by Osamu Shimomura [79]. The gene expressing GFP in jellyfish was cloned and sequenced by Douglas Prasher *et al.*[80] in 1992, followed by recombinant expression in *Escherichia coli* and *Caenorhabditis elegans* [81], demonstrating a novel fluorescence labeling technique. The crystal structure of wild-type GFP reported by the Remington group[82] unveiled the conformation of the GFP molecule being that of a β -barrel with an α -helix running through it. Interactions between the chromophore in the middle of the α -helix and residues on the interior of the barrel influence the energy level structure of the chromophore and hence the spectrum, QY and photostability[83], which can be engineered to produce FP derivatives by modifying those residues through mutagenesis.

Transfection is practiced to introduce genes of fluorescent proteins into eukaryotic cells. In my work, the introduced gene is in the form of a plasmid, a small circular DNA molecule carrying a fusion construct comprising an FP gene concatenated to or inserted within the gene encoding the target protein. The gene coding a protein has two ends corresponding to the free amino acid terminus (N-terminus) and the free carboxyl terminus (C-terminus). The transcription process starts from the N-terminus and ends at the C-terminus. What is known as N-terminal FP construct refers to the plasmid having the C-terminus of the FP gene connected to the N-terminus of the target protein gene via a linker sequence

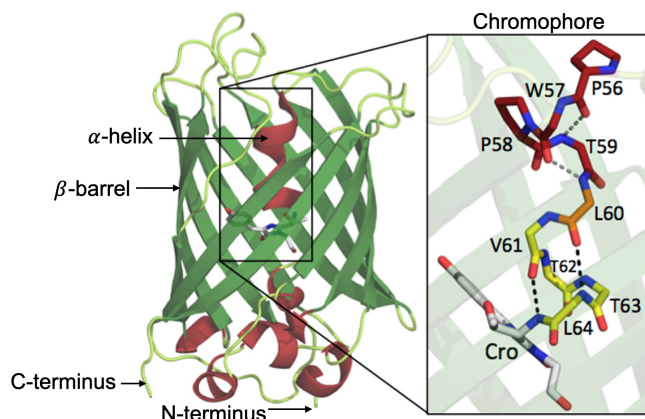


Figure 2.15: Illustration of EGFP crystal structure. Adapted from [84] with permission from PLOS ONE.

to ensure expressed proteins are well separated. The C-terminal FP construct is arranged the other way around. A validated construct will express a properly functioning target protein linked to an FP that fluoresces.

Which tagging strategy should be employed varies from case to case. For instance, secreted proteins or signaling proteins have a short sequence known as signaling peptide preceding the N-terminus of the functioning protein gene. This sequence serves as a tag to determine the destination of the protein in the cell. For many secreted proteins, the signaling peptide will be cleaved off when undergoing modification in the Golgi/ER[85], such as Wnt protein [86]. As a result, the N-terminal FP construct may not work because the FP tagged to the signaling peptide will be degraded. An alternative tagging strategy that works, however, is to insert the FP gene between the signal peptide and the functional protein with two linkers. Apart from construct failure, the protein location within the cell should be taken into account for pH-sensitive FPs[87]. To produce a working plasmid, it is advisable to try out different tagging strategies and check out the functioning of the target protein and FP in vivo and in situ.

2.3.2 Organic dyes

In comparison to photoconvertible FPs, organic dyes are preferably employed in SMLM due to their high photon budget per on-off switching cycle (table. 2.1), rendering considerable localization precision when a short frame exposure time is a major concern for dense structure imaging, where at least hundreds of thousands of frames are needed to reconstruct a super-resolution image. The discrepancy in the number of photons for FPs between the references could originate from different experiment configurations, such as excitation power density, frame exposure time, photon detection efficiency, *etc.* The literature[88] reporting a smaller number of

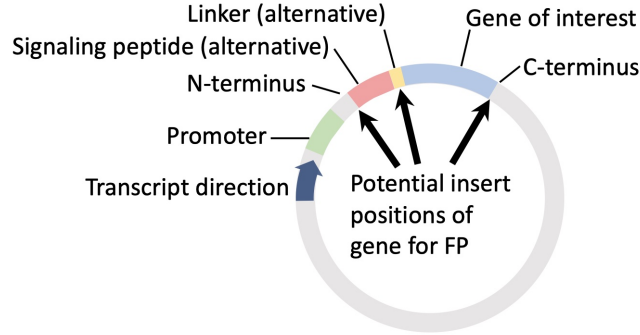


Figure 2.16: Diagram of the plasmid.

photons for Dendra2 and mEos2 also systematically investigated Cy5 and Cy7, whose numbers of photons are consistent with the result in reference [89]. It is reasonable to believe those two groups shared a similar experiment configuration and the comparison between datasets reported by [89] and [88] is fair.

Table 2.1: Switching properties of selected organic dyes and FPs

	$\lambda_{\text{ex}}(\text{nm})$	$\lambda_{\text{em}}(\text{nm})$	$\epsilon(\text{M}^{-1}\text{cm}^{-1})$	QY	duty cycle	No. photons	ref.
organic dye							
Alexa Fluor 647	650	655	239,000	0.33	1.2×10^{-3}	5,202	[89]
Atto 488	510	523	90,000	0.8	2.2×10^{-3}	1,110	[89]
Atto 647N	644	669	150,000	0.65	3.5×10^{-3}	4,433	[89]
Cy3	550	570	150,000	0.15	0.3×10^{-3}	8,158	[89]
Cy5	649	670	250,000	0.28	0.7×10^{-3}	5,873	[89][88]
Cy7	747	776	200,000	0.28	0.4×10^{-3}	997	[89][88]
TAMRA	546	557	90,430	0.2	4.9×10^{-3}	2,025	[89]
FP^a							
Dendra2	490/553	507/573	45,000/35,000	0.5/0.55	4×10^{-6}	686/131 ^b	[90],[88]
mEos2	506/573	519/584	56,000/46,000	0.84/0.66	3×10^{-6}	745/360	[90],[88]
mMaple2	489/566	506/583	15,000/30,000	0.74/0.56	2×10^{-6}	783	[90]

λ_{ex} , excitation wavelength; λ_{em} , emission wavelength; ϵ , extinction coefficient; QY, quantum yield; duty cycle, fraction of on state dwelling time in one on-off switching cycle; No. photons, the average number of photons per switching event. ^a Values presented in λ_{ex} , λ_{em} , ϵ and QY entries are for two states of photoconvertible

FPs. ^b Number of photons per switching event is in terms of the state after photoconversion. Different experiment configurations, such as excitation power density, frame exposure time, and detection efficiency could be responsible for the discrepancy between the two reports.

In light of the low detection efficiency of our SPIM, I will focus on organic dyes used in direct STORM (dSTORM)[91] that do not require the activator fluorophore as in STORM[58], thus allowing for conventional immunofluorescence techniques for labeling a specific structure. There are mainly two immunofluorescence methods, *i.e.*, direct and indirect, the latter is more widely used. By indirect labeling, the epitope on the target molecule, also known as antigen, will be recognized and specifically bound by the variable site of the primary antibody, to the other side of which two or more secondary antibodies carrying fluorophores will bind. With such a binding strategy, each antigen is more likely to be spotted against photobleaching compared to the direct labeling manner, by which a

primary antibody complex carrying a dye molecule directly binds to the antigen. Additionally, the indirect labeling strategy facilitates the manufacturing and the usage of antibodies in a way that only the primary antibodies with varying variable sites and the secondary antibodies tagged to varying fluorophores need to be inventoried in lieu of adapting both the variable and fluorophore sites of a direct labeling antibody to different tasks.

The photoswitching mechanism of the organic fluorophores including carbocyanine dyes, rhodamine and oxazine derivatives can be understood as the interaction of the fluorophore in the triplet state with thiol groups and oxygen. Instead of intersystem crossing with oxygen and transition to the ground state via generation of reactive oxygen species, the fluorophore in the triplet state in aqueous imaging buffer containing thiol groups and oxygen scavengers will react with the thiol anion (RS^-) to form a thiyl radical and the radical anion of the fluorophore (F^\cdot) at a rate k_{exc}^1 [92], the value of which strongly depends on the irradiation power density, thiol concentration and the pH of the imaging buffer[93]. The non-fluorescent radical anion of the fluorophore can be oxidized back to the fluorescence singlet ground state in the presence of oxygen at a rate k_{ox}^1 . Irradiation of 350-550 nm light and increasing oxygen concentration will promote this process[94]. For oxazine and carbocyanine dyes, the semi-reduced radical anions are intermediary products that can subsequently react with thiolate at a rate k_{exc}^2 to yield the fully reduced leuco form (FH) for oxazine or thiol-adduct for carbocyanine[93] by forming a covalent bond with the thiolate at the polymethine bridge as shown in Fig. 2.17. Those fully reduced non-fluorescent species can likewise be oxidized back to the fluorescence singlet ground state mediated by oxygen and 350-550 nm light irradiation with rate k_{ox}^2 .

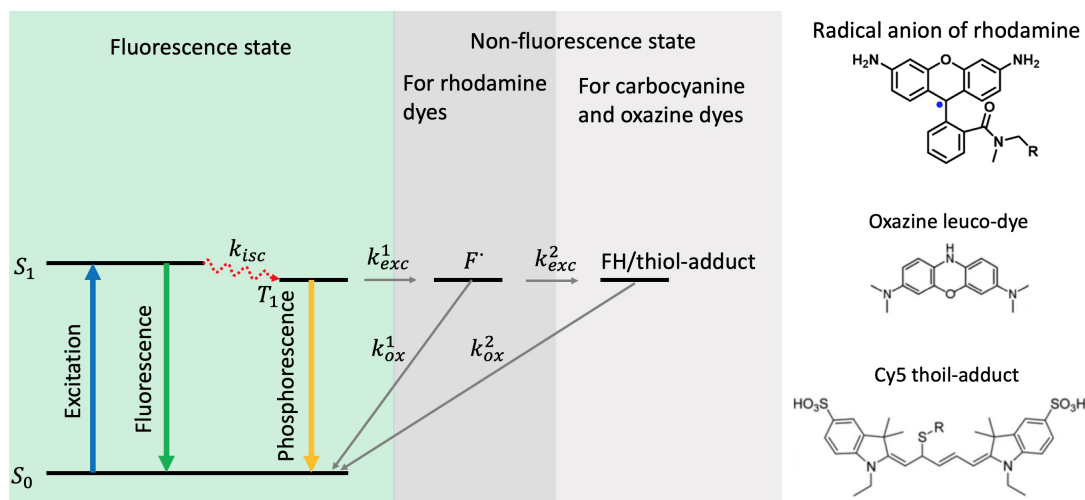


Figure 2.17: Photoswitching diagram. S_0 , electronic ground state; S_1 , electronic first excited state; T_1 , electronic triplet state. Adapted with permissions from [95, 96]. Copyright 2017, 2018 American Chemical Society.

Oxygen plays an important role in on-off switching cycles. The fate of fluorophores in the triplet state, which ends up with either intersystem crossing with oxygen and transiting to S_0 or forming non-fluorescence species mediated by thiol groups, depends on the reaction rates of individual processes. For the purpose of SMLM, the conversion of fluorophores in the dark state should predominate over the intersystem crossing process with oxygen. To this end, an oxygen scavenging system is employed to lower down oxygen level in the aqueous imaging buffer containing thiolate with a concentration as high as tens to hundreds of millimolar. However, on the other hand, the stable radical anion of the fluorophore, especially for rhodamine dye or leuco dye can persist for hours devoid of oxygen. Therefore, a low oxygen level in the imaging buffer is indispensable for the reactivation of fluorophore to the fluorescence state. In addition to the aforementioned reactions, such a high concentration of thiolate will further deplete oxygen to the same extent as the oxygen scavenging system[97]. Moreover, apart from the oxidation of non-fluorescent species, photobleaching, thiolate and oxygen scavenging process, thiyl radical, the by-product of the reduction reaction, will also consume oxygen to generate superoxide radicals and hydrogen peroxide[98].

The art of dSTORM allowing for moderately dense single molecules in the on state within any given exposure time is exemplified by manipulating on and off lifetimes through adjusting the concentrations of thiolate, oxygen scavenging buffer and irradiation intensity. A natural question arises if the photon budget per on-off switching event increases with excitation intensity as with the case in the absence of thiol groups and oxygen scavenging system (Eq. 2.7-2.8). It is reported that the number of photons per localization is inversely proportional to

the irradiation intensity[99] given the product of exposure time and irradiation intensity unchanged. This counterintuitive observation can be easily elucidated by a simple model assuming the number of fluorescence cycles (or the number of photons) it takes to trigger off-switching obeys a geometric distribution with the parameter equaling to the product of k_{exc}^1 and the rate of $S_0 - S_1 - T_1$ transition, which is proportional to the irradiation intensity. The expected number of photons emitted by a fluorophore before off-switching is hence inversely proportional to the irradiation intensity. As a result, a trade-off between acquisition speed and the number of photons per emitter has to be made because the sole way to increase the number of photons is to expand exposure time and fluorophore on time by using low excitation intensity, which is favorable to the application of SMLM in SPIM, as I will introduce in the next chapter.

Chapter 3

Methods and materials

3.1 The focal field

The simulation of the imaging system offers insight into how the microscope performance responds to varying parameters, thus allowing for systematic optimization regarding parameter selection for specific tasks. Excitation and detection PSFs, as crucial factors determining the resolution of the microscope, are the major objects to be investigated prior to the experiment.

As formulated in Eq. 2.12, the lateral PSF is equivalent to the Fourier transform of a plane wave clipped by the circular BFA of the objective lens in the absence of aberration. In reality, due to the misalignment and imperfect fabrication of the optical elements as well as the sample-induced aberration, the wavefront at the BFA is distorted. This continuous surface $\Phi(r, \varphi)$ can be represented by a family of orthogonal basis functions

$$\Phi(r, \varphi) = \sum_k c_k^{\text{Noll}} Z_k(\rho, \varphi), \quad (3.1)$$

where c_k^{Noll} is the expansion coefficient of Zernike polynomial $Z_k(\rho, \varphi)$ originally defined by two parameters[46]

$$\begin{aligned} Z_n^m(\rho, \varphi) &= R_n^m(\rho) \cos(m\varphi) \quad (\text{even over the azimuthal angle}) \\ Z_n^{-m}(\rho, \varphi) &= R_n^m(\rho) \sin(m\varphi) \quad (\text{odd over the azimuthal angle}), \end{aligned} \quad (3.2)$$

where the integers $n \geq m \geq 0$. The radial polynomials can be expressed as

$$R_n^m(\rho) = \sum_{k=0}^{\frac{n-m}{2}} \frac{(-1)^k (n-k)!}{k! \left(\frac{n+m}{2} - k\right)! \left(\frac{n-m}{2} - k\right)!}. \quad (3.3)$$

For convenience in representation, especially in aberration theory, the Zernike polynomials are re-indexed using one single parameter. In the Noll convention adopted in this thesis, for example, c_{11}^{Noll} corresponds to spherical aberration, $Z_0^4(\rho, \varphi)$ and c_5^{Noll} corresponds to oblique astigmatism $Z_2^{-2}(\rho, \varphi)$.

Instead of using Eq. 2.12, a more general form with an aberration term is used in the calculation,

$$E_{\parallel}(y, z) = \iint_{S_{\parallel}} \exp[i\Phi(y_0, z_0)] \exp[i(k_y y + k_z z)] dk_y dk_z. \quad (3.4)$$

According to the angular spectrum theory [29], the out-of-focus light field with Δx offset can be readily calculated by inserting the factor $\exp(i\Delta x \sqrt{k^2 - k_y^2 - k_z^2})$ into the integral in Eq. 3.4. For calculating the axial plane field $E_{\perp}(x, z)$, $\exp[i\Phi(y_0, z_0)]$ should first be mapped to wavevector space (see section 2.2.1) followed by a projection to the $k_x k_z$ plane (Fig. 2.5). Considering the spherical surface is not symmetric for arbitrary $\Phi(y_0, z_0)$, the summation of two pieces should be added in Eq. 2.14 as a factor.

The vector field integral adapted from Richards and Wolf model [100] is used to calculate the detection PSF for an objective lens with $NA = 1.1$, as used in my experiment. A basic concern is that linearly polarized photons are not coherent anymore after being focused because of dramatically changed polarizations, the orientations of which depend on where the photons interact with the dielectric medium of the lens. As shown in Fig. 3.1, the linearly polarized field \mathbf{E} before being refracted by the lens is decomposed into a radial part E_{ρ} and an azimuthal part E_{ϕ} [101], each of which propagates independently, governed by the Fresnel diffraction approximation that can be calculated via Fourier transformation. The polarization orientation of the azimuthal component always perpendicular to the radial axis does not change after refraction, while the radial component rotates by θ on the plane determined by the wavevector and the optical axis. The rotated polarization can be decomposed into an optical axis component \tilde{E}_x and a radial component \tilde{E}_{ρ} , which can be further decomposed into y and z directions. Similar decomposition rule also applies to E_{ϕ} , yielding the Cartesian representation of the light field decomposition at the focal point

$$\begin{aligned} E_y &= E_{\phi} \sin(\phi) + E_{\rho} \cos(\theta) \cos(\phi) \\ E_z &= E_{\phi} \cos(\phi) + E_{\rho} \cos(\theta) \sin(\phi) \\ E_x &= E_{\rho} \sin(\theta). \end{aligned} \quad (3.5)$$

In practice, a linearly polarized light field is pre-decomposed into those three components, followed by calculating the focused fields, the intensity summation of which gives the effective PSF within the vector diffraction framework.

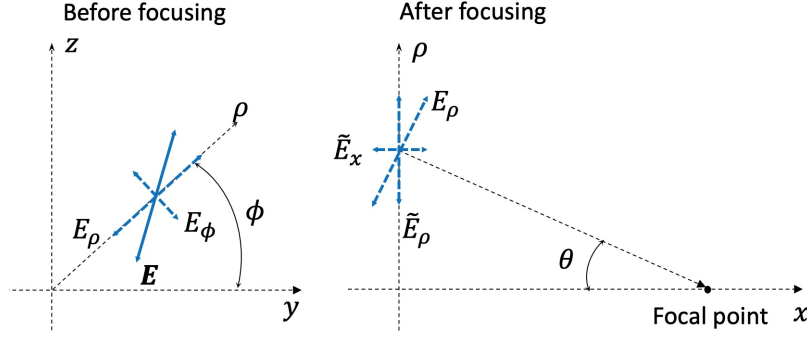


Figure 3.1: Illustration of polarization decomposition in cylindrical coordinates.

3.2 Optimization of the lattice light sheet

As with the Bessel beam, a practical lattice beam is characterized by its constituent plane waves. A fundamental measure of the lattice is the parameter k_{\parallel} , which dictates the lattice period and the main lobe thickness. A rule of thumb is selecting the proper k_{\parallel} so as to align the two side lobes flanking the main lobe of the scanned lattice to the first two zero valleys of $h_{\text{det}\perp}$, thus filtering out the strongest background excitation near the focal plane on the detection objective lens, as shown in Fig. 3.2a.

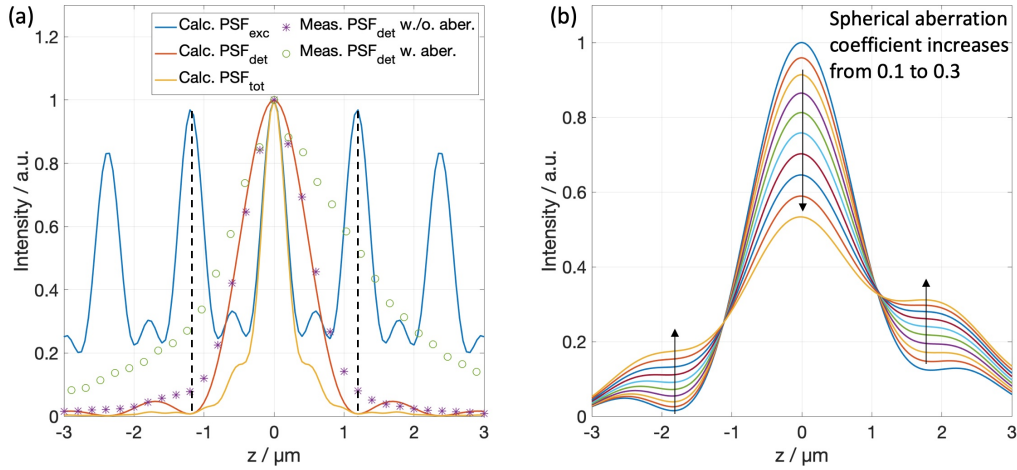


Figure 3.2: Determination of the lattice period for an optimal PSF. (a) Comparison between calculated and measured PSFs. Ideally, to effectively cancel the background elicited by sidelobe excitation, the lattice with optimal period has its sidelobes aligned to the first valleys of h_{det} , which experimentally do not exist due to imperfect optics. (b) Simulation of a distorted h_{det} with peak to valley depth of the 11th Zernike polynomial in Noll convention for a spherical aberration varying from 0.1λ to 0.3λ [46].

Due to the existence of refractive index (RI) mismatch-induced aberrations, especially spherical aberration, which mostly elongate $h_{\text{det}\perp}$, the two valleys marked by the dashed lines in Fig. 3.2a that should have been present in the measured h_{det} are missing. This fact leads to a more flexible lattice design strategy, with which not only background rejection but also axial resolution, covered FOV and the light sheet thickness shall be comprehensively taken into account[102]. For instance, a large k_{\parallel} allows for higher axial resolution at the cost of squeezing the lattice in the axial direction, hence the thicker light sheet and narrower FOV (Fig. 3.3), given that the size of the experimental plane waves used to generate the lattice beam is fixed. To achieve a comparable covered FOV range as with low k_{\parallel} , the plane waves have to widen, which in turn leads to an even thicker light sheet. As a result, excessively pushing the axial resolution limit while keeping a large FOV will converge in epi-illumination. In the following part of this section, I will show the simulation of a lattice linked to our setup configurations and discuss the optimal parameter choices for this topic.

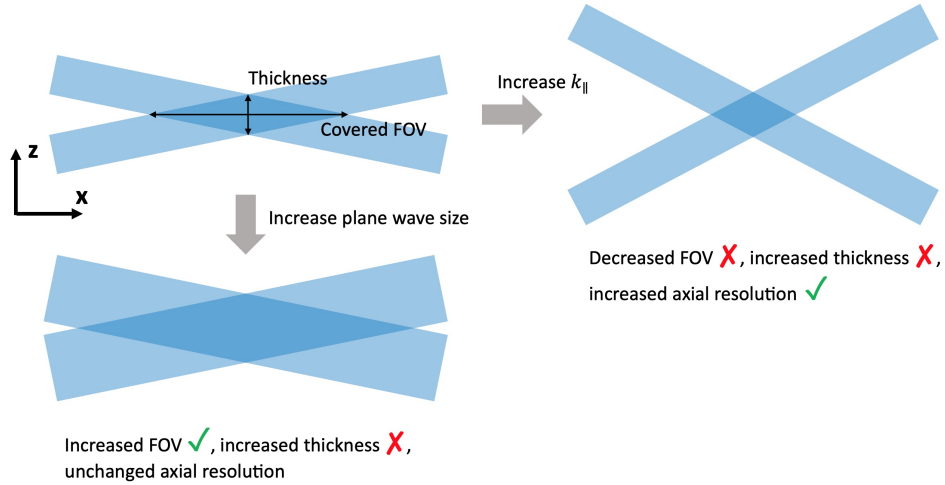


Figure 3.3: Illustration of the dependency of the lattice shape on k_{\parallel} and the constituent plane waves.

As with Eq. 2.26, the structure of the lattice light sheet in the focal plane can be related to the wavevector distribution on the BFA via Fourier transformation, where NA_{eff} is determined by the smallest circle encompassing the spectrum. Physically, the wavevector space is the momentum space of the electromagnetic wave, while the focal plane corresponds to the position space. Evidently, the Heisenberg uncertainty principle $\Delta x_i \Delta p_i \geq \hbar/2$ holds, asserting that the larger the uncertainty of the momentum, the smaller is the uncertainty of the photon distribution in position space, *i.e.* a smaller focused spot [103]. Reversely, if one wants to compress the lattice in z direction in the focal plane, the elongation of the spectrum along k_z will yield the desired result.

With increasing aspect ratio of the Gaussian spots, the diffraction-free lattice gradually wanes, in the form of a lower number of side lobes and a narrower light sheet thickness, to a diffraction-limited beam on the xz plane as shown in Fig. 3.4. I define a measure of the SBR as the accumulated intensity of the scanned lattice within the FWHM range of h_{det} divided by the remainder of the intensity integral. The higher this ratio, the thinner is the lattice. Because of the destruction of the diffraction-free property, the covered FOV is measured by the FWHM of the lattice main lobe. It is worth noting that parameters used in the calculation are adapted to realistic experimental conditions.

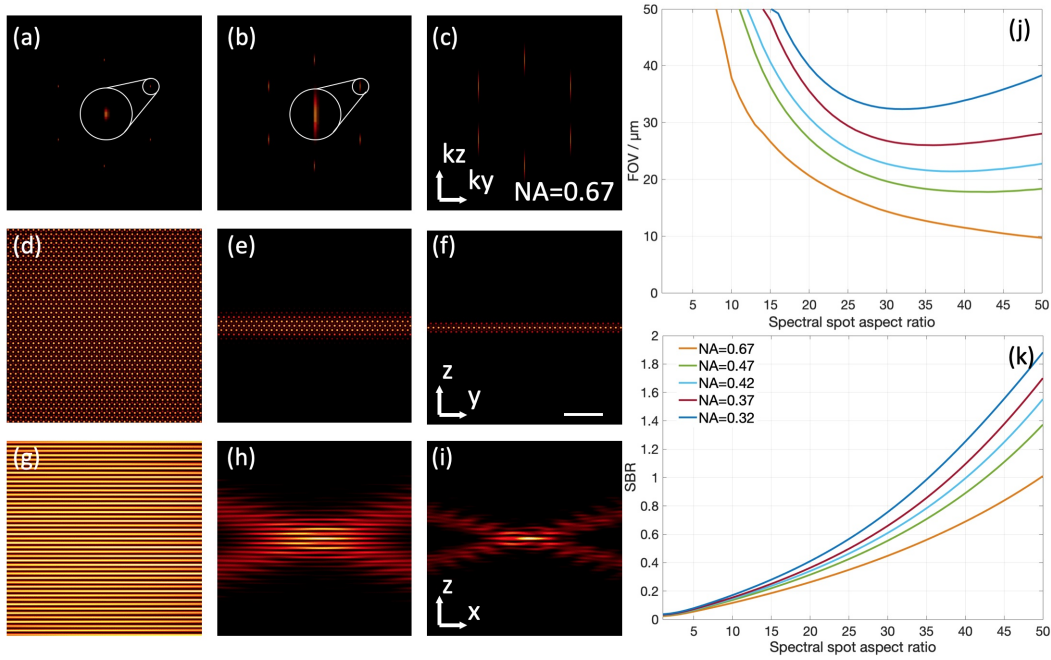


Figure 3.4: Simulation of an experimentally generated lattice and its relationship to NA and spectral spot aspect ratio. (a)-(c) Lattice spectrum spots with increasing spectral spot aspect ratio in momentum space. (d)-(f) The lateral cross-section of the lattice pattern is gradually compressed as the spectral spot aspect ratio increases. Scale bar $10 \mu\text{m}$. (g)-(i) The axial plane cross-section of the lattice pattern shrinks as the spectral spot aspect ratio increases. (j) Covered FOV of the lattice as a function of the spectral spot aspect ratio. (k) Lattice SBR to spectral spot aspect ratio.

Even though a $1.1 NA$ water immersion detection objective lens and a $0.67 NA$ water immersion excitation objective lens are employed in the experimental setup the NA_{eff} for the excitation objective lens is smaller, so as to achieve a sufficiently large FOV. Fig. 3.4j-k show SBR and FOV in terms of spectral spot aspect ratio for a range of NA_{eff} of the excitation objective lens. Despite the highest axial resolution rendered by a large NA_{eff} , both SBR and FOV are inferior to low NA_{eff}

cases regardless of the spectral spot aspect ratio. Given a certain NA_{eff} , there is a trade-off between high SBR and large FOV. For time-lapse live cell imaging, a general requirement is low phototoxicity, low photobleaching and a large FOV to cover the whole region of interest (ROI). In comparison to these factors, resolution is of least importance.

I use $SBR = 0.32$ as a benchmark obtained from the calculated h_{det} and h_{exc} in Fig.3.2a, a value that is suggested to be optimal in the literature [5]. If one wants to achieve $SBR > 0.32$, the spectral spot aspect ratio of 16 is the minimal possible choice among NAs varying from 0.32 to 0.67, as shown in Fig. 2.5k. However, a smaller spectral spot aspect ratio is preferable if a large FOV is desired for any given NA . I empirically require the FOV to be larger than 50 μm , being the minimum requirement to cover a whole ROI in either observation of Wnt vesicle transport or nanoparticle uptake experiments, which are the later subjects of my work. Apparently, only a $NA = 0.32$ satisfies the outlined constraints.

3.3 Experimental implementation

3.3.1 Wave front engineering

There are two ways of creating a lattice. A straightforward way is selecting points out of an annular spectrum of a Bessel beam, which is of low efficiency. The other way is to modulate the complex amplitude of an expanded Gaussian beam, which can be approximated as a plane wave, with the aid of a spatial light modulator (SLM), a powerful optoelectronic device with a wide spectrum of applications varying from photonics to engineering and medicine, where customizing the electromagnetic field from ultraviolet to near-infrared is involved. By incorporating the SLM into the excitation path, the lattice can be adapted to suit diverse imaging tasks with distinct parameter settings. Certainly, the excitation light does not necessarily have to be in the form of a lattice, it could also be a Bessel beam or a Gaussian beam, which are indispensable for fine alignment.

In my work, I utilize a reflective phase-only SLM that modulates the phase of the light field by spatially introducing a phase retardation map through altering the effective refractive indices of a birefringent liquid crystal, the fast axis of which is oriented along the wavevector of the incident plane wave. Upon applying an external voltage, the fast axis rotates in response in the plane of the incident light polarization direction and wavevector. As a result, the effective RI of the liquid crystal is governed by

$$n_{\text{eff}} = \frac{n_o n_e}{\sqrt{n_o^2 \sin^2 \varphi + n_e^2 \cos^2 \varphi}}, \quad (3.6)$$

where n_o and n_e are the refractive indices for ordinary and extraordinary ray, φ is the rotated angle. In addition to the nonlinearity between n_{eff} and φ , the voltage

dependency of the angle φ is also irregular[104]. A so-called gamma correction should be carried out for different wavelengths, for which a look-up table (LUT) is created, mapping the voltage delivered from the SLM driver to the liquid crystal on silicon (LCOS) to the modulation depth ranging from 0 to 2π . From the user's side, an 8-bit image that describes the target phase map evenly distributed among 2π phase is used as an input to the SLM driver. The panel of the SLM is pixelized, allowing for independent addressing of each individual pixel by the driver. A grayscale image with the size of the LCOS device can be displayed on the SLM. The driver reads it from the graphics card and converts the grey values to the voltages to be applied to the substrate electrodes of LCOS cells.

3.3.2 Phase mask designing

As spectra for all excitation modalities are either thin annular slits or point arrays, a great amount of energy will be lost, provided the SLM display is conjugated to the BFA of the excitation objective lens. Therefore, a different method can be employed by positioning the SLM in the conjugated plane of the focal plane. For the Bessel beam, an axicon lens is emulated by displaying a phase mask of $\exp(i2\pi k_{\parallel} r)$ on the SLM. The center of the Bessel beam appears at $\frac{rk_{\perp}}{2k_{\parallel}M}$ in front of the SLM, where r is the physical radius of the phase mask on the SLM and M is the magnification. A small k_{\parallel} is selected to allow for legible and large fringe patterns in a dye sample to facilitate fine alignment. The phase mask for the Gaussian beam is simply a blank rectangular area with high aspect ratio; thus, a thin one-dimensional Gaussian waist will be projected to the focal plane. Although the fill factor of the SLM display is as high as 93%, LCOS cells are arranged in a grid with gaps, causing infinitely high diffraction orders centering around the unmodulated zero-order spot. To isolate the first diffraction order, a blazed grating is superposed to all phase masks (Fig. 3.5a-b).

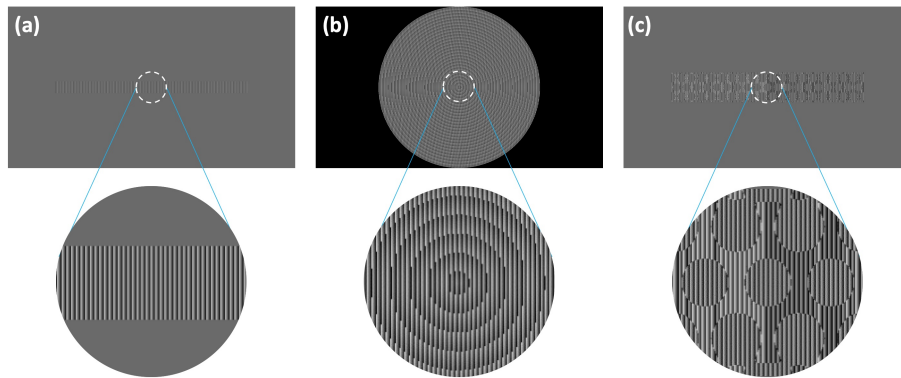


Figure 3.5: Holograms to be applied to the SLM display. Holograms for a Gaussian beam (a), a Bessel beam (b) and a lattice beam (c).

For lattice generation, complex amplitude modulation comes into play, as a phase-only SLM is solely capable of modulating the phase of a light field while Eq. 2.27 requires continuous intensity modulation. A complete pipeline to lattice phase mask designing is shown in Fig. 3.6.

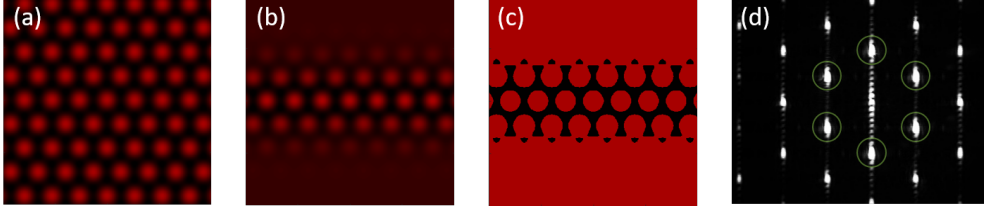


Figure 3.6: Lattice pattern generation pipeline. (a) Complex amplitude for ideal lattice pattern. (b) Bounded complex amplitude for ideal lattice pattern. (c) Binary bounded lattice pattern. (d) Experimentally measured spectrum of binary bounded lattice pattern. The six spots highlighted in circles are selected by a mask.

The calculation results in section 3.2 on optimal parameter settings of a hexagonal lattice are considered and implicitly included in the Gaussian bound 2D lattice expression $E_{\text{hex}}(y, z)\Psi(z)$, which is then subjected to the Heaviside function with threshold $\epsilon = 0.5$. At last, a $0/\pi$ phase binary mask

$$\phi_{\text{SLM}}(y, z) = \pi \cdot H[E_{\text{hex}}(y, z)\Psi(z) - \epsilon] \quad (3.7)$$

is applied to the SLM. The modulated light field turns out to be a $-1/1$ periodic intensity pattern, of which the base frequency Fourier decomposition is nothing more than the desired lattice. Direct Fourier transformation of this binary intensity pattern shows six bright dots, representing the wavevectors of constituent plane waves of the lattice (Eq. 2.27), surrounded by infinitely high order frequency components (Fig. 3.6d). By inserting a mask at the conjugated plane of the BFA that only retains the hexagonal point spectrum, the designed lattice can be realized.

3.3.3 Experimental setup

The experimental setup for SPIM consists of two arms, the detection path and the excitation path (Fig. 3.7). On the junction of the two paths are two orthogonally arranged objectives lenses (Special Optics, Model 54-10-7, NA 0.67, 3 Stewart Ct, Denville, NJ 07834, United States and NIKON, 25X-APO-MP, NA 1.1, Minato City, Tokyo, Japan) with the sample located near the intersection region of their focal planes.

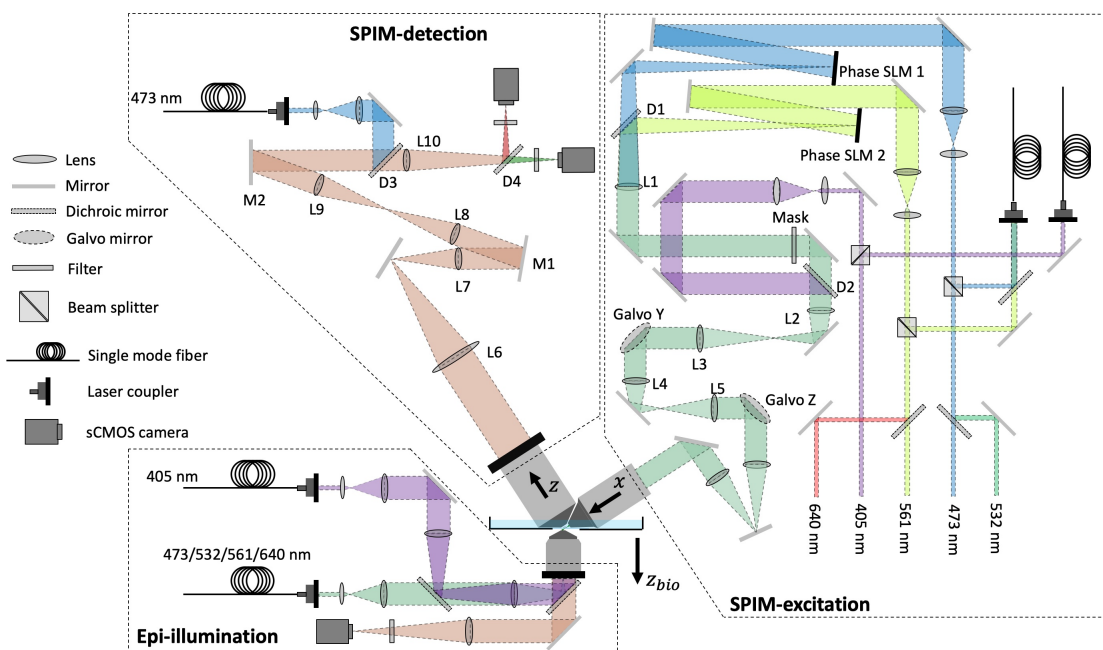


Figure 3.7: Schematic of the experimental setup.

Four lasers with wavelengths 473 nm, 532 nm, 561 nm, and 640 nm, (all of them are diode-pumped solid-state lasers manufactured by Laser Quantum, 3083 Lawrence Expy, Santa Clara, CA 95051, United States) are divided into two groups (473 nm combined with 532 nm and 561 nm combined with 640 nm laser, respectively), independently manipulated by two SLMs (Holoeye, LETO, Volmerstrasse 1, 12489 Berlin). The LUTs loaded on the SLMs were individually gamma corrected with respect to 532 nm and 640 nm lasers, meaning modulation depths of 255 grey value for shorter wavelength lasers sharing the same LUTs will be beyond 2π . The upper limit of grey values, at which the modulation depth equals 2π for the 473 nm and the 561 nm laser, were experimentally measured as 214 and 204, respectively.

All laser beams are expanded 12.5 times to fully cover the SLM displays. Such a layout allows for simultaneous two-channel excitation. The modified beams are separately demagnified by a factor of three using two pairs of 150-50 telescope lenses before being combined through a long-pass dichroic mirror at 550 nm (D1). Placing the back focal plane of the $f = 150$ mm lens on the SLM relays the wavefront on the SLM display to the front focal plane of the $f = 50$ mm lens. All telescopes involved in the following text are arranged in pairwise confocal geometry, if not otherwise specified. A $f = 400$ mm lens (L1) after the 150-50 telescope applies Fourier transformation to the modulated beams and projects their spectra on a mask to select the base plane wavevectors used to create the lattice. In-between the mask and another telescope with 1.2 fold magnification

(L2 and L3) that conjugates the beam on the mask to a y -galvo mirror (Cambridge technology, 8330K, Bedford, Massachusetts, United States) is a 450 nm long-pass dichroic mirror (D2) used to incorporate collimated 405 nm laser beam (LaserBoxx HPE series manufactured by OXXIUS Simply Light, 4 Rue Louis de Broglie 22300 Lannion, France). Following the y -galvo, another telescope consisting of a $f = 80$ mm f-theta lens (L4, S4LFT4375 telecentric F-Theta, Sill Optics GmbH, Johann-Hoellfritsch-Strasse 13, 90530 Wendelstein, Germany) and $f = 100$ mm ordinary lens (L5) is positioned to relay the beam on the y -galvo mirror plane to the z -galvo mirror plane whose scanning axis is orthogonal to the y -galvo axis. At last, two telescopes conjugate the beam on the z -galvo mirror to the BFA of the excitation objective lens. One telescope consists of a $f = 80$ mm f-theta lens and a $f = 80$ mm ordinary lens, while the other is comprised of two $f = 200$ mm lenses. All lenses in the system are apochromatic plano-convex lenses, if not otherwise specified.

Five lenses confocal with one another are deployed in the detection path to give an overall magnification factor of 67. The first lens right after the detection objective lens is a $f = 200$ mm tube lens (L6) customized for the objective lens. It has one focal plane located at the BFA of the detection objective lens and the other confocal with a $f = 150$ mm lens (L7), thus the demagnified BFA plane is conjugated to the back focal plane of L7, where a plane mirror (M1) is deployed to deflect the fluorescence signal into a telescope ($f = 200$ mm and $f = 100$ mm L8-L9) confocal to L7. On the back focal plane of L9 is a planar mirror (M2) used to reflect the fluorescence signal into a $f = 200$ mm lens (L10), one focal plane of which shares the same focal plane as L9. A 480 nm long-pass dichroic mirror (D3) is located between L10 and M2. Collimated reference light, normally 473 nm, is introduced from D3 and passed through all optics in the detection path all the way to the detection objective lens to create a guide star in dye solution (see section 3.7.3) for fine positioning of the excitation light sheet. And finally, a dichroic mirror (D4) separates the fluorescence light onto two sCMOS cameras (Hamamatsu Orca 4.0, Shizuoka, Japan). The selection of D4 and filters depends on the emission spectra of the probes in different measurement tasks. Redundant lens pairs in the detection path are intended for future implementation of adaptive optics, in which M1 will be replaced with a deformable mirror and M2 will be replaced with a galvanometer mirror [105].

In addition to the light sheet path, an epi-illumination path with a low magnification air objective lens (20X, CFI S Fluor, NIKON, Minato City, Tokyo, Japan) is also implemented as a supplement, allowing us to browse through the coverslip and spot cells of interest. Two pairs of laser lines (473 nm & 532 nm and 561 nm & 640 nm) are split right in front of the beam expanders. Apart from those going into the SPIM excitation path, the other half of the laser light is further combined and coupled into a single-mode fiber, the output port of which is either connected to a SPIM detection path for guide star creation or to the epi path to generate a uniform illumination. A tube lens with 200 mm focal length collects

photons passing through the dichroic mirror and forms an image on an sCMOS camera sensor at the BFA of the tube lens. An optional functionality enabling laser-induced damage experiments on cell membranes is implemented through introducing, by using another set of fiber-laser coupler, collimated 405 nm laser at the BFA of the epi-objective, which in turn creates a tightly focused 405 nm laser spot on the sample.

3.3.4 Control strategy

All electronic devices used in SPIM microscopy are controlled by customized software developed by Dr. Kobitski and modified by Dr. Flatten using the C language. The control commands are sent via appropriate communication protocols to lasers, SLMs and T1000 control box (Applied Scientific Instrumentation, 29391 W Enid Rd, Eugene, OR 97402, United States), which integrates the driver cards for all motor driving stages (SPIM objective vertical stage, epi objective stage, XY translation stage) and piezo stages (detection objective lens stage and Z stage). The SLM drivers are connected to the graphics card with HDMI connectors so that the operating system recognizes the SLMs as displays. One only needs to load the designed 8-bit images onto the corresponding displays to load the holograms on the SLM. Two sCMOS cameras working in external trigger mode for the SPIM path are connected to a camera link directly plugged into PCIe slots on the workstation. The positioning of the detection objective, the two galvo mirrors and the camera triggers are synchronized by a signal generated from two data acquisition (DAQ) devices (National InstrumentsTM, Austin, Texas, United States). In more detail, the analog signal sequences, the length and amplitude of which are determined by the number of steps and step size specified in the acquisition protocol, are generated by DAQ 1 to control the piezo stage and the z -galvo. The frame trigger and control signal for the y -galvo are generated by DAQ 2 with higher temporal resolution. Upon the acquisition task getting started, a start trigger issued from the digital output port on DAQ 2 triggers the frame trigger signal to stream into both cameras and to the external clock port of DAQ 1 that in response sets a modulating voltage according to one data point of a pre-buffered sequence to the z -galvo and the piezo stage. At the same time, a control signal for the y -galvo is set by another analog output port of DAQ 2. As soon as one complete sequence of frame triggers is streamed, which takes a time as long as the exposure time configured in the acquisition protocol, DAQ 2 immediately starts a new cycle until the designated number of frames is obtained by counting the acquired frames from the frame counters of the cameras.

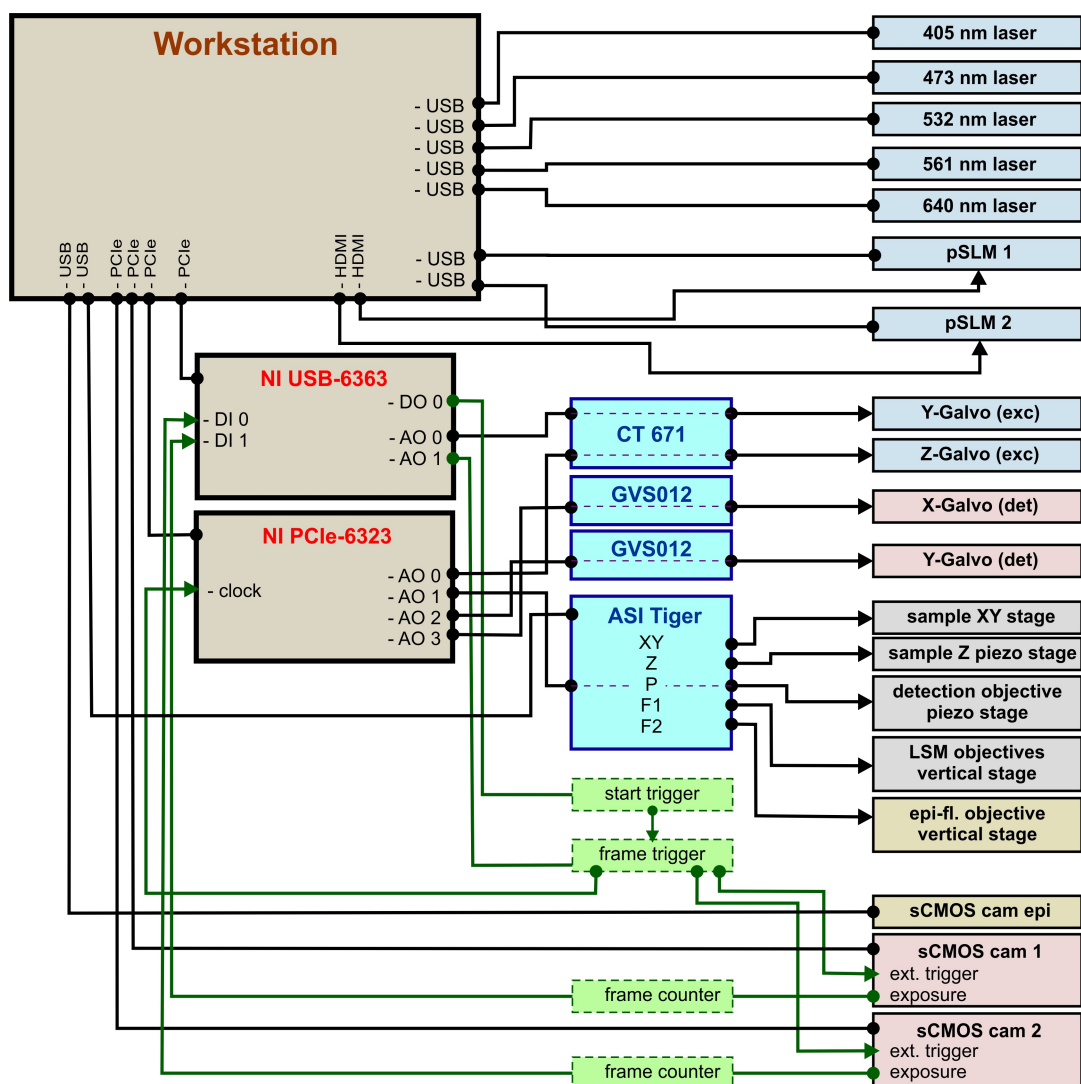


Figure 3.8: Schematic for electronic connection. Figure is adapted from Dr. Kobitski's report for SFB 1324 project.

3.3.5 Setup alignment

Static alignment

The limited size of the lens apertures, especially L7 (25.4 mm) and L8 (30 mm), considerably restrain the available aberration-free FOV of the detection objective lens, beyond which spatially varying aberration induced by the optics will dominate. Therefore, the center of the detection FOV, from which fluorescent light propagates paraxially, has to be carefully adjusted. To this end, I developed the following procedure: I introduce a reference light from D3 in the detection path and reflect it back to D3 through M2. By carefully positioning M2, D3 and L10,

the incident and reflected beam between M3 and D3 are co-axial and, at the same time, the transmission beam from D3 is aligned to L10 and the center of camera. Then M2 reflects incident light to L9 and the reference light is aligned to all optics thereafter up to the detection objective lens. The fluorescence from the guide star in a dye solution created by the focused reference light goes through the detection path all the way back to the camera. In this way, the guide star marks the FOV center of the detection objective lens. The cameras are laterally aligned such that the guide star coincides with the center of cameras.

The first step of alignment for the excitation path is to successively align the center of the Gaussian beams of 473 nm and 561 nm to the centers of the cameras. The other two laser lines should automatically be aligned as they share the same paths after the SLMs. Tip-tilt alignment in z direction is done with the aid of a propagation-invariant interference pattern of low NA Bessel beams. The rule of thumb is to deflect and shift the Bessel beam until the high contrast interference pattern is resolved throughout the propagation length (Fig. 3.9b).

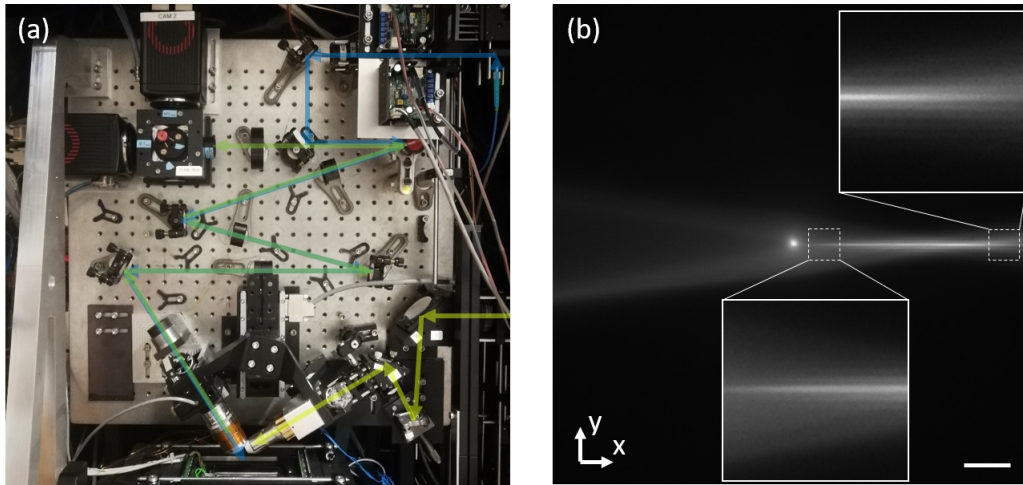


Figure 3.9: Schematic of the static alignment procedures. (a) The detection path. Blue arrows represent the reference light, green arrows show the path of the fluorescence light and yellow arrows mark the excitation light. (b) Guide star and Bessel beam in dye. The guide star should coincide with the center of the camera. The excitation beam is aligned such that a crisp interference pattern is observed at both ends of the Bessel beam. Scale bar, 20 μm .

The next step is to check if the light sheets are spatially overlapping at the sample plane. This is done by successively recording the image of the same fixed multicolor bead when Gaussian light sheets are scanning across it while the piezo stage remains fixed. The intensity change of the fixed bead characterizes the profile of the light sheet in z direction. For fine alignment, the holograms on the SLM for the 561 nm laser will be shifted by the distance that the peaks of the

light sheet profiles are separated. In doing so, the 561 nm light sheet will overlap with the 473 nm light sheet. At last, the camera for the 561 nm channel should be shifted along the optical axis to compensate for chromatic aberration.

Note that the manual alignment with a dye solution can only achieve up to 500 nm precision in z direction. Therefore, further fine alignment should be done with the bead immobilized on a coverslip surface. The detection PSF can be examined by scanning the piezo stage while keeping the light sheet fixed. Should an axially asymmetric PSF be observed, the collar ring on the detection objective lens is to be adjusted. This step is intended for eliminating spherical aberration. The last step is to examine the overall PSF by synchronously scanning the light sheet as well as the piezo stage across a fixed bead. Symmetric out-of-focus intensity attenuation with respect to the center of the PSF should be observed, otherwise, a voltage offset has to be applied to the z galvanometer scanner. With the outlined procedure, the light sheet can be aligned relative to the detection focal plane with up to 120 nm precision.

Dynamic alignment

Ahead of each acquisition of one volumetric dataset in the time-lapse measurement loop, the system will take around 3 s to reconfigure all devices, which is too slow for tasks like SMLM modality and nanoparticle tracking experiments where hundreds of thousands of volumes are required. To skip this reconfiguration process between volumes, a fast scanning mechanism was developed, by which each acquisition task creates a hyperstack containing multiple volumes while samples are undergoing persistent exposure with the focal plane and light sheet synchronously and continuously scanning across samples. The dynamic response of the galvanometer scanner and piezo stage to alternating signals should thus be investigated. It is safe to assume the galvanometer scanners featuring a broad bandwidth can accurately follow a control signal operating at up to 10 Hz with a small scanning angle. Whereas an apparent discrepancy between the input signal and position sensor reading for the piezo stage indicates the piezo stage cannot catch up with the sudden change present in a saw tooth signal irrespective of the scanning frequency. To circumvent this problem, a triangle signal is adopted for the fast acquisition mode.

To approximate the lag between the modulating signal and the actual position of the objective lens, a forced oscillation model is employed,

$$\frac{d^2x}{dt^2} + 2\zeta\omega_0\frac{dx}{dt} + \omega_0^2x = \frac{1}{m}F_0\sin(\omega t), \quad (3.8)$$

where ζ denotes the damping coefficient and ω_0 is the natural angular frequency of the oscillator. The analytical solution is written as

$$x(t) = \frac{F_0}{mZ_m\omega} \sin(\omega t + \phi_0), \quad (3.9)$$

where

$$Z_m = \sqrt{(2\omega_0\zeta)^2 + \frac{1}{\omega^2}(\omega_0^2 - \omega^2)^2}, \quad (3.10)$$

and

$$\phi_0 = \arctan\left(\frac{2\omega\omega_0\zeta}{\omega^2 - \omega_0^2}\right). \quad (3.11)$$

It should be noted that the piezo stage is technically not an oscillator under sinusoidal force but rather a position-based feedback system. A high-frequency alternating control signal is superposed to the specified base command such that the piezo stage can precisely set to the given position without damping, overshooting, oscillation and *etc.*, which is confirmed from the graph of input and position sensor signal on the oscilloscope (Fig. 3.10a). Moreover, the solution to Eq. 3.8 is in terms of a forced oscillator under a sinusoidal driving force while our external force is in triangle form. Therefore, the resultant fitting to the phase lag ϕ_0 , which gives rise to wrong frame registration in image stacks can partly characterize the piezo stage as a forced oscillator. To clarify the phenomenon, I denote the forward and backward scanning image stacks as m0 and m1, respectively. For a 6-frame image stack recorded in the fast mode without lag, for instance, if one emitter appears in the 2nd frame of the m0 stack, it should reoccur in the 5th frame of the m1 stack. In the presence of a lag of 2 frames, an emitter that appears in the 5th frame of the m0 stack will reoccur in the 6th frame of m1 stack (Fig. 3.10b-c).

A straightforward quantification can be obtained by inspecting fixed beads in agarose gel acquired under the fast mode, yielding rough lag information to the precision of half a frame. Preliminary estimation of the lag as a function of frequency is shown in Fig. 3.10f. We circularly shift the discrete sequence of controlling signals to approach the lag to the extent of half the frame residual. To validate this method, I run the localization routine on a beads image recorded with the most frequently used acquisition protocols, the lag factors of which are individually assigned according to the initial estimation. The step size is fixed to 400 nm, guaranteeing up to 200 nm residual misalignment comparable to at most 250 nm static alignment error. In the worst case, where 200 nm dynamic error and 250 nm static concur, the overall misalignment in one scanning direction will almost cancel, while in the other direction, it amounts to 450 nm. Fortunately, such great misalignment is discernible in the sensor output signal when

the measurement is running and hence can be avoided. The acquisition parameters that jointly define the scanning frequency are exposure time and the number of slices per stack. Totally 6 acquisition protocols are investigated with the free combinations of 5, 10, 20 ms exposure time and 25, 50 frames per stack.

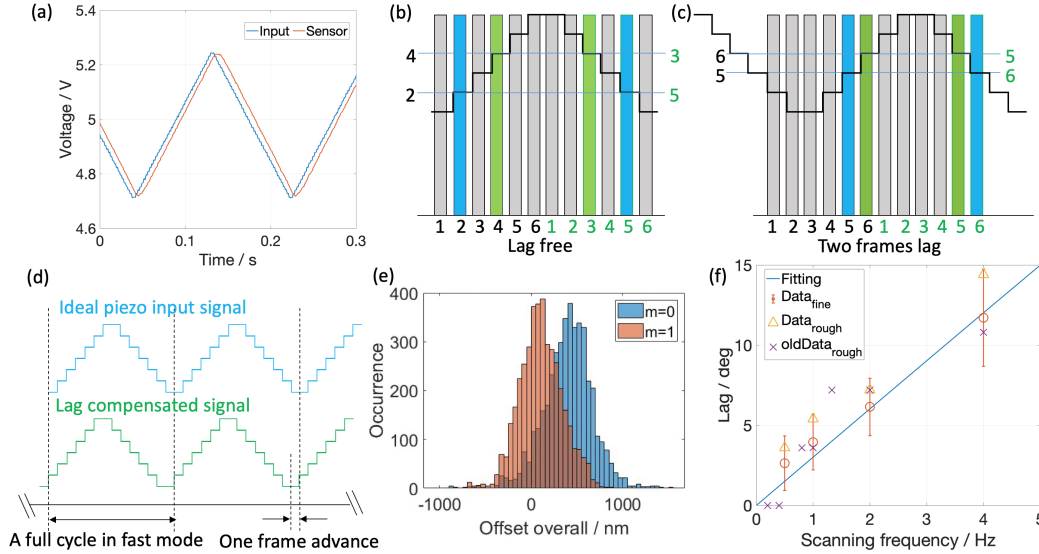


Figure 3.10: Determination of the dynamic alignment procedures. (a) Comparison between input signal and position sensor signal reveals temporal lag. (b) Image registration into m_0 and m_1 sequences without lag. The stair signal denotes the piezo stage position and the serial rising edge triggers camera frames registered into m_0 and m_1 sequences. (c) Image registration into m_0 and m_1 sequences with two frames lag. (d) One frame of the piezo input signal is circularly left-shifted to compensate for lag. (e) The statistics of the measured overall misalignment in m_0 and m_1 scanning directions with a certain scan protocol. The global misalignment is extracted from the median of the statistics. (f) The lag with respect to scanning frequency is fitted to a forced oscillation model, where ω_0 is 76π rad and ζ is 1. Triangle markers are rough estimations to the lag manually evaluated through inspecting raw data of fixed beads, so are the cross markers calibrated earlier. Circle markers with error bars are the accurate evaluations using a single emitter fitting algorithm.

The fitting result characterizes the overall offset $OStot_{exc}$ between PSF_{exc} and PSF_{det} , which is the summation of static and dynamic misalignment. The dynamic misalignment originates from the piezo stage lag and is identified as $(OStot_{m_0} - OStot_{m_1})/2$. The fitting algorithm will be elaborated in detail in section 3.5. The realistic lag is actually the summation of pre-estimated lag being the integer times of the one frame lag and the finer lag obtained from the fitting result (Fig. 3.10f). The forced oscillation model Eq. 3.8 is shown to be a good approximation, from

which the lag factor can be calculated for any given acquisition protocol. By virtue of the robustness of the fitting algorithm, the residual overall misalignment will not lead to a deteriorated localization precision.

3.3.6 Environmental chamber

Long-term time-lapse measurements with live cells require an environmental chamber to maintain the cells in physiological conditions (37 °C, 5% CO₂) as well as the proper cell culture medium. Because two objective lenses are directly immersed from above into the cell culture medium, a customized chamber lid encompassing both objective lenses is needed to maintain the correct temperature. Five heating units are used to heat the chamber bottom, the chamber frame, the lid and the two objective lenses in a closed-loop way, allowing for fast acclimatization after sample swapping. The heating units on the objective lenses and lid prevent condensation, protect the objective lenses and minimize water loss-induced concentration changes in the cell medium. This is critical for both the cells and the microscope performance, as a RI change alters not only focal positions but also introduces spherical aberration.

Owing to the cylindrical shape of the objective lenses, simply wrapping them with polyimide ThermofoilTM heaters (HK6903 and HK6908, MINCO, Minneapolis, Minnesota, United States) renders a uniform temperature distribution. In contrast, the irregular shape of the lid imposes difficulties in terms of how to arrange the resistor array to heat it uniformly. To this end, I calculated using finite element analysis software (COMSOL) the temperature map on the lid given a resistor array layout as shown in Fig. 3.11(bottom). Several assumptions are made to simplify the calculation including that the lower surface of the lid is subjected to a constant 37 °C environment, while the upper surface undergoes free convection exposed to a 20 °C room. The modeled two objective lenses, whose temperature is assumed to be 37 °C, are in contact with the lid over a 0.5 mm air gap. On the nodes of four heating circuits, a 0.7 A current is applied to give a stationary thermal distribution, as shown in Fig. 3.11. The aluminum objective lens mount acts as a heat sink, leading to a 0.34 °C/cm thermal gradient due to the direct contact. Therefore, another ThermofoilTM heater (HK6908, MINCO) is installed on the inner wall of the mount, constantly providing 3 W heating power. With all components implemented, including two fully filled reservoirs inside the environmental chamber, 3 h evaporation rate of the imaging medium reduces from 2.6 mL to 0.5 mL, which is inevitable as 0.05 L/minute 5% CO₂ introduced from the bottom plate results in air exchange between 37 °C water-saturated air inside the chamber and 20 °C dry air outside it through thin gaps between the lid and other parts. A syringe pump (AL-1000, World Precision Instruments Inc., 175 Sarasota Center Blvd. Sarasota, FL 34240, United States) with a high-resolution fluid delivery rate is employed to compensate for the water loss at the end.

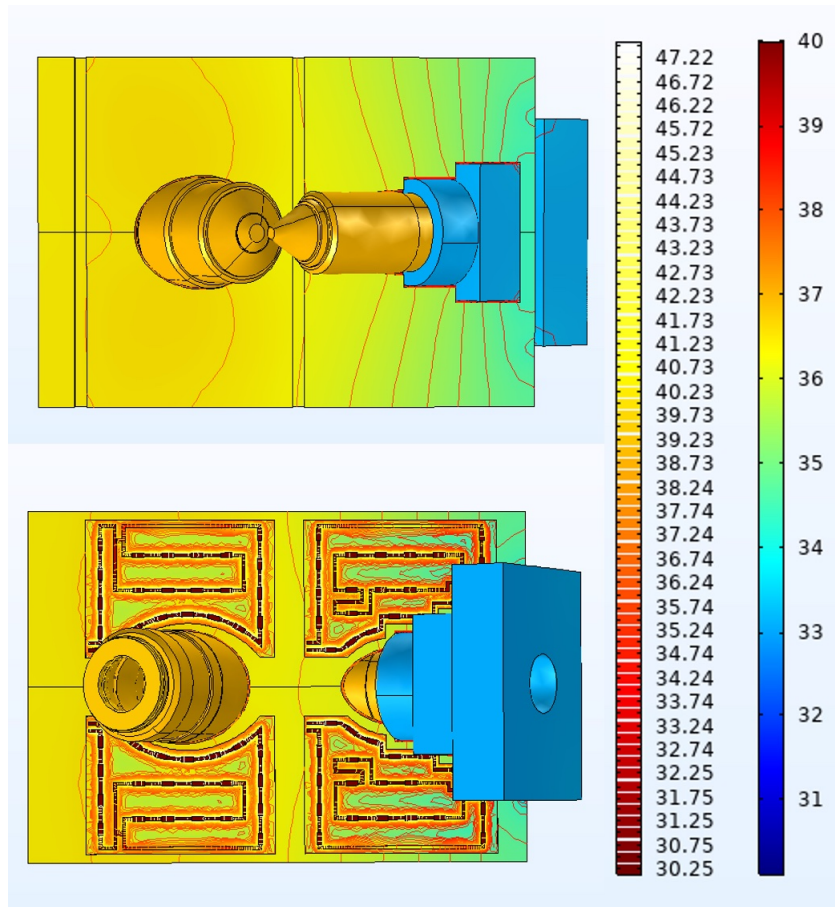


Figure 3.11: Stationary temperature map of the environmental chamber lid. The top image shows the temperature distribution on the bottom surface of the lid. The bottom image shows the resistor array arrangement on the top surface of the lid. The red hot color bar quantitatively indicates the temperature contour with 0.5 °C step size while the jet colormap visualizes the temperature distribution.

Compared to the medium used for live cell measurement in widefield modality, the RI of the imaging buffer in the SMLM modality is more prone to change from evaporation due to high electrolyte and glucose concentration (see section 3.7.5) such that 100 μL of water loss out of 5 mL immersion medium per hour will cause a substantial change in RI and the subsequent focal point drifting, leading to more than 800 nm misalignment per hour (Fig. 3.13d). As the evaporation rate is highly dependent on real-time humidity and ventilation condition in the laboratory, which can not be controlled because the first one relies on the weather and the ventilation facility boots up sporadically, the calibration for the syringe pump rate should be regularly carried out.

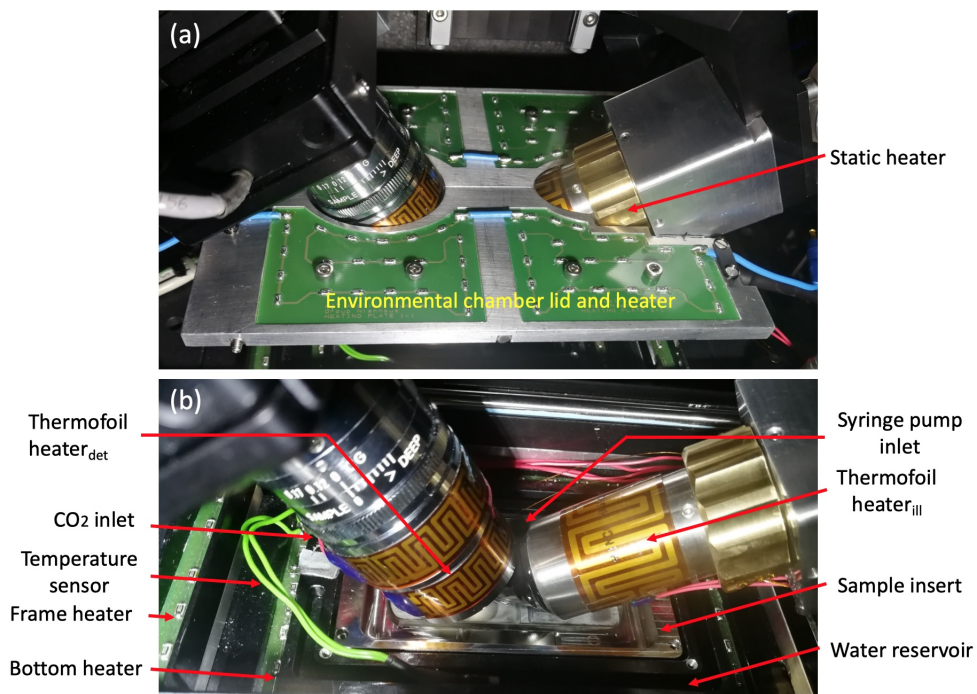


Figure 3.12: Images of the actual environmental chamber. (a) Closed lid on the top of the objective lenses. (b) Elements within the environmental chamber keep cells in physiological condition.

As with the method used before to inspect dynamic misalignment, I investigated static misalignment over time. Preliminary observation of the static misalignment with 200 μL per hour water refilling rate upon adding thiol groups and oxygen scavenging catalyst into the base buffer shows a peak at around 40 min (Fig. 3.13c), indicating the RI change is predominated by the oxidation reactions discussed in section 2.3.2 during the first half hour. After the reactions reach the equilibrium state, the dropping RI implies water refilling prevails over evaporation. To avoid the dramatic RI change induced misalignment, around 30 min waiting time is advisable. A proper water refilling rate allows temporally constant static misalignment as shown in Fig. 3.13a. Typical refilling rates for my imaging buffer (section 3.7.5) with 1.3499 initial RI at 21.5 ± 0.5 $^{\circ}\text{C}$ and with 30 ± 5 % humidity varies from 100 to 200 μL per hour.

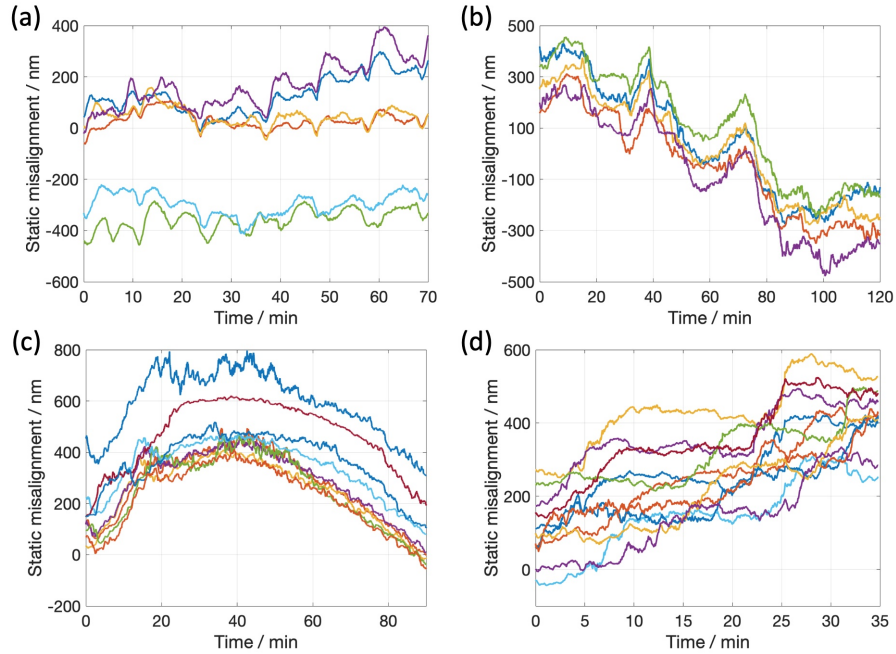


Figure 3.13: Measurement of misalignment between the light sheet and detection PSF over time with varying refilling rates. (a) Water refilling properly compensates for evaporation losses. (b) Water refilling overcompensates for evaporation losses. (c) RI change at different reaction stages in the presence of evaporation and water refilling. (d) Water refilling undercompensates evaporation losses. Each curve in one subplot represents a single fluorescence bead located at different positions. Offsets between curves imply the light sheet is slightly tilted in y direction. Varying water refilling rates were used for each experiment. Imaging buffers in (a) (b) and (d) were left reacting for half an hour before measurements while the measurement was started immediately upon adding the imaging buffer to the sample in (c).

3.4 Microscope characterization

3.4.1 Stability evaluation

Jittering

Regardless of four vibration isolators (S-2000 StabilizerTM, Newport, Irvine, California, United States) deployed, pronounced jittering present in fluorescence beads images with 1 ms frame exposure time as shown in Fig. 3.14a, deteriorated the widefield PSF quality and localization precision in SMLM modality. Fourier spectrum analysis provides the fingerprints of the noise as shown in Fig. 3.14c. We have identified the source of 36 Hz belonging to the water cooling system for cameras, lasers, and drivers of SLMs. The tiny contact of tubes to the optical

breadboard conducted substantial vibration of the cooling pumps lying on the floor. We overcame this problem by decreasing the pump revolutions per minute to mitigate vibration and mediating the pump and thermal sink on the optical table with two pieces of soft and elongated tubing linked via a heavy thermal dissipater to dampen the jittering conducting along the tubes. Further measures to isolate other jittering sources presumably originating from the cooling fans of the PC (100 Hz) and the building (3.6 Hz) that conducted to the breadboard through stiff and tensioned umbilical cables were relocating periphery equipment to release cables from tension and dampening the cables by firmly fastening them to a heavy table or metal blocks. After the optimization, most of the vibrational modes diminished substantially in amplitude or disappeared (Fig. 3.14b and d).

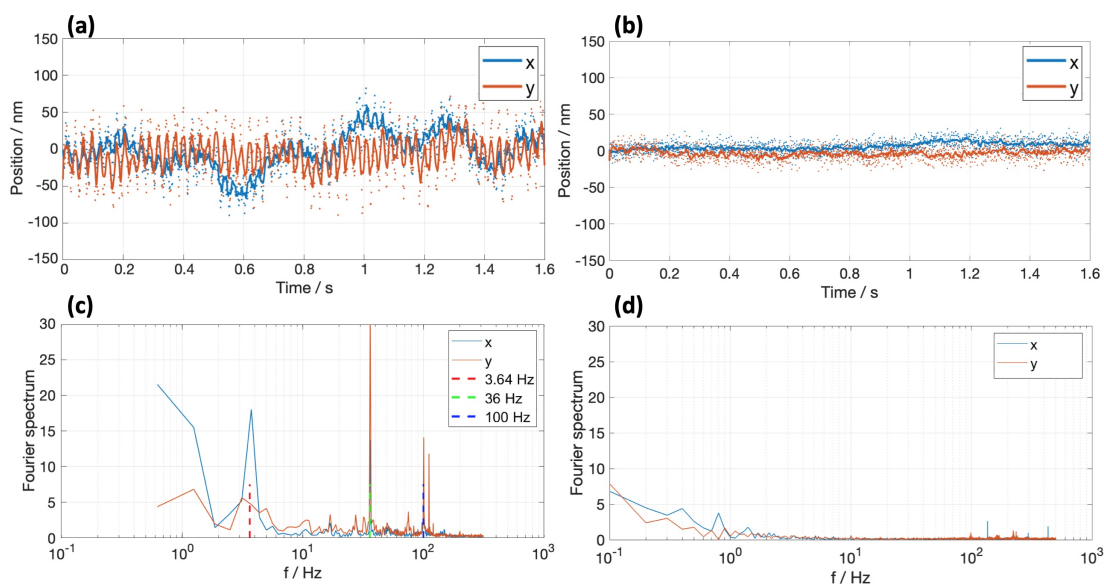


Figure 3.14: Jittering characterization. Time traces of fluorescent beads immobilized on the coverslip before (a) and after (b) optimization. The energy spectra of time traces before (c) and after (d) optimization.

Drifting

Due to mechanical relaxation and the piezo actuator creeping in open-loop mode, the sample constantly experiences drifting during acquisition. Cross-correlation is a simple yet effective method to correct for drifting up to voxel-level precision [70, 106], and is implemented to correct data with widefield resolution, for instance, the time-lapse measurement using SPIM modality. The target here is to register volumes acquired later to the coordinate of the first volume. The lateral correction vector is obtained by always cross-correlating two adjacent volumes considering the live cells are undergoing morphological change over time. However, this strategy is vulnerable to cumulative correction error, especially in the axial direction

where the sampling rate is typically four times lower than lateral. A trade-off way is cross-correlating the current and first volumes to get the correction vector.

Albeit the cross-correlation method can also be employed in the SMLM modality with modifications[75, 107, 108], a proper segmentation size has to be empirically chosen according to the labeling density and drifting velocity. Moreover, it is challenging for both memory and computational power to cross-correlate upsampled 3D super-resolution data. Therefore, fluorescent beads as fiducial markers are introduced for drift correction in the SMLM modality. To speed up the acquisition process, only a small ROI barely covering the cell of interest is selected, for example, $20 \times 20 \times 5 \mu\text{m}^3$. At least two-fifths of the cell would drift out of the ROI after 80 min should the drifting shown in Fig. 3.15a reoccur.

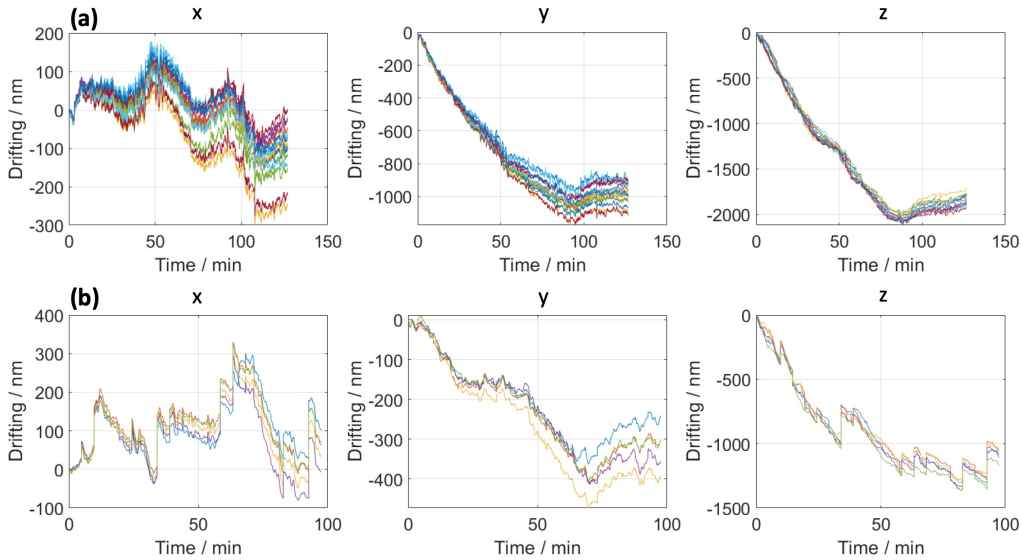


Figure 3.15: Drifting curves of immobilized fluorescence beads. (a) Drifting curves without quasi-close-loop correction. (b) Drifting curves with quasi-close-loop correction. Each curve in one subplot represents a single fluorescent bead located at different positions within the observation volume. The divergent curve bundle can be explained by the hysteresis of the objective lens piezo stage (see section 4.3.2).

The drifting shown here is mainly contributed by the sample piezo stage, whose movement axis is denoted as z_{bio} (Fig. 3.7) with minor contributions from motor-driven stages. Although the closed-loop mode of the piezo stage could eliminate creeping, it also comes with ringing at the same time. We implemented a quasi-closed-loop control strategy to approximately bring the sample stage back to the start position at the end of each hyperstack in fast acquisition mode by reading out the current position from the sensor output and adaptively updating the positioning command applied to the piezo actuator. This correction halved the

z drifting that could have exceeded $-2 \mu\text{m}$ as shown in Fig. 3.15b. The detailed correction procedure using fiducial marker drifting curves will be discussed in section 4.3.3.

3.4.2 PSF evaluation

SPIM modality

With all the alignment and aberration correction work done, the PSF_{det} of 100 nm yellow-green fluorescent beads fixed in agarose gel was measured. The Bessel light sheet was used for this measurement to imitate a widefield epi-illumination. Because only the detection objective is scanned, bulk illumination is preferable so as to include more beads in an ROI. As shown in Fig. 3.16a, 60 beads scattered across two $99 \times 104 \times 40 \mu\text{m}^3$ volumes are averaged and a value of $1.14 \pm 0.09 \mu\text{m}$ FWHM of PSF_{det} in axial direction is obtained. The deviation is also within a reasonable range, indicating a spatially invariant PSF_{det} over a large FOV.

Several factors account for the FWHM deviation from the theoretically predicted values in Eq. 2.13 and 2.23. The physical BFA position of the detection objective lens is located inside the objective barrel, 51 mm away from the focus plane. Since the light after the BFA is divergent, the following mechanical aperture should have been enlarged. However, the mechanical apertures of around 75 mm away from the BFA are only as large as the nominal BFA size, resulting in a NA_{eff} of less than 1.1.

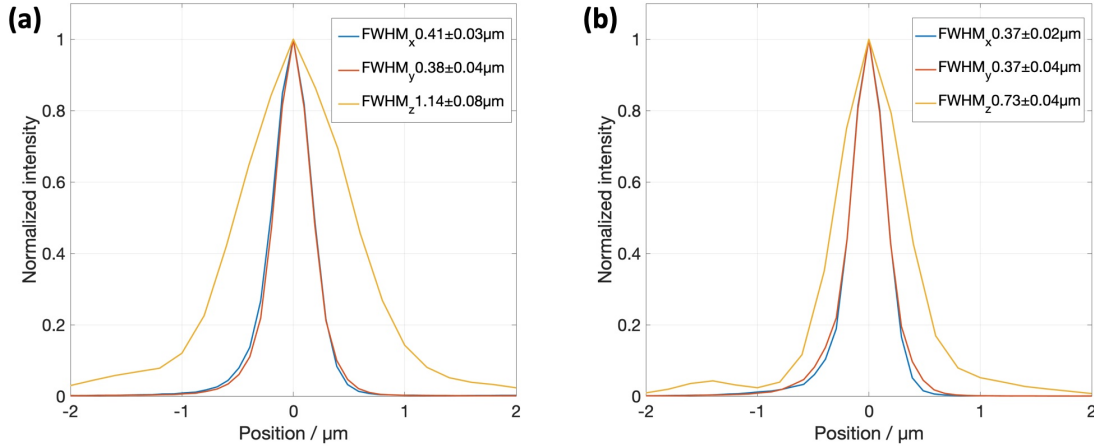


Figure 3.16: PSF calibration for SPIM modality. (a) Profiles of the detection PSF in x , y and z directions. (b) Profiles of the overall PSF in x , y and z directions.

As for the overall PSF, the hexagonal lattice with a NA of 0.32 is selected as an excitation lattice to allow a trade-off between a large FOV ($34 \mu\text{m}$) and a

small light sheet thickness (FWHM 5 μm) as discussed before in section 3.2. The hologram for the hexagonal lattice features 3 lobes as shown in Fig. 3.5c. The averaged overall PSF is then given as the summation of 60 beads out of three narrow volumes $48 \times 170 \times 40 \mu\text{m}^3$. A deviation of less than 100 nm in the axial direction illustrates the propagation-invariant characteristics of the lattice light sheet in the FOV. The axial FWHM is improved to 0.73 μm in comparison to the previous value of 1.14 μm of the PSF_{det} . A reduced average FWHM in x direction to 0.37 μm (Fig. 3.16b) further demonstrates the spatially variant clipping effect on the fluorescent signal by the limited mechanical aperture right behind the detection objective lens. Note that the experimentally measured PSF_{tot} is the true PSF_{tot} in the formation of the image, which should be the basis for post-processing operations such as deconvolution.

SMLM modality

Astigmatic aberration has to be artificially introduced in the detection path for 3D SMLM. In lieu of inserting a cylindrical lens between the tube lens and the camera as reported in the literature [75] that will bring in appreciable focal plane shifting in z direction, I generate tunable astigmatism by rotating L8 (Fig. 3.7) mounted on a rotational mount with 5 arcmin resolution in the vernier scale. For a well-aligned detection path where the fluorescence light ray intersects the rotational axis of L8, no other adverse effect shall be observed when rotating L8 apart from the slight shifting of the FOV in the lateral direction, thus allowing for freely switching between SMLM and widefield modalities.

I calibrated the PSF with astigmatism by imaging 100 nm red fluorescent polystyrene particles fixed on the surface of the coverslip. In virtue of the broad emission spectrum of these nanoparticles (see section 4.2.2), a sufficiently high number of photons on both cameras was observed using a 650 nm longpass dichroic mirror and 532 nm laser excitation. Therefore, the bleed-through signal of the red nanoparticle is a good approximation to the dark red fluorescence, which will be used in SMLM measurements. Bright and monodisperse nanoparticles were manually selected and positioned at 9 different areas within the ROI where the lattice light sheet exhibits diffraction-free properties. At each position, a single nanoparticle was imaged 6 times on each camera with 30 ms frame exposure time, 10 nm step size of the objective lens piezo stage, 500 steps, and a fixed light sheet. In total 54 detection PSFs were separately corrected with respect to photobleaching followed by background subtraction, upsampling and registering using the cross-correlation method (section 3.4.1). The averaged detection PSF was then downsampled to the final calibrated PSF. Notably, a low SNR of the calibrated PSF undermines the fitting performance because the noisy pixels will break the monotonicity of the PSF model to be introduced in section 3.5.3 and lead to a local minimum in the fit. Therefore, for the 16-bit images, the brightest pixel of the calibrated PSF should preferably be above 2,000 analog to digital

units (ADU).

The calibration protocol for the excitation PSFs was the same as for the detection PSFs except for the illumination configuration. Square lattices with $0.2 NA_{\text{eff}}$ for both 532 nm and 640 nm excitations were used for their spatially invariant thickness. Dark red polystyrene particles with 40 nm diameter were used for 640 nm excitation PSF. Instead of scanning the piezo stage, the z -galvo mirror was scanned while the piezo stage was fixed. Thus the brightness of the PSFs in different frames was modulated by the z profile of the scanning lattice. To account for apparent drifting, 54 single-peak PSF_{exc} profiles were aligned and averaged to get the final calibration of a one-dimensional PSF_{exc} .

To justify the merit of the lattice light sheet, the z profile of 640 nm Gaussian light sheet with its waist similar to the main lobe of the lattice was measured at different positions along the propagation direction. As shown in Fig. 3.17a the Gaussian light sheet exhibits gradually expanding thickness away from the waist, while the lattice light sheet maintains its thickness over a 30 μm ROI, in which the excitation PSF is regarded invariant.

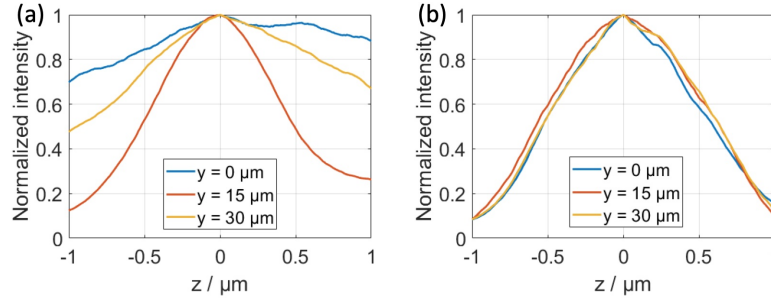


Figure 3.17: Excitation PSF calibration for SMLM modality. (a) PSF z profiles for 640 nm Gaussian light sheet. (b) PSF z profiles for 640 nm lattice light sheet. Light sheet thickness was measured every 15 μm along the propagation direction.

Astigmatism manifests itself in the orientation of the elongated PSF at opposite defocusing directions as shown in Fig. 3.18a and c. The asymmetry of astigmatism can be measured by the slope of the FWHM ratio in the x and y directions, σ_x/σ_y , which increases with the rotational angle at the cost of spreading PSF as the FWHMs at the in-focal plane become larger compared to aberration-free PSFs (Fig. 3.16). Indeed enhancement in PSF asymmetry implies higher z localization precision, one should heed the downside that the spreading PSF inevitably compromises the SNR per pixel that in turn affects localization precision. Notably, the short wavelength is more liable to rotation-driven astigmatism such that the PSF for the yellow channel totally loses the tight focus at $z = 0$ in attempting to enhance astigmatism for the dark red channel. In the spirit of maximizing z localization precision in the dark red channel and avoiding the risk

of difficulty in segmenting PSFs devoid of focal points in the yellow channel, a critical rotational angle is chosen such that the focal point for the yellow channel is on the verge of disappearing. Eventually, the rotational angle in the following experiments is optimized to 4 degrees.

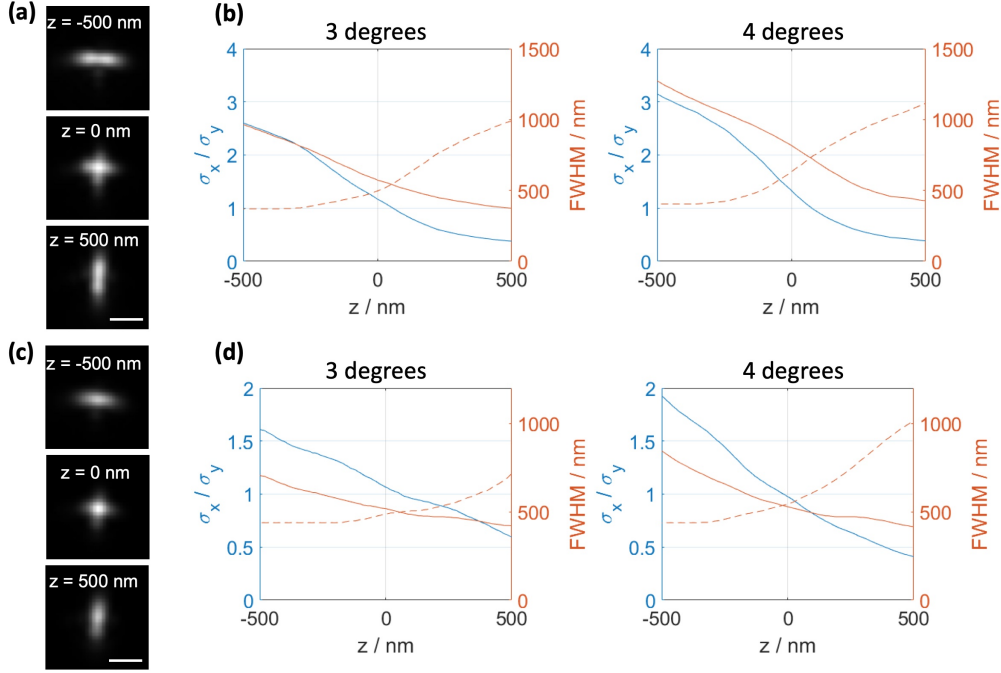


Figure 3.18: Detection PSF calibration for SMLM modality. Astigmatic PSF images for the yellow channel (a) and dark red channel (c). Astigmatism was created with 4 degrees rotation for (a) and (c). FWHM profiles in x (solid line) and y (dashed line) directions and their ratio with different rotational angles for the yellow channel (b) and dark red channel (d). Scale bar 1 μm .

3.5 SMLM algorithms

3.5.1 sCMOS camera pixel reading model

sCMOS cameras have been widely employed in the field of SMLM, as their parallel readout architecture allows for high frame rates and, therefore, makes video-rate throughput of super-resolution images on living samples possible. Actually, the high frame rate is traded for a low exposure time that inevitably limits the detected number of photons per emitter given a constant excitation intensity, leading to a poor SNR and low localization precision in turn, as discussed in section 2.2.4.

Another effect that weakens the localization performance is the pixel dependent readout noise ranging from several ADU square to more than one thousand

ADU square. The random occurrences of hot pixels will severely influence the localization precision if not properly treated in the fitting algorithm. Although improving the detection efficiency, utilizing fluorophores with higher quantum efficiency and increasing the excitation intensity can enhance the SNR, all of those endeavors have a smaller effect compared to the order of magnitudes modulation of the signal level obtained when pushing the exposure time from tens of milliseconds to hundreds of microseconds or even shorter. In practice, incorporation of the camera model into the fitting algorithm is more advisable and cost-effective to minimize readout noise. To this end, intimate knowledge of the camera noise model is required.

The ADU generation can be decomposed into multiple stages, along with which diverse sources of noise kick in and contribute to the ADU reading. During the course of the exposure, a train of photons originating from the ambient environment, background excitation as well as emitters in the focal plane hit the photodiode on the sensor that turns photon counts into an accumulated charge on a capacitor. Shot noise is the collective photon count fluctuation around the expected number of photons due to their quantum nature. But even in the absence of photons, the capacitor is still not void of charge. This is the consequence of operating at ambient temperature, so that thermal fluctuations in the semiconductor give rise to free electrons, denoted as dark current, exponentially increasing with temperature. Thanks to Peltier elements attached to the camera chip, the working temperature is maintained at $-20\text{ }^{\circ}\text{C}$, hence, the thermal or conductive noise is almost negligible. In the conversion stage, the amount of charge on the capacitor is measured by a pixel-based amplifier circuit with a reduced intrinsic gain factor of less than $10\text{ ADU}/e^-$ due to a highly restricted transistor channel length on the chip having as many amplifiers as the number of pixels integrated. The most prominent noise contribution is the readout noise occurring in the amplification stage. Every attempt to measure a physical quantity comes with an error, measuring amplified voltage is not an exception. The amplitude of the fluctuation can be characterized by a normal distribution with a variance depending on the manufacturing process of the amplifier circuit. Following the amplification is the analog-to-digital conversion performed in parallel by two columns of A/D units on the top and bottom of the chip. In order to avoid negative ADUs, especially when the variance of the readout noise is greater than the photon counts, a constant offset is applied to the ADU.

As the readout noise is independent of photon counts, the probability density function (PDF) of the output ADU represented by D for an arbitrary pixel can be expressed as[69]

$$P(D|q) = \frac{1}{\sqrt{2\pi\text{var}}} e^{-\frac{(D-q\cdot\text{gain}-\text{os})^2}{2\text{var}}}, \quad (3.12)$$

where var, os and gain represent the variance of the readout noise, offset and

gain, respectively. q is the number of photons impinging on the concerned pixel. The photon statistics for a single emitter is characterized by the second-order autocorrelation function at zero delay time, $g^{(2)}(0) = 1 - 1/\langle n \rangle$ with photon number operator $n = a^\dagger a$. Provided a sufficiently large number of photons within a given exposure time can always be detected by increasing the re-excitation rate, the autocorrelation function asymptotically approaches one, leading to a Poisson process for photon detection [109].

As shown in Fig. 2.12a, photons from a single molecule will be distributed over a pixel grid. The photon statistics on the i^{th} pixel complies with a binomial distribution $B(Q, \gamma)$, where Q is the total number of photons emitted by the single molecule and

$$\gamma = \frac{\int_{S_i} h_{\text{tot}} dx dy}{\int h_{\text{tot}} dx dy}, \quad (3.13)$$

where S_i denotes the area covered by the i^{th} pixel and h_{tot} is defined by Eq.2.22 in section 2.2.3. If Q is sufficiently large while γ is close to zero so that $\gamma \cdot Q$ is larger than 1 but much smaller than infinity, the binomial distribution can be approximated as a Poisson distribution with parameter $\gamma \cdot Q$. The overall probability of observing q photons on the i^{th} pixel is the summation of the product of two Poisson distributions,

$$P(q) = \sum_{Q=0}^{\infty} P(q|Q) \cdot P(Q) = \sum_{Q=0}^{\infty} \frac{e^{-\gamma Q} (\gamma Q)^q}{q!} \cdot \frac{e^{-N} N^Q}{Q!}, \quad (3.14)$$

where N is the expected number of photons emitted by a single molecule, *i.e.* $N = \langle Q \rangle$. It can readily be proven that, when γ approaches zero, the photon statistics on the i^{th} pixel can be approximated as a Poisson distribution,

$$P(q) = \frac{e^{-\mu} \mu^q}{q!}, \quad (3.15)$$

where $\mu = \gamma \cdot N$, implying the expected number of photons detected by the i^{th} pixel, which depends on the location of the pixel in the PSF.

The overall PDF for the ADU reading can be written as the summation of the conditional probability of the Gaussian noise (Eq. 3.12) and Poissonian signal (Eq. 3.15) over the detected photon number q [69],

$$P(D) = \sum_{q=0}^{\infty} P(D|q) P(q) = \sum_{q=0}^{\infty} \frac{1}{q!} e^{-\mu} \mu^q \frac{1}{\sqrt{2\pi \text{var}}} e^{-\frac{(D-q \cdot \text{gain} - \text{os})^2}{2\text{var}}}. \quad (3.16)$$

By rearranging the exponential term as

$$\exp \left\{ \frac{-[(D - \text{os})/\text{gain} + \text{var}/\text{gain}^2 - \text{var}/\text{gain}^2 - q]^2}{2\text{var}/\text{gain}^2} \right\} \quad (3.17)$$

and substituting $(D - \text{os})/\text{gain} + \text{var}/\text{gain}^2$ for D , Eq. 3.16 is rewritten in exactly the form of a convolution between a normal distribution $\mathcal{N}(\cdot, \cdot)$ and a Poisson distribution $\mathcal{P}(\cdot)$

$$P((D - \text{os})/\text{gain} + \text{var}/\text{gain}^2) \sim \mathcal{P}(\mu) * \mathcal{N}(\text{var}/\text{gain}^2, \text{var}/\text{gain}^2). \quad (3.18)$$

For flawed pixels with $\text{var}/\text{gain}^2 > 10$, $\mathcal{P}(\text{var}/\text{gain}^2)$ is a good approximation to $\mathcal{N}(\text{var}/\text{gain}^2, \text{var}/\text{gain}^2)$. According to the property of the convolution of two Poisson distributions, Eq. 3.18 is approximately written as

$$P((D - \text{os})/\text{gain} + \text{var}/\text{gain}^2) \sim \mathcal{P}(\mu + \text{var}/\text{gain}^2). \quad (3.19)$$

In this way, the camera-related parameters are incorporated into an analytical expression of the Poissonian PDF to be used in the fitting algorithm later. For normal pixels with small variance such that the convolution is negligible, Eq. 3.18 and 3.19 consistently reduce to a single parameter Poisson distribution.

Our next task is to calibrate the offset, variance and gain values for all pixels. To account for the fact that Eq. 3.16 reduces to a normal distribution dependent on offset and readout noise if no photon is detected, 60,000 full-frame dark images are acquired and the offset map can be calculated pixel by pixel via the equation

$$\text{os}_i = \frac{1}{K} \sum_{k=1}^K D_i^k, \quad (3.20)$$

where D_i^k is the ADU reading of the i^{th} pixel on the k^{th} frame, and K is the total number of frames. Then, the readout noise can be calculated as

$$\text{var}_i = \frac{1}{K} \sum_{k=1}^K (D_i^k)^2 - \text{os}_i^2. \quad (3.21)$$

Determining the gain is not as straightforward as that of offset and variance because a temporally uniform illumination is required to guarantee a fixed average number of photons in an equivalent period of time during the course of acquisition, which is demanding in view of the incessant power fluctuation of the light

source, for instance, a solid state laser under the control of an electronic driver. Fortunately, our 405 nm laser exhibits an operating regime where fluctuations are minimal. I carefully adjusted the power output and attenuated the beam with a neutral density filter to create a gradient of illumination intensity. The expanded and collimated laser is projected onto a piece of thick white paper right in front of the camera sensor to create a uniformly scattered light pattern. Four sequences of full frame bright images (20,000 frames each) were captured with evenly spaced intensities to ensure that 20-200 photons were detected per pixel.

The estimation of the gain is as follows. Calculating the expectation value and the variance of the variable $(D_i - os_i)/gain_i + var_i/gain_i^2$ and canceling μ_i yields the equation

$$Var[D_i] - var_i - gain_i(\bar{D}_i - os_i) = 0, \quad (3.22)$$

where $Var[D_i]$ and \bar{D}_i denote, respectively, the variance and mean of the i^{th} ADU reading over 20,000 frames. Being independent of photon count, the unbiased estimator of the gain should guarantee Eq. 3.19 to hold for arbitrary photon numbers,

$$\hat{gain}_i = \arg \min \sum_{j=i}^4 (Var[D_i^j] - var_i - gain_i(\bar{D}_i^j - os_i))^2. \quad (3.23)$$

The \hat{gain}_i can be explicitly expressed by taking the partial derivative of the summation with respect to $gain_i$ and equaling it to zero,

$$\hat{gain}_i = (B_i B_i^T)^{-1} B_i A_i^T, \quad (3.24)$$

where

$$\begin{aligned} A_i &= \{Var[D_i^1] - var_i, \dots, Var[D_i^4] - var_i\}, \\ B_i &= \{\bar{D}_i^1 - os_i, \dots, \bar{D}_i^4 - os_i\}. \end{aligned} \quad (3.25)$$

The statistics of the full calibrated maps of offset, variance and gain are shown in Fig. 3.18. Since a realistic amplifier model is not supposed to decrease the photon count, I set the calculated gains < 1 to 1. The median of gain and offset agree well with the specifications provided by the manufacturer, validating this calibration method.

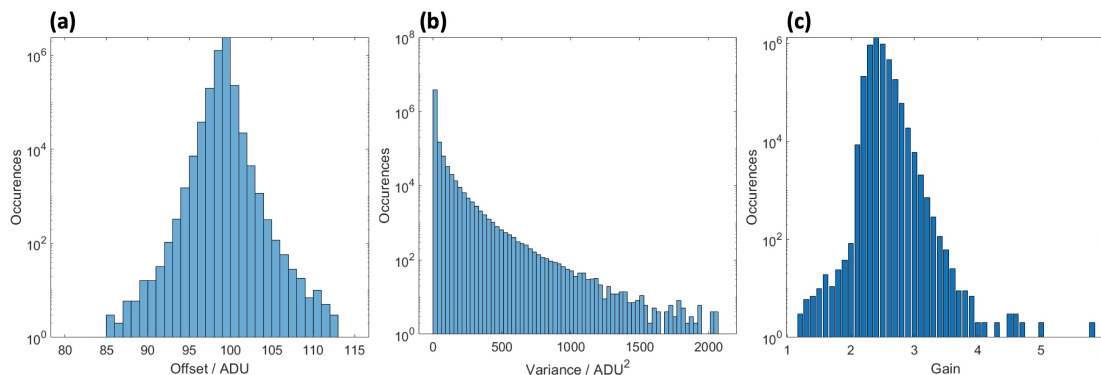


Figure 3.19: Calibration results of the 2048×2048 pixels of the sCMOS camera. (a) Statistics of the offset. (b) Statistics of the variance. (c) Statistics of the gain.

3.5.2 Global segmentation algorithm

It comes about naturally to take advantage of the merits of SPIM and SMLM to obtain thick and super-resolved volumetric data. However, so far all the applications of SMLM in SPIM geometry still fit a 2D emitter image to the 3D PSF regardless of the intrinsic 3D emitter pattern appearing in several consecutive slices [23]. In doing so, one emitter will be repeatedly localized multiple times with compromised axial localization precision for every single 2D localization. In practice, this should be avoided since it has been proven that globally fitting an emitter pattern at different focal planes for one coordinate can achieve quasi-isotropic localization precision [74]. The first practical difficulty of global fitting is the lack of segmentation algorithms for SPIM-generated data. Even though one can apply a cluster classification algorithm to 2D segmented data to collapse multiple segments belonging to the same emitter, this strategy is of low efficiency and computationally expensive. On top of that, the cluster classification algorithm itself is prone to error. For densely populated raw data, simply combining two algorithms would be far from optimal. Another difficulty impeding global fitting is how to incorporate the light sheet-related parameters into the fitting algorithm.

In the following part of the algorithm section, I first put forward a one-stop segmentation method for SPIM-produced 3D image stacks, especially suitable for low SNR data. In the next subsection, I present a global fitting algorithm taking into account the sCMOS model and the light sheet configuration for volumetric data. At last, simulated results are presented to validate the method.

Signal enhancement

There are two typical errors in the process of segmentation. False positive refers to a segment thought to contain a single emitter (represented by black crosses in Fig. 3.20), while there is none. False negative refers to a single emitter that the

segmentation algorithm fails to identify (red pentagrams in Fig. 3.20). Contrary to those errors are true positives marked by green crosses in Fig. 3.20 and true negatives. Sensitivity, also known as positive rate defined as the ratio between the true positive instances and all positive instances in the pool,

$$\text{sensitivity} = \frac{\text{true positives}}{\text{true positives} + \text{false negatives}}, \quad (3.26)$$

measures the ability of the segmentation algorithm to retrieve positive instances. Specificity, as another standard metric describing the rejection rate of negative instances for a classifier, is defined as the ratio between the true negative instances and all negative instances in the pool,

$$\text{specificity} = \frac{\text{true negatives}}{\text{true negatives} + \text{false positives}}. \quad (3.27)$$

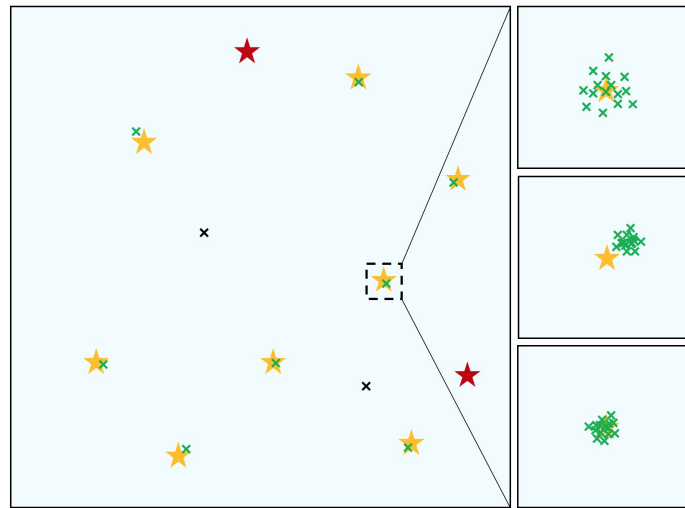


Figure 3.20: Illustration of the metrics of the segmentation and localization algorithm. Pentagrams mark the emitters to be segmented, of which orange ones labeled with green crosses are true positives while red ones are false negatives. Black crosses represent false positives. The localization performance can be characterized by the cloud of localizations to a particular emitter. The upper panel on the right indicates high localization accuracy as the centroid of the cloud coincides with the emitter, but poor precision as the cloud is broad. The cloud featuring the smaller standard deviation in the middle panel exhibits high localization precision but low accuracy due to a displaced centroid. The point cloud in the lower panel shows both high localization precision and accuracy.

Considering the instances to be classified in the segmentation scenario are not countable, especially negative instances, a proper assumption has to be made for

practical calculation. It is reasonable to suppose the total number of instances is equivalent to the ratio of the dataset volume to segment size, given that the former is much larger than the latter. Thus, the number of negative instances equals the difference between the total and positive instances.

A good segmentation classifier should simultaneously maximize sensitivity and specificity or, in other words, minimize false positive and false negative errors. In reality, a compromise has to be made due to the fact that segmentation algorithms tend to, in the presence of noise, lose specificity if conditioned toward high sensitivity. As a result, pre-processing is indispensable in a segmentation workflow to smooth out noise.

A Gaussian filter is a suitable tool for this task. However, it will bring about pseudo-emitters around pixels with high readout noise, if an sCMOS camera is used. To avoid false positives arising from this effect, a 2D 3×3 median filter preceding the Gaussian filter is applied to the raw data. Following the median filter, a user-defined 3D Gaussian filter is applied, which adaptively takes into account the voxel size and the resolution. The resulting image stack consists of a smoothly varying background and expanded single emitters. Inspired by the super-resolution radial fluctuation method [110], a 2D or 3D Laplacian filter, depending on signal level, is applied to the Gaussian-filtered images for two purposes. Firstly, it is reasonable to assume that a slowly varying background can be approximated by a low-order Taylor expansion, which can almost be eliminated by the Laplacian operation. Secondly, single emitters will be sharpened by a Laplacian filter in such a way that the height of the peak remains invariant while the FWHM shrinks. This operation is beneficial for raw data with dense emitters. After the outlined three-step sequential filtering, the noise and background are substantially suppressed while the signal contrast is enhanced, as illustrated in Fig. 3.21.

Thresholding segmentation workflow

Defining a cube centered at a local maximum is the simplest way to determine a segment candidate that will later be assessed and classified as positive or negative. Among the investigated metrics to assess if a segment qualifies as a candidate containing an emitter, the statistics of the ADU values within the segment has been proven to be robust yet sensitive for low SNR data, especially if the PSF sampling rate is low. In the preliminary simulation, for instance, the measure of Gaussian-fitted 3D FWHM was tested as a metric in emitter qualification. With a critical sampling rate that a PSF is covered by 10×10 pixels, Gaussian fitting exhibits a big fitting uncertainty, leading to low specificity and sensitivity.

The desired metric is defined as the number of voxels within the segment whose ADUs are larger than half of the maximum ADU determining the center of the respective segment. Assumptions about the quality of the raw data have to be made in order to validate the metric. Firstly, the concerned data are supposed

to exclusively contain single molecules rather than structures in any other form, because, for instance, a periodic structure with high spatial frequency cannot be ruled out by the Laplacian filter and hence will bring in false positive segments. Secondly, the step-wise filtering operation substantially suppresses noise and background and relies on the assumption that the voxels around local peaks contain no signal.

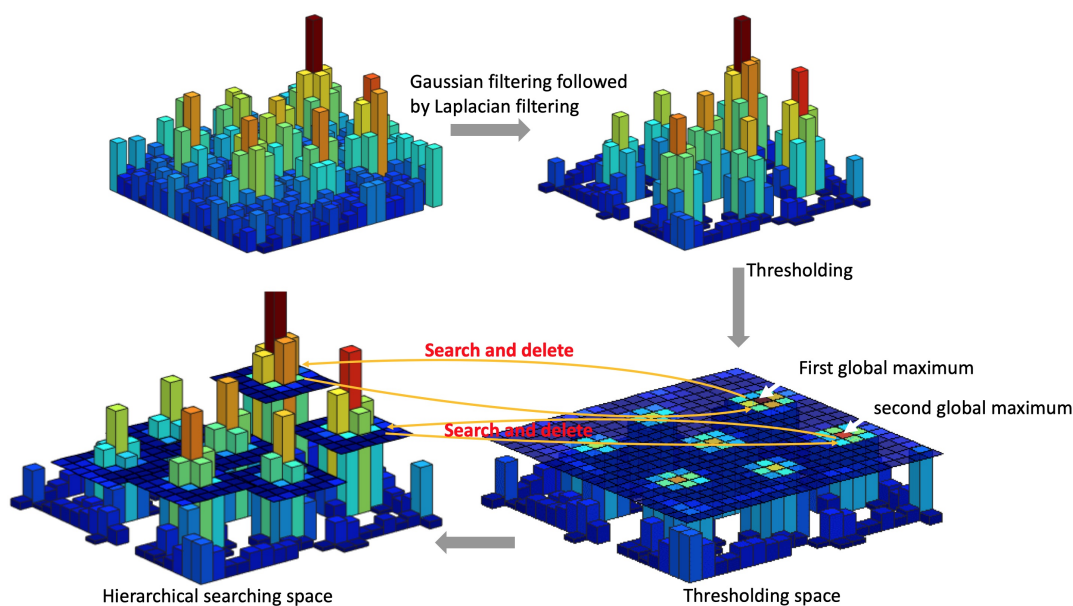


Figure 3.21: Schematic of the segmentation workflow. The raw data are preprocessed using a Gaussian filter followed by a Laplacian filter. The thresholding space possibly containing emitters is determined as the cross-section of a thresholding hyperplane and the volumetric data. Selecting the hyperplane centered on the current global maximum voxel within the thresholding space, with its height being half of the global maximum defines a continuous segment in search space, whose volume is compared against the benchmark. Whether or not this segment is accepted, all voxels within it are deleted from thresholding space and the process is repeated until the thresholding space is depleted.

A benchmark value of the metric, against which the measure of the real data is compared, is created by simulated data under exactly the same conditions the measured data are acquired. This includes the NA , the magnification, the camera pixel size and the axial step size. The simulated data are then given by a set of segments, each of which has one Gaussian-shaped emitter with its axial position being in-between ± 0.5 steps. Such a dataset can account for all possible occurrence positions of a segmented emitter around the center of the segment. A step-wise filtering operation is applied to the simulated segments, followed by calculating the lower bound for the benchmark, which is the minimal metric of all

processed data sets. Finally, a realistic segment with its metric measuring greater than the benchmark is assumed to contain an emitter and vice versa.

As with all other segmentation methods, the thresholding procedure is inevitable to determine candidate segments. To this end, I have implemented a hierarchical search scheme to define candidate segments. An $11 \times 11 \times 5$ subvolume is defined with $100 \times 100 \times 400$ nm³ voxel size and 1.1 *NA* detection objective lens such that it allows for only one emitter being completely encompassed in the small hyper-plateaus shown in the hierarchical search space in Fig. 3.21. Then, the post-processed image stack is subjected to thresholding, the voxels with ADU above which are picked out and stored in an array termed thresholding space (Fig. 3.21) together with their corresponding coordinates. The candidate segment centered on the current global maximum ADU is clipped out of the post-processed data and tested. Whether or not this candidate segment is accepted to contain an emitter, the voxels satisfying the requirement to be above the threshold and inside the current candidate segment are deleted from the array. The global maximum is iteratively selected from the reduced array, and the candidate segment centered around the current global maximum voxel is tested until the size of the array reduces to zero. It can be foreseen that a small threshold dramatically increases false positives as the consequence of smoothed yet significant emitter-like peaks originating from the filtering of readout noise. A trade-off solution is to select a threshold smaller than the optimal one to gain sensitivity at the cost of specificity. The returned CRLB and likelihood values of false positive segments in the fitting stage will be significantly larger compared to those of true positive segments and thus can be readily sorted out.

Generation of simulated data

In order to justify the validation of my segmentation method, I first tested it on simulated single emitter data by randomly distributing points convolved with the PSF with aberration in an image stack. The three-dimensional detection PSF is calculated using the method given in section 3.1. In light of innate systematic aberration in the detection path, spherical aberration Z_{11} and coma aberration Z_8 are included in the simulation in addition to astigmatic aberrations $Z_{5,6}$. As for the excitation PSF, I employed a hexagonal lattice with $NA_{\text{eff}} = 0.4$. The overall PSF is the product of two PSFs with 300 nm misalignment, which is similar to the real experimental condition because misalignment around 250 nm happens from time to time during the measurement as a consequence of mechanical drifts of optical mounts.

The simulated overall PSF is sampled in a $5 \times 5 \times 5$ nm³ voxel size volume, whose brightest frame is then 20×20 binned starting from the emitter center, followed by normalization. In doing so, the latent pixelation error in numerical calculation is minimized. To approximate a real experimental scenario, I empirically take 30 ADU above the background, which is the brightest pixel of an emitter, as the

lower bound to make this emitter prominent within the noise. Dividing this value by the gain factor yields the number of photons detected by the brightest pixel. The total number of photons is obtained by integrating over all pixels in the center slice of the PSF with respect to photon count. A constant conversion factor of 6.2 relates 30 ADU of the brightest pixel to 185 photons in total. I use this number of photons as a benchmark for the following part of the simulation. I designate an average number of photons to emitters in each set of the simulated data, which is a fraction or integer times the benchmark photon number.

In order to make the simulated data more generic, such that they cannot only be used for testing segmentation performance but also for the localization algorithm, I randomly scattered 200 overall PSFs with $621 \times 621 \times 241$ voxels in a blank volume with $5120 \times 5120 \times 100$ voxels. The voxel size of the PSF is $5 \times 5 \times 5 \text{ nm}^3$ while the blank volume is $5 \times 5 \times 400 \text{ nm}^3$, meaning the PSF volume in axial direction will be down-sampled every 80 frames. Thus, the ground truth coordinates of all 200 emitters are known with a precision of 5 nm. Lateral binning yields the realistic volumetric data with $256 \times 256 \times 100$ voxels and $100 \times 100 \times 400 \text{ nm}^3$ voxel size. A constant background is also added to the resultant binned data. As per Eq. 3.15, the photon statistics for each pixel is a Poisson-distributed variable with its expectation value being exactly the pixel values of the binned PSF. I substitute, for each pixel, the number drawing from a Poisson distribution, whose expectation value is the current pixel value for the current pixel value. Thus, the photon detection process is done. At last, the sCMOS camera model is employed to convert the number of photons to ADU reading by multiplying the cumulative photon map with the gain map and individually adding pixel-dependent Gaussian read-out noise to each pixel according to Eq. 3.12. The gain, variance and offset maps are obtained from preceding calibration results and will be used in the localization stage.

Evaluation of the segmentation performance

In this section, I describe simulations of 12 sets of data with the number of photons per emitter ranging from 100 to 11,800. Except for the number of photons, all other parameters are identical. Each set of data consists of 10 randomly generated image stacks containing 200 sparse emitters. It is worth mentioning that a fluctuation of the emitter brightness in the same data set is the consequence of the random photon number and the random position of the emitter with respect to the light sheet position. If an emitter happens to be located at the light sheet plane, it will appear brightest. Contrarily, it will be dark if the emitter is located between two adjacent light sheet planes. Actually, the real number of photons per emitter complies with the convolution of Poisson distribution and Gaussian distribution, provided the light sheet profile can be approximated as a Gaussian. All random processes introduced in the simulation make it resemble experimental data. The built-in Matlab[®] functions are used as random number generators.

As proposed in the signal enhancement section, I predefined sensitivity and specificity to evaluate the segmentation performance. Specificity and sensitivity are surveyed against threshold, using the data set with benchmark number of photons. As can be seen in Fig. 3.22, specificity rises in the beginning and asymptotically converges to 1 when the threshold is larger than 15. By contrast, the sensitivity is always above 0.97 and slowly decreases with increasing threshold. Here, I heuristically selected a threshold of 15 as the optimal trade-off between specificity and sensitivity.

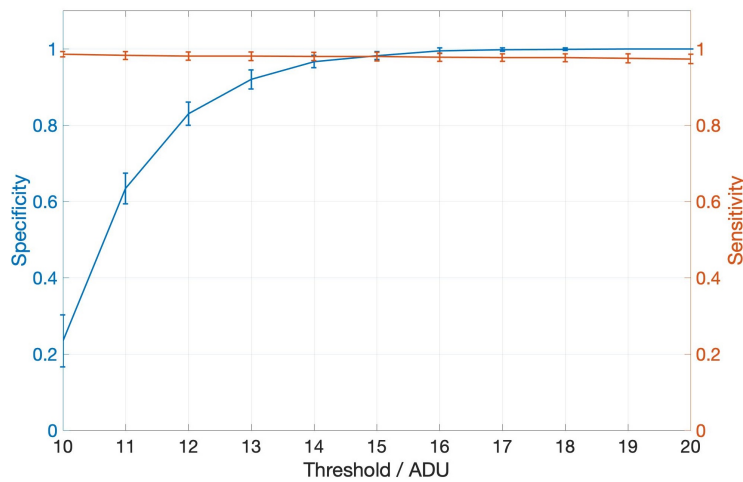


Figure 3.22: Specificity and sensitivity vs. threshold.

For the investigation into the influence of the number of photons on specificity and sensitivity, especially the threshold is meticulously selected for each data set to guarantee high sensitivity and specificity in the same time. As shown in Fig. 3.23, if the number of photons is above the benchmark, the segmentation method exhibits high performance. Even though the number of photons drops down to 97, both specificity and sensitivity nevertheless maintain high levels. However, one should avoid using emitters in this domain since, due to a lack of photons, the localization precision will be low. With the interference of noise, the localization method might then give large uncertainties. The reason why the sensitivity fluctuates around 0.97 and does not converge to 1 even with a high number of photons is rooted in the stochastic emitter placement, which cannot prevent overlapping emitters. The bumpy sensitivity curve with large error bars can also be explained by this effect and the lack of statistics. The hierarchical search scheme cannot tell apart overlapping emitters, which will in turn cause difficulty in the fitting stage and hence have to be avoided in real experiments by controlling the temporal population of single emitters residing in the on-state.

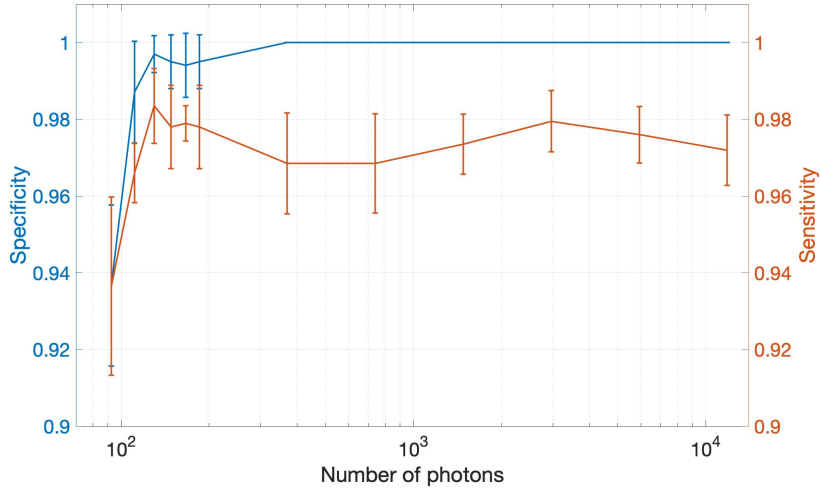


Figure 3.23: Specificity and sensitivity vs. photon number.

3.5.3 Global single molecule fitting algorithm

Formulation of the likelihood function

As can be seen from Eq. 3.16, the ADU reading is made up of Poissonian signal and Gaussian readout noise, the parameters of the latter are a priori knowledge from the camera calibration. The expectation value of photons for the i^{th} pixel μ_i can be expressed as

$$\mu_i = I \cdot \int_{x_i-a/2, y_i-a/2}^{x_i+a/2, y_i+a/2} h_{\text{tot}}(x - x_c, y - y_c, z - z_c) dx dy + bg, \quad (3.28)$$

where I denotes the brightness of the emitter; \mathbf{r}_i and \mathbf{r}_c are the coordinates of the i^{th} pixel and the center of the emitter. Owing to the pixelation of the PSF in the imaging process, the integral of the PSF over the area of individual pixels has to be performed. It will be proven later that the integral of the PSF with 400 nm FWHM over 97 nm pixels can be replaced by the value at the center of the pixel and vice versa. Therefore, Eq. 3.28 simplifies to

$$\mu_i = I \cdot h_{\text{tot}}(x_i - x_c, y_i - y_c, z_i - z_c) + bg. \quad (3.29)$$

The fitting goal is now to find the proper center coordinate \mathbf{r}_c , the brightness I and the background photon number bg so that the recorded single emitter data best resemble the model data. Those parameters are represented by the vector $\mathbf{v} = \{v_1, v_2, v_3, v_4, v_5\}$ with the following derivation. The maximum likelihood

estimation (MLE) method provides an unbiased estimator for the parameters in the Poisson distribution and hence is adopted in my work. A succinct substitution for Eq. 3.19 is

$$P(d|p) = \frac{1}{d!} e^{-p} p^d, \quad (3.30)$$

where d represents the observation of the random variable $(D\text{-os})/\text{gain}+\text{var}/\text{gain}^2$ and p the unknown parameter $\mu+\text{var}/\text{gain}^2$ to be fitted. The principle of MLE assumes that the most likely estimation, *i.e.*, $\hat{\mathbf{p}}$ of the target parameters maximizes the probability for the current observation,

$$\hat{\mathbf{p}} = \arg \max \prod_i P(d_i|p_i), \quad (3.31)$$

where the joint probability distribution takes into account all observations within the segmented volumetric data and is also known as the likelihood function $\mathcal{L}(\mathbf{d}|\mathbf{p}) = \prod_i P(d_i|p_i)$. Conventionally, the normalized logarithmic likelihood function will be minimized instead of maximizing $\mathcal{L}(\mathbf{d}|\mathbf{p})$ [111],

$$\chi_{\text{mle}}^2 = -2\ln(\mathcal{L}(\mathbf{d}|\mathbf{p})/\mathcal{L}(\mathbf{d}|\mathbf{d})) = 2 \sum_i (p_i - d_i) - 2 \sum_{i, d_i \neq 0} (d_i \ln(p_i/d_i)). \quad (3.32)$$

The second equality is obtained by substituting $\mathcal{L}(\mathbf{d}|\mathbf{p}) = \prod_i P(d_i|p_i)$ and $\mathcal{L}(\mathbf{d}|\mathbf{d}) = \prod_i P(d_i|d_i)$ into the left hand side and considering Eq. 3.30.

Fitting algorithm

Analytically searching in parameter space for a set of parameters \mathbf{v} that minimize χ_{mle}^2 is almost impossible. Therefore, iterative minimization schemes have to be employed for practical optimization problems. The Levenberg-Marquardt (L-M) algorithm will be adopted in this work for its efficiency and robustness [73, 111]. The principle assumes that, in the neighborhood of the minimal value of χ_{mle}^2 , χ_{mle}^2 is monotonic with respect to \mathbf{v} and can be expanded into a Taylor series around the current parameter set \mathbf{v}_{cur} ,

$$\chi_{\text{mle}}^2(\mathbf{v}_{\text{cur}} + \Delta\mathbf{v}) \approx \chi_{\text{mle,cur}}^2 + \nabla_{\mathbf{v}_{\text{cur}}} \chi_{\text{mle}}^2 \cdot \Delta\mathbf{v} + \frac{1}{2} \Delta\mathbf{v}^T \cdot \nabla_{\mathbf{v}_{\text{cur}}} \nabla_{\mathbf{v}_{\text{cur}}} \chi_{\text{mle}}^2 \cdot \Delta\mathbf{v} \quad (3.33)$$

Thus, χ_{mle}^2 is converted to a quadratic function with respect to $\Delta\mathbf{v}$. One can readily minimize χ_{mle}^2 by differentiating Eq. 3.33 in terms of $\Delta\mathbf{v}$ and setting it

to zero. Iteratively updating \mathbf{v}_{cur} with the newly obtained $\Delta\mathbf{v}$ results in χ_{mle}^2 to converge. However, the occurrence of the second derivative in $\nabla_{\mathbf{v}_{cur}} \nabla_{\mathbf{v}_{cur}} \chi_{mle}^2$ causes computational effort and instability. The L-M algorithm therefore ignores the second derivative term and modifies the updating scheme, stabilizing the convergency of χ_{mle}^2 to its minimal value. Eventually, $\Delta\mathbf{v}$ is calculated by omitting the second derivative term,

$$\alpha_{jk} \Delta v_k = \beta_j, \quad (3.34)$$

where

$$\alpha_{jk} = \sum_i \frac{\partial p_i}{\partial v_j} \frac{\partial p_i}{\partial v_k} \frac{d_i}{p_i^2}, \beta_j = - \sum_i \left(1 - \frac{d_i}{p_i}\right) \frac{\partial p_i}{\partial v_j}. \quad (3.35)$$

Only if the updated χ_{mle}^2 fails to decrease, the diagonal elements of the matrix $\boldsymbol{\alpha}$ will be increased by a factor of $(1+\lambda)$ [112],

$$\alpha'_{jk} = \alpha_{jk}(1 + \lambda \delta_{jk}). \quad (3.36)$$

If χ_{mle}^2 still does not decrease with updated \mathbf{v} , \mathbf{v} will be recalculated using successively amplified λ by a factor of ten until χ_{mle}^2 decreases, upon which the calculation of $\boldsymbol{\alpha}$ should again follow Eq. 3.35 in the next iteration.

Modeling the experimentally measured PSF by a cubic spline

In this section, I work out the explicit expression of \mathbf{p} and its partial derivatives in Eq. 3.35. Essentially, the formulation of \mathbf{p} is nothing more than a model of h_{tot} as

$$p_i = I \cdot h_{tot}(x_i - x_c, y_i - y_c, z_i - z_c) + bg + \text{var}_i / \text{gain}_i^2. \quad (3.37)$$

In the context of 3D SMLM, an analytically modified Gaussian PSF model is typically employed in the estimator to resolve the depth information[71, 75]. To account for an imperfect alignment in the detection path and sample-induced RI mismatch, a realistic PSF comes not only with astigmatism, but also with spherical aberration or even coma. Fitting a severely distorted PSF to a simple astigmatic PSF model will in turn compromise the localization precision and accuracy. In this regard, the fidelity of the PSF model is crucial. To this end, I choose to model the experimentally measured PSF with the cubic spline method [113], which allows for arbitrary combinations of low-order aberrations.

The idea of the cubic spline method is to represent an experimentally measured PSF by a piecewise function, each piece of which describes a continuous intensity distribution within a voxel with up to third-order polynomials,

$$\begin{aligned}
 f_{j,k,l}^{\text{det}}(\tilde{x}, \tilde{y}, \tilde{z}) &= \sum_{m=0, n=0, o=0}^{3,3,3} c_{j,k,l,m,n,o} \tilde{x}^m \tilde{y}^n \tilde{z}^o, \\
 f_j^{\text{exc}}(\tilde{z}) &= \sum_{o=0}^3 b_{j,o} \tilde{z}^o (0 \leq \tilde{x}, \tilde{y}, \tilde{z} < 1),
 \end{aligned} \tag{3.38}$$

where j, k, l indicate the three dimensional indices of the calibrated voxel and $\tilde{x}, \tilde{y}, \tilde{z}$ denote the local coordinates within a voxel. Since we cannot assure an unchanged h_{tot} over long times due to subtle misalignment after the fine alignment and potential misalignment during the measurement, we calibrate the detection and excitation PSF separately. The underlying reason to do so will be discussed later. Two data points with $1/3$ spacing are inserted in each direction within a $97 \times 97 \times 10 \text{ nm}^3$ voxel of the calibrated detection PSF by spline interpolation and also in the excitation PSF. The same number of spline coefficients are in turn calculated from the supporting data points for each voxel. More specifically, 64 coefficients are calculated for each detection PSF voxel and 4 coefficients are calculated in each space for the one-dimensional excitation PSF. The main nodes of the grid, *i.e.*, the raw data points, are labelled with the coefficients $m, n, o = 0$.

In order to justify the validity of the spline interpolation, I tested it on the simulated PSF data used in the segmentation section. The high-resolution PSF data with $5 \times 5 \times 5 \text{ nm}^3$ voxel size are now regarded as the continuous ground truth. The discrete ground-truth PSF is created by sampling the continuous ground truth every $l \text{ nm}$. Of the discrete PSF, one pixel out of every three pixels is selected to generate a control group. The simulation to experimentally measured data is obtained by binning the continuous ground truth with $3l \times 3l \text{ nm}^2$ bin size, which is actually the camera pixel size. Both discrete images are then up-sampled using the cubic spline interpolation method and subtracted from the discrete ground truth to get the mean error of counts. The retrieval precision is investigated by varying the camera pixel size from 50 nm to 200 nm . Although the binning method features a little bit higher mean error compared to the sampling method, the cubic spline exhibits a superior retrieval precision for pixel size $< 150 \text{ nm}$ as shown in Fig. 3.24c, validating the exchange of Eq. 3.28 by Eq. 3.29. When the pixel size is above 150 nm , mean error and variance lose stability for both methods, implying any attempt to bin our $97 \times 97 \text{ nm}^2$ pixel will compromise the fidelity of the PSF model.

Having verified the retrieval precision of spline interpolation, one can establish the piecewise representation of the Poissonian parameter p_i for the i^{th} voxel in the raw data by substituting Eq. 3.38 for h_{tot} in Eq. 3.37,

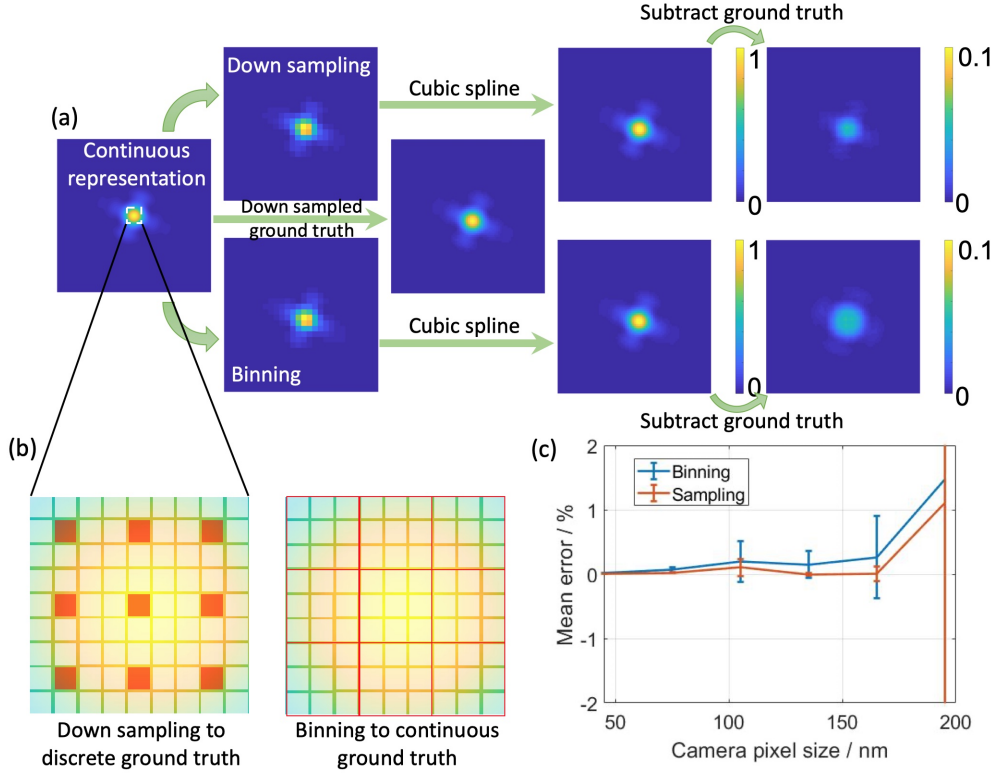


Figure 3.24: Justification of the cubic spline interpolation. (a) The pipeline shows how the cubic spline retrieval residual is calculated. (b) Zoomed-in views of the down-sampling and binning processes to the continuous ground-truth PSF. The fine grid space is l nm and the camera pixel array represented by the thick lined grid has $3l$ nm space. (c) Retrieval mean errors of the binned and down-sampled images to camera pixel size.

$$\begin{aligned}
 p_i = & I \cdot \sum_{m,n,o=0}^{3,3,3} c_{j,k,l,m,n,o} \left(\frac{x_i - x_c - j \cdot a}{a} \right)^m \left(\frac{y_i - y_c - k \cdot a}{a} \right)^n \left(\frac{z_i - z_c - l \cdot u}{u} \right)^o \\
 & \sum_{o=0}^3 b_{j,o} \left(\frac{z_i - z_c - \bar{z} - j \cdot u}{u} \right)^o + bg + \text{var}_i / \text{gain}_i^2.
 \end{aligned} \tag{3.39}$$

The first summation presents h_{det} and the second h_{exc} , in which u is the light sheet step size and \bar{z} is the total misalignment between the light sheet and detection focal plane. In both summations, indices j, k, l are chosen to guarantee fractional values between zero and one in parenthesis. In reality, \mathbf{r}_i represents the coordinate of the concerned voxel within the segment, and j, k, l are indices of the voxel on the calibrated detection PSF, to which the measured voxel \mathbf{r}_i is mapped. It is trivial to calculate the partial derivatives of p_i with respect to \mathbf{r}_c, I, bg and is therefore

not elaborated here. As for now, all mathematical formulation is established, which allows moving forward with the fitting of the parameter set \mathbf{v} .

Establishment of fitting routine

Two metrics are established to evaluate the performance of the global fitting algorithm. The resolution-related metric is localization precision, which is defined as the standard deviation of the cloud of localizations to the same emitter. A high localization precision implies that more details can be resolved in the reconstructed super-resolution image. Localization accuracy refers to the root-mean-square error (RMSE) of the localizations compared to the ground truth of the same emitter. It is introduced to assess whether the estimator is biased, as shown in Fig. 3.20.

The preliminary fit results to the simulated data show a high axial localization precision with a 270 nm localization bias (Fig. 3.25a) if \bar{z} is set to zero while the total misalignment is 300 nm. This indicates that a priori knowledge about the total misalignment must be generated before the measurement, which is almost impossible. The reason for that is the limited precision of the fine alignment procedure with a dye solution. A different way to calibrate the light sheet position is by focusing on a single emitter in a real sample and scanning the light sheet across the emitter. This procedure has to be done on-site to avoid a RI mismatch-induced focal position change. Although a sub-100-nm alignment precision can be achieved by this approach, it is not advisable for the sake of evolutionary misalignment during the course of measurement. To address this difficulty in an economic and adaptive manner, I incorporate \bar{z} as a sixth parameter in the estimator simply by regarding \bar{z} as an independent variable and treating it equal to the other five parameters in the fit.

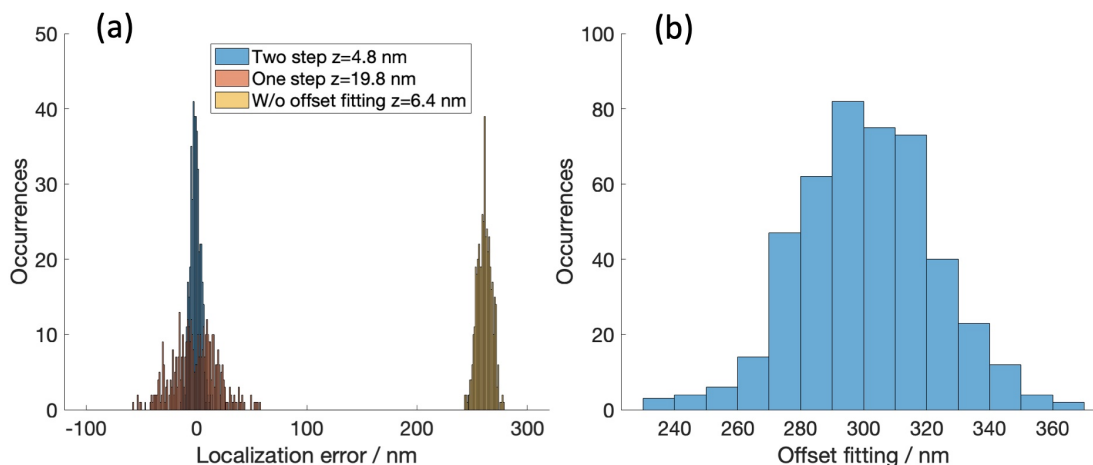


Figure 3.25: Statistics of fitting results with different workflows. (a) Localization error in z direction. (b) Light sheet offset fitting result. Values in the legend represent localization precision.

From the result in Fig. 3.25a, one can see that six-parameter fitting compensates for the bias, however, the localization precision in the axial direction is compromised. This is mainly because z_c and \bar{z} actually co-vary in h_{tot} so that the two parameters share the same search space and loosely compete with each other. Nevertheless, the mean offset in the statistics faithfully reflects the 300 nm misalignment (Fig. 3.25b). As it is a global characteristic of the light sheet that all emitters share the same \bar{z} , the issue of low axial localization precision can be overcome by introducing the averaged \bar{z} obtained in the six-parameter fit in the first round as a constant parameter in a second round of five-parameter fit. The two-step fit exhibits an unbiased axial localization and the highest axial localization precision. The left-shifted peak of the statistics of the likelihood function χ^2 in Fig. 3.26a double validates the necessity of \bar{z} fitting. Similar statistics shown in Fig. 3.26b indicate lateral localization precision is insensitive to fit strategies. Notably, in experiments, because of either the local RI change or mechanical relaxing, the misalignment is no longer a globally constant parameter, but instead spatially and temporally varying. The fitting workflow for experimental data will be discussed shortly.

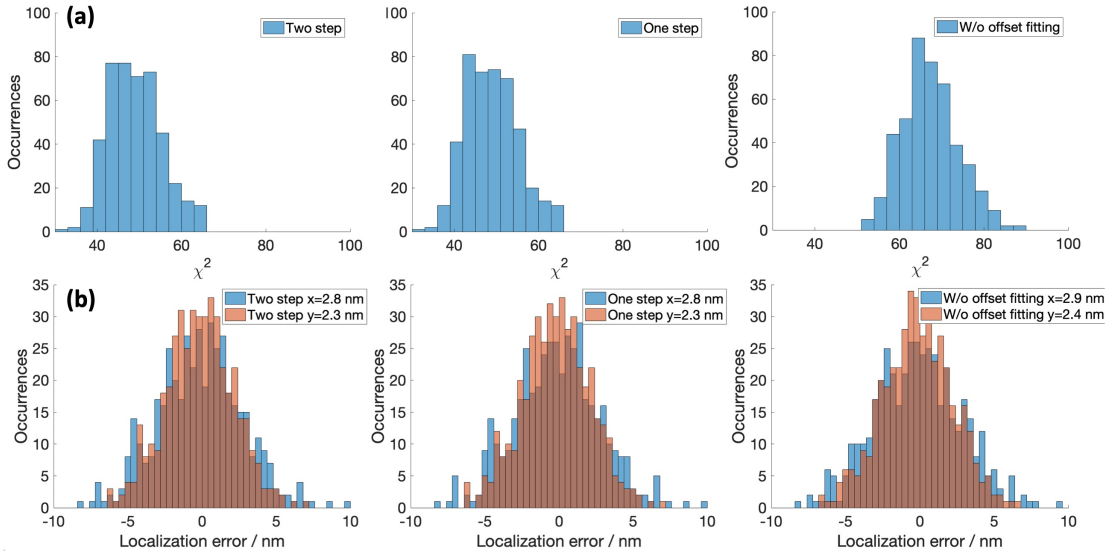


Figure 3.26: Comparison of the localization performance for different fit routines. (a) Statistics of the log-likelihood functions. (b) Statistics of localization error in the lateral direction. Values in the legend represent localization precision.

Theoretical estimation of the fitting error

The Cramér Rao lower bound (CRLB) is a common metric employed to evaluate the minimal achievable variance for an unbiased estimator[114]. It is given as the

diagonal elements of the reciprocal of the Fisher information matrix

$$\text{var}(\hat{\mathbf{v}}) \geq I(\mathbf{v})^{-1}. \quad (3.40)$$

Indeed, the Fisher information matrix measures the variance of the score, which is the gradient of the log-likelihood function with respect to the parameters to be estimated. This relationship can be intuitively understood that, the steeper the score is, the parameters minimizing the log-likelihood function are more likely to be closer to their real values, and the greater the variance of the score is. By the definition of the Fisher matrix, the matrix elements can be readily calculated as the expectation values of the partial derivatives of the log-likelihood function,

$$I_{j,k}(\mathbf{v}) = E \left(\frac{\partial \ln \mathcal{L}}{\partial v_j} \frac{\partial \ln \mathcal{L}}{\partial v_k} \right), \quad (3.41)$$

where $\ln \mathcal{L}$ is the normalized log-likelihood function χ_{mle}^2 . Substituting Eq. 3.32 into Eq. 3.41 gives

$$I_{j,k}(\mathbf{v}) = 4 \sum_i \left[\frac{1}{p_i} \frac{\partial p_i}{\partial v_j} \frac{\partial p_i}{\partial v_k} \right]. \quad (3.42)$$

The fitting routine is implemented on the graphics processing unit (GPU) to process each segment's fitting task in parallel with an independent thread. The full frame gain, variance and offset maps are copied to the global memory so that the launched kernels can freely access them according to the relative position of the individual segment with respect to the full frame. In addition to the fitting parameter $\hat{\mathbf{v}}$, the corresponding CRLBs are also returned together with convergency traces of the log-likelihood function χ_{mle}^2 , whose final values undergo thresholding as a criterion to reject false positive emitters.

3.5.4 Simulation results of global fitting algorithm

Among the acquisition parameters that influence the localization performance, the number of photons dominates the localization precision as discussed in section 2.2.4. I reuse the data generated for the evaluation of the segmentation specificity and sensitivity to characterize the influence of the number of photons on localization precision. The light sheet step size is fixed to 400 nm, allowing for fast acquisition over a large FOV depth. The hexagonal lattice with $NA_{\text{eff}} = 0.4$ and 300 nm misalignment is employed, thus I can validate the performance of the two-step fitting routine in retrieving the offset and correcting the localization bias. The number of slices per segment is another investigated parameter,

which poses a crucial impact on the axial localization precision, as more slices conceivably increase the depth information in the segment and thus can improve the localization performance, which on the other hand will not infinitely gain with increasing number of slices for finite PSF size.

From the simulation results shown in Fig. 3.27, one can first learn that the inverse relationship between localization precision and the number of photons holds for all curves, which all asymptotically converge to zero for a high number of photons. Considerable enhancement of the axial localization precision is observed when the number of slices increases from one to three, particularly in the regime where the number of photons is less than 1000, which is a favorable choice for the low photon count case. Typically, the localization precision improves from 73 nm to 15 nm with 3 slices per segment at the benchmark number of photons. The overlapping localization precision curves in z (Fig. 3.27b) when the number of slices per segment is beyond 2 indicate that the first slice at the top and the fifth slice at the bottom of the segment do not contribute significant information to the estimator. This conclusion can also be supported by the fact that the FWHM of the axial PSF_{tot} is smaller than 800 nm. The lateral localization precision does not significantly benefit from the increased number of slices, implying the lateral position information within 11×11 pixels of one slice already suffices to give a high localization precision.

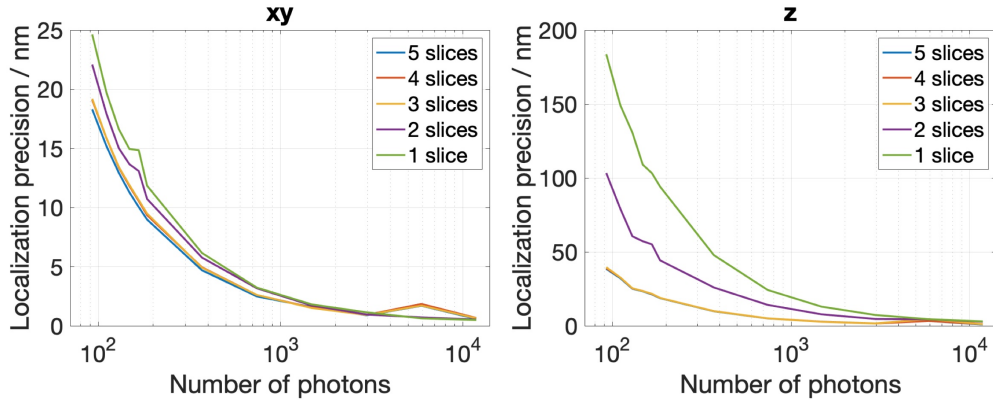


Figure 3.27: Evaluation of localization precision.

The curves in Fig. 3.28 show a good estimation of offset with more than one slice regardless of the number of photons. This result is expected, as the algorithm cannot distinguish the modulation of the detection PSFs of intensity I and the excitation light sheet, provided only one cross-section of the overall PSF is given in the segment. Remarkably, the totally biased estimation of offset for one slice fitting does not affect localization accuracy, which is understandable as only a single lateral image of the emitter is compared against the overall PSF, whose axial variance will not make any difference to the fitting result. One cannot conclude

that one slice fitting is as good as multiple slice global fitting, nevertheless, for the sake of poor localization precision of one slice fitting.

Another conclusion one can draw from the simulation results is the number of slices should preferably be an odd number. The segmentation mechanism is to find the local maximum, the neighboring slices included since they are considered a reasonable segment. Normally the same number of slices flanking the center slice are included in the segment for symmetry. If a segment has an even number of slices, the slice above the brightest slice will be selected in my convention. Yet, because of misalignment, the overall PSF in z direction might not be a perfect monotonic function. Therefore, more supporting data points spanning the entire overall PSF are required to guarantee the convergence of the likelihood function to a global minimum. However, if the supporting data points are skewed to one side of the overall PSF, as they are for a segment with an even number of slices, the likelihood function might end up in a local minimum, leading to a biased localization performance, as shown in Fig. 3.28. In summary, three slices per segment are optimal for achieving the best localization performance with the configured acquisition parameters.

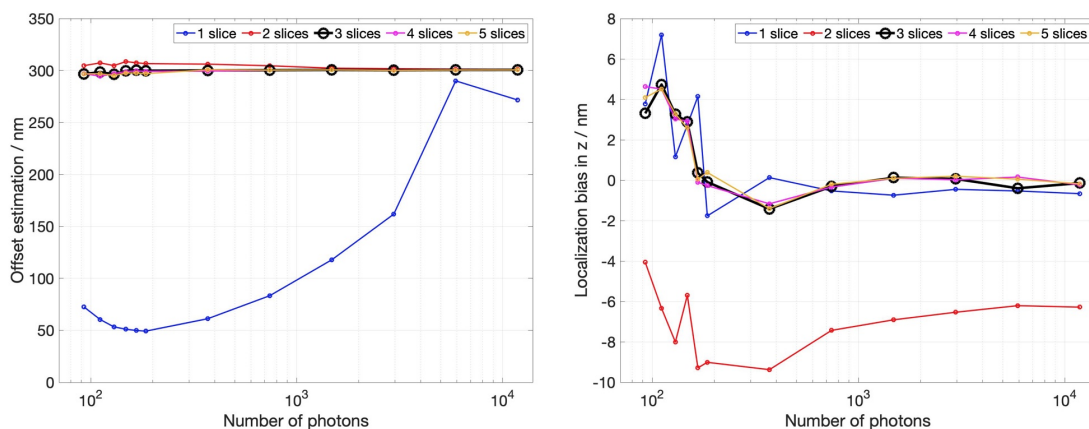


Figure 3.28: Evaluation of light sheet offset estimation and localization accuracy.

Each of the above data points was calculated from the statistics of more than 1,500 localizations and their ground truth. The individual emitter is localized only once with the camera calibration maps and random z position with respect to the light sheet. The localization performance evaluated from such data is of statistical significance, as almost all possible emitter-camera instances are included. However, according to the definition of the CRLB, a rigorous localization precision comparable to the CRLB should be calculated from multiple observations of the same emitter. To this end, I again generated 41 emitters at the same lateral position but different axial positions with 10 nm step size, ranging from -200 nm to 200 nm with respect to the center slice in a segment (Fig. 3.29). Each emitter

with the benchmark number of photons is observed 400 times with the same Poissonian shot noise model and camera read-out noise model. Three slices in each segment were globally fitted, following the conclusion of the previous section.

It can be seen from Fig. 3.29 that the localization precision can achieve the CRLB-predicted minimal error. Throughout the whole imaging depth, both lateral and axial localization precisions remain within narrow bounds. The relatively low axial localization precision at zero is due to the fact that the astigmatism aberration exhibits least spatial variance in the vicinity of the focal plane. In the scenario of SMLM with 400 nm step size light sheet excitation, an emitter found at an arbitrary position within the full FOV can be mapped into the illustrated region in Fig. 3.29. Therefore, one can conclude that the proposed global localization algorithm can achieve a full FOV localization precision of 10 nm in the lateral and 20 nm in the axial dimension with 185 photon counts per emitter.

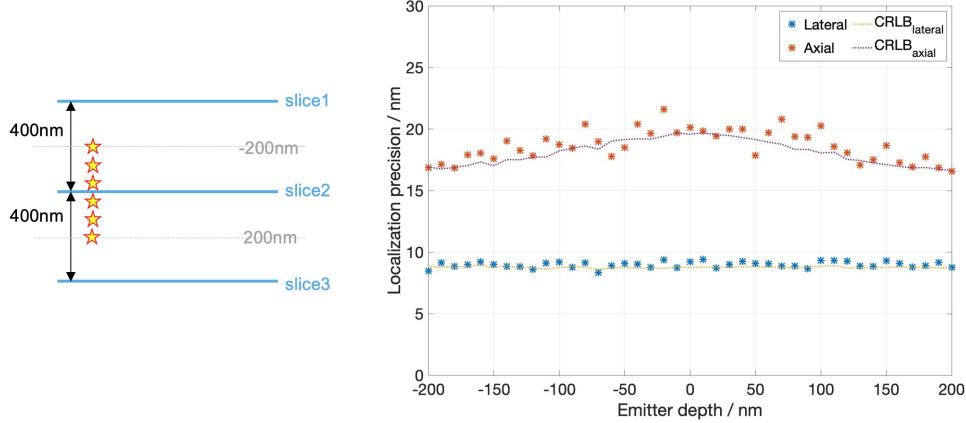


Figure 3.29: The Cramér–Rao lower bound can be achieved within the whole imaging range. Each data point is the average of 400 localizations at depth with 10 nm step size in z .

3.6 Software implementation

3.6.1 Post-processing features for SPIM data

A graphic user interface (GUI) integrating the diverse post-processing features has been developed using Matlab[®] to facilitate the analysis of the data produced with the SPIM modality.

The GUI (Fig. 3.30) provides 3D data browsing features, allowing users to select an ROI for further post-processing such as image binning, camera offset subtraction, gain correction, 3D Richardson-Lucy deconvolution [115], wavelet-based background and noise subtraction (WBNS) [116] as well as image registration including multichannel registration and transformation from laboratory coordinates

to biological coordinates. The processed data can be individually visualized in up to four sub-panels within the GUI to permit comparison of processed data using different methods. Once a data processing pipeline is determined, users can sequentially perform the desired processing methods to establish a recipe for batch mode, which works in parallel to time-lapse acquisition so that data processing will be completed shortly after the acquisition is finished. The cross-correlation based drift correction method described in section 3.4.1 was implemented in batch mode.

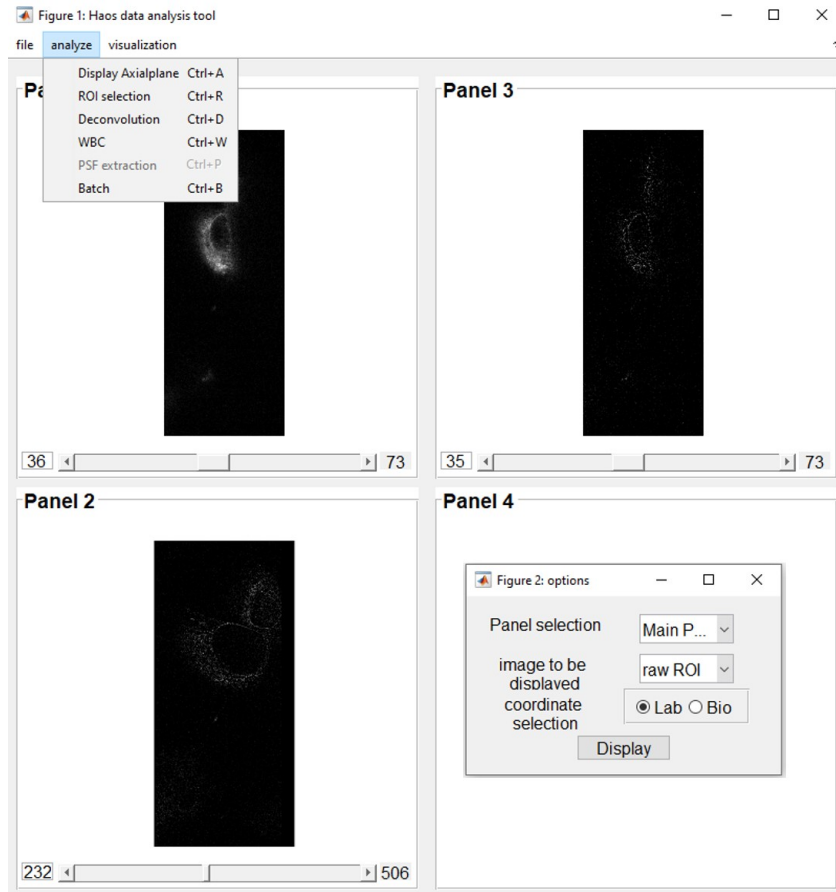


Figure 3.30: A snapshot of the data processing GUI working on SPIM generated data.

3.6.2 Segmentation features for SMLM data

In addition to the widefield data processing modality, the GUI also features segmentation functions for either SMLM or PSF calibration. The segmentation routine used for SMLM data differs from the version for fluorescence bead PSF cali-

bration only in visualization features while the segmentation kernel described in section 3.5.2 is generalized for detecting any PSF-like object regardless of its SNR.

For the calibration of the PSF used in deconvolution, the software labels all segmented PSFs on maximum intensity projections (MIP) of the image stack visualized in panel 1 with their FWHM measures listed in panel 3. The user can manually rule out outliers and display the FWHM profiles of the averaged PSF in panel 2 (Fig. 3.31a).

In the SMLM modality, a constant photobleaching speed factor adapted to specific experiment conditions such as excitation power density, the type of fiducial markers, and imaging buffer, is needed for segmenting fiducial markers in long-time measurement to compensate for the photobleaching-induced decreasing specificity with the dynamically adjusted threshold for each hyperstack in fast mode. Stacks contained in one hyperstack are thought to share the same threshold and are segmented in parallel using all cores of the CPU. The segmented single molecules / fiducial markers are labeled in the MIP of the corresponding stack shown in panel 1 (Fig. 3.31b). One can freely browse through all MIPs in panel 1 and inspect the z positions of the segments in panel 4 to evaluate segmentation performance and adjust parameters if necessary.

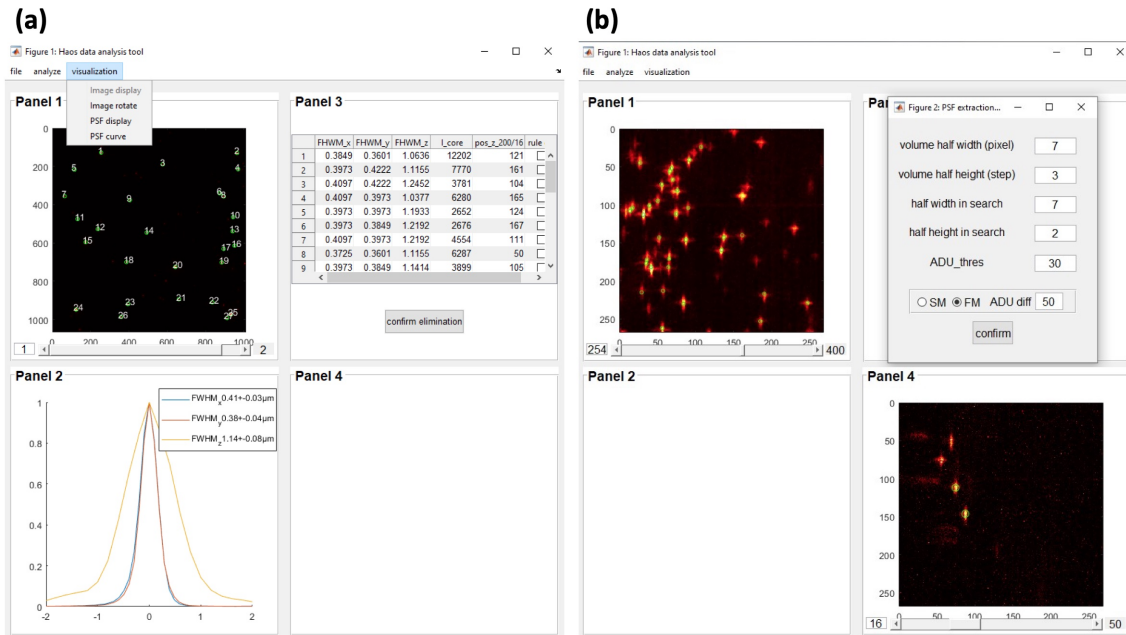


Figure 3.31: Instances of visualized segmentation of integrated data processing GUI. (a) Visualization of PSF calibration. (b) Visualization of fiducial marker segmentation.

3.6.3 GPU accelerated fitter

The data of segmented fiducial markers and single molecules are structured in user-specified subvolumes, normally $11 \times 11 \times 5$ voxels for fiducial markers and $11 \times 11 \times 3$ for single molecules together with their spatial-temporal coordinates (x , y , z and t) with respect to the raw hyperstacks, where t represents the volume index in time when the emitter occurred. Accompanying those data are the camera calibration maps and spline coefficients of PSFs prepared for fitting.

Fitting workflows for fiducial markers and single molecules are separately specified as illustrated in Fig. 3.32. Trajectories for fiducial markers are tracked, of which only the length equal to the total number of volumes is accepted for subsequent fitting, permitting fiducial marker-based drift correction at any given time. Then, all data are copied to the shared global memory of the GPU, where depending on the capacity of the specific device thousands of kernels are launched for fitting. Each thread independently undertakes the entire fitting task for one emitter. According to the emitter index, the specific segments of the data and camera calibration maps in the shared memory are accessed and the fitting results are asynchronously returned to the corresponding segment of the pre-allocated global memory. Six parameters (see section 3.5.3) including light sheet offset are fitted simultaneously for the first fitting round.

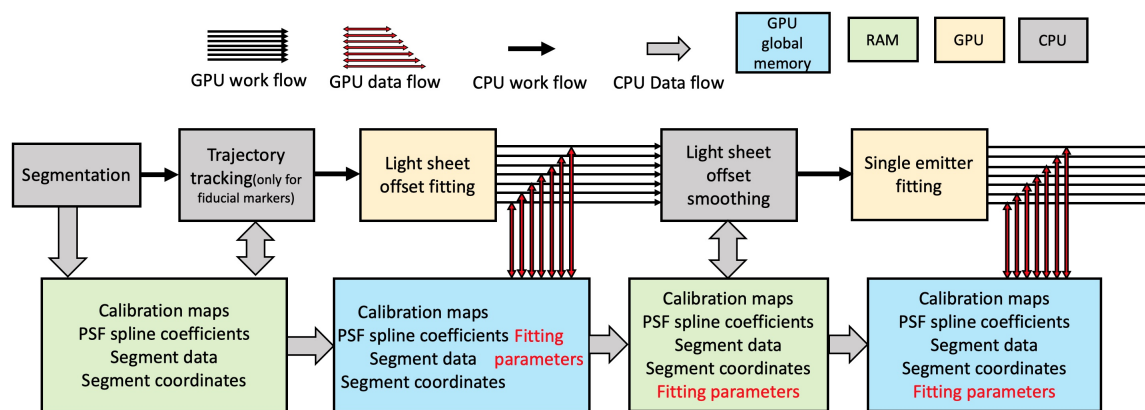


Figure 3.32: Workflow of the fitter.

When all emitters have been fitted, the light sheet offset time trace for fiducial markers or the map for single molecules will be calculated. As shown in Fig. 3.25b, only the average of the offset fit statistic gives the unbiased light sheet offset estimation. I approach the light sheet offset time trace by applying a smooth sliding window to the raw data (Fig. 3.33). The smoothed light sheet offset array is then copied back to the GPU memory and used as a constant parameter for the second round of fitting.

Because the single molecules are largely distributed all over the acquisition ROI, it is possible to work out the light sheet offset map as a function of time with

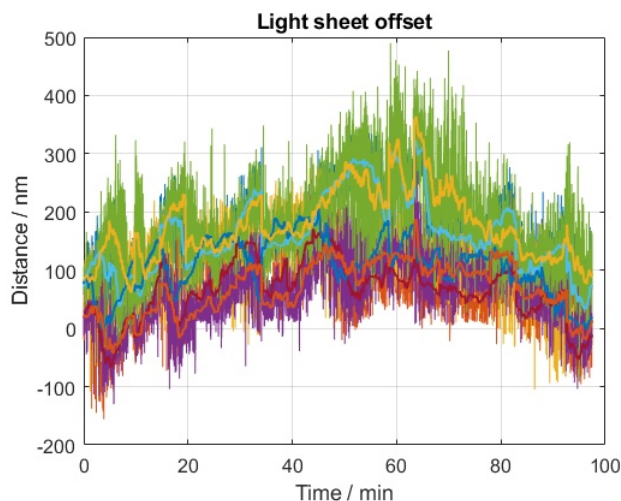


Figure 3.33: Light sheet offset fitting results for fiducial markers. Five fiducial marker traces are plotted with thin lines for raw data and bold lines for smoothed data.

the offset fitting results of single molecules. To make the 2D+t map statistically meaningful, offsets of the fiducial markers located within the 10×10 binned pixel (Fig. 3.34a) at the same time are grouped followed by sliding window smoothing on the time axis. Three smoothed light sheet offset traces for the selected regions are shown in Fig. 3.34b. In the next round of fitting, light sheet offsets are designated to single molecules as constant fitting parameters according to their spatial-temporal coordinates. Single molecules and fiducial markers are excited by different wavelength light sheets, which are not perfectly overlapping even after meticulous alignment, as can be seen from the discrepancies between offset time traces of two channels at different regions.

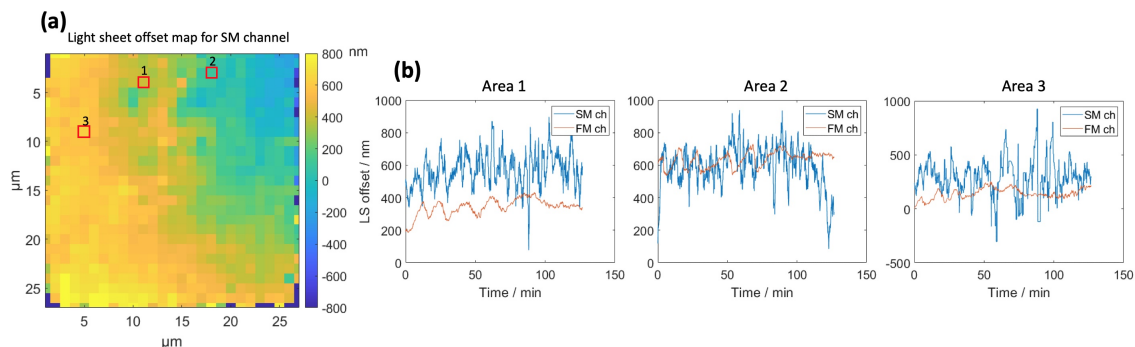


Figure 3.34: Light sheet offset fitting results for single molecules. (a) Light sheet offset map at a certain time. (b) Light sheet offset time traces of selected regions.

3.7 Sample preparation

3.7.1 Sample insert

The sample insert, which fits into the open window on the bottom plate of the environmental chamber, serves as a holder of the coverslips and thus permits fast sample swapping during the course of the measurement. It consists of an austenitic stainless steel base plate with a square open window and top frame used to clamp the coverslip against the base plate with the aid of an array of magnets embedded into the rims of both parts, as shown in Fig. 3.34. The rectangular thin frame in-between the coverslips and the top frame is made of Polydimethylsiloxane, also termed PDMS (SYLGARD™ 182 Silicone Elastomer, Dow®), which is an inert and biocompatible silicone material [117] and widely used in the fabrication of microfluidic and lab-on-a-chip devices. We mix 1 part curing agent in 17 parts silicone elastomer base by weight and put the mixture in a vacuum chamber for 10 min to remove the bubbles. The mixture is then poured into a mold and cured for 30 min at 150 °C. Right before the measurement, a coverslip with cells is sandwiched between the permanently glued coverslip (window in Fig. 3.34) and the PDMS sealing frame.

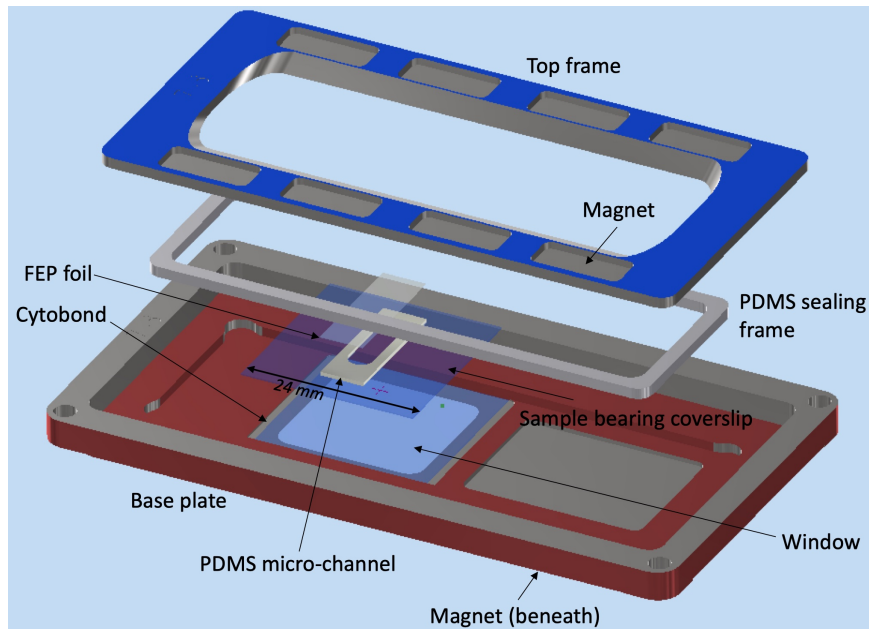


Figure 3.35: Model of the sample insert.

To verify the bio-compatibility of the coverslip sealant (2020-00-1, Cytobond® manufactured by SciGene), we cultured cells in a Cytobond coated well for 48 h. No significant morphological discrepancy was observed when compared with the control group. Upon installation, 5 mL of imaging medium is added to the

sample insert. The total time cells are exposed to air should not be longer than 15 s. The glass window is intended for browsing the entire area of the coverslip using a low magnification epi objective lens so as to identify cells of interest. However, for some special purposes, where a high NA oil immersion objective lens with a short working distance has to be used, the coverslip with a monolayer of cells also serves as a window in lieu of a permanently glued coverslip.

3.7.2 Coverslip pre-treating

To clean 24×24 mm² coverslips (8000105, Hirschmann Inc.) for future use, a plasma cleaner (PDC-002, Harrick Plasma Inc.) is employed with processing gas of oxygen to remove organic dirt particles from coverslips surface through ablation and a chemical etching effect. The complete coverslip pre-treating protocol is as follows:

- Plasma clean coverslips for 30 min.
- Immerse coverslips in Hellmanex[®] II (320.002, Hellma[®]) solution overnight (1 part Hellmanex in 70 parts Milli-Q[®] water). For simplicity, all water in the following text refers to Milli-Q[®] water if not otherwise stated.
- Thoroughly rinse coverslips in water and preserve them in water. Before using, dry the coverslip in air flow hood and put it in the standard six-well plate (657160, Greiner CELLSTAR[®]).
- (Optional) Normally, cells will fully attach and stretch out on cleaned coverslips 24 h after seeding. To boost the attachment process, fibronectin from bovine plasma (F1141, Sigma-Aldrich[®]) can be used to coat the coverslip surface. Dilute 1 mg/mL fibronectin stock solution by a factor of 2 in water. Drop 30 μ L diluted solution on a coverslip and leave it drying out to get 1-5 μ g/cm² protein-coated surface, on which cells attach in 2 h.

An alternative coverslip washing protocol is listed below, which is specifically used for SMLM near the coverslip surface, where autofluorescence from contaminants should be eliminated:

- Sonicate coverslips in 2% Alconox[®] (1104-1, Cole-Parmer[®]) solution in water for 15 min.
- Sonicate coverslips in water for 10 min.
- Rinse coverslips in water.
- Sonicate coverslips in 2M potassium hydroxide for 30 min.

- Rinse coverslips in water.
- Sonicate coverslips in water for 10 min.
- Preserve coverslips in 70-80% ethanol.

3.7.3 Dye sample in PDMS microchannel

A dye sample is necessary for fine alignment of the excitation light with respect to the focal plane of the detection objective lens. For the sake of quantity and protecting the objective lenses from contamination, the dye solution is encapsulated in a PDMS micro-channel. As shown in Fig. 3.35, the micro-channel measures 0.5 mm depth, 3.5 mm width and 13.6 mm length and thus features around 17 μL capacity. In order to align all available laser lines, we use a dye mixture composed of Atto 395, Atto 488, Atto 547 and Atto 642 solution in DPBS (+/+) solution. Each dye is fully dissolved in dimethyl sulfoxide to make a stock solution of 10 mM followed by further dilution in DPBS (+/+) to 10 μM . Lastly, 17 μL of the dye solution is injected into the PDMS micro-channel stuck on a plasma-cleaned coverslip, and a thin layer of silicone oil is applied to the top edge of the micro-channel. The final and most crucial procedure is to cover the channel using a strip of 10 μm ultra-thin fluorinated ethylene propylene foil kindly provided by the TCI company. Either introducing bubbles inside the channel or smearing the fluorinated ethylene propylene foil with glue will spoil the sample. Precautions such as always immersing the dye sample in water and keeping it in the dark, preferably at 4 $^{\circ}\text{C}$ when not using it, must be taken to avoid deterioration.

3.7.4 Fixed beads sample

For the purpose of PSF calibration and spherical aberration correction, 100-nm diameter polystyrene yellow-green microspheres (F8803, InvitrogenTM) and red microspheres (F8801, InvitrogenTM) are employed. Two kinds of fixed beads samples are used in my experiment. Firstly, beads fixed on the surface of a coverslip are reusable, but the coating density is hard to control even when prepared with the spin coating method. Multiple ROIs have to be carefully selected to gather significant statistics of single beads. Secondly, beads can be prepared in an agarose gel to create a volumetric sample. Regarding the first approach, a desired bead density of 1 bead / μm^2 on a $24 \times 24 \text{ mm}^2$ coverslip requires 5.76×10^8 beads. The number of microspheres per mL C_N in the stock solution is given by

$$C_N = \frac{6C \times 10^{12}}{\rho \times \pi \times \phi^3}, \quad (3.43)$$

where ϕ is the diameter of the microsphere in μm , ρ is density of the polymer in g/mL (1.05 for polystyrene) and C represents the concentration of suspended beads in g/mL (0.02 g/mL for a 2% suspension). For our 2% (in weight), 100-nm polystyrene beads, 0.016 μL stock solution is needed to coat one coverslip fully. The detailed sample preparation protocol is as follows:

- Sonicate beads stock solution for 10 min to guarantee monodisperse stock.
- Sequentially dilute beads stock in water by a factor of 200 followed by 10 times to get 1 to 2k times diluted beads solution.
- Drop 30 μL diluted beads solution on the hydrophilic surface of coverslip treated by 10 min plasma cleaning.
- Leave beads loaded coverslip in the dark and keep the surface level so that beads solution will evenly spread over the whole coverslip. The sample will be ready for use upon water drying out. The coated beads on the coverslip surface last even longer than the coverslip itself under weathering.

The second approach, namely to fix beads in polymerized agarose gel, can be used to create a volumetrically homogeneous dispersion, thus allowing for more than 200 single beads in $25 \times 25 \times 20 \mu\text{m}^3$ ROI in comparison to just a couple of available single beads fixed on a coverslip surface. The RI mismatch between agarose gel and the immersion medium induces aberrations and can be overcome by preparing a gradient of concentrations of NaCl saline solution and looking for the concentration at which the RI matches that of agarose gel best (with the aid of a portable refractometer, PAL-RI, ATAGO®). For the calibration of the PSF, the sample will be immersed in NaCl solution to minimize aberration.

- Prepare agarose solution by heating agarose colloid produced by 1 part powder (A6560, Sigma-Aldrich®) and 100 parts water (w/w) at 70 °C for 30 min.
- Dilute sonicated beads stock solution in water about 30 times followed by 100 times dilution in agarose solution to obtain a 20 pM beads agarose solution.
- Thoroughly vortex the beads solution at high speed for 15 s before applying it to the PDMS micro-channel stuck to the coverslip.
- Inject the beads solution into the micro-channel and flip the coverslip, immersing the micro-channel side in water to avoid evaporation. All operations should be swiftly done as soon as the agarose solution leaves the heating plate since it begins to polymerize when the temperature is lower than 40 °C.

The drawback of this sample is that the agarose is apt to fracture during the measurement because of the disturbance caused by frequent movement of the sample for ROI searching, such that the sample might disintegrate or detach from the micro-channel. Therefore, the beads fixed in agarose gel can only be used a limited number of times.

Apart from PSF calibration, fluorescence polystyrene microspheres serve as fiducial markers in the SMLM modality. Sulfate-modified polystyrene latex beads with 100-nm diameter and red fluorescence (L9902-1ML, Sigma-Aldrich[®]) are used for their highly hydrophobic surfaces and thus high affinity to the proteins on the cell membrane. The fiducial marker coating protocol is as follows:

- Dilute 3 μL fully vortexed stock solution in 300 μL DPBS (+/+) solution.
- Repeat the first step on the beads in DPBS (+/+).
- Dilute 50 μL solution obtained at the second step in 950 μL DPBS (+/+).
- Apply 1000 μL solution to the immunostained fixed cells in 6-well plate.
- Incubate the sample for 30 min. and wash the sample twice for 10 min. with DPBS (+/+).

3.7.5 Imaging buffer

The imaging buffer used for SMLM consists of three components including base buffer (buffer B), thiol group and oxygen scavenging system, specifically GLOX in my work. This protocol shows the recipes of base buffer and GLOX.

- Dissolve 1.51 g Tris, 0.15 g NaCl and 25 g glucose in water to get 250 mL buffer B containing 50 mM Tris, 10 mM NaCl and 10 % (w/v) glucose. Titrate buffer pH to 8 with HCl.
- Dissolve 61 mg Tris and 150 mg NaCl in water to get 50 mL buffer A containing 10 mM Tris and 50 mM NaCl. Titrate buffer pH to 8 with HCl.
- Dissolve 17 mg catalase powder (C40-100MG, ≥ 10000 units/mg protein, Sigma-Aldrich) in 1 mL water to get 17mg/mL catalase solution. Dissolve 280 mg glucose oxidase powder (G2133-250KU, Sigma-Aldrich, Taufkirchen, Germany) in 4 mL buffer A and vortex.
- Blend catalase solution and glucose oxidase solution. Spin down the mixture at 13.4×10^3 RPM for 10 min.
- Aliquot supernatant as GLOX solution. Store GLOX and buffer B at 4 °C.

- Add 50 μL 2- mercaptoethanol (Sigma–Aldrich), 50 μL GLOX into 4.9 mL buffer B right before the measurement. Fully agitate the mixture and inject it into the sample insert. Wait for 30 min before imaging until the reaction equilibrium state is achieved.

The RI of the imaging buffer measures 1.3500 at room temperature. A saline solution with the same RI was prepared as the immersion medium of the dye sample for alignment in the SMLM modality. Indeed, the RI of the immersion medium of the dye sample should always match the specific immersion medium used for the cell sample.

3.7.6 Transfection and staining

When dealing with cell samples, especially for live cell measurements, the health status of cells is crucial. Cells are considered to be healthy for transfection and staining only if the confluency is between 50% and 100% and each individual cell is stretching on the surface of the coverslip. Otherwise, several rounds of routine culture and splitting need to be carried out until cells are ready for special treatments. If that is not the case, thawing new cells preserved in liquid nitrogen is necessary. The protocols for general treatments of cells are listed in the appendix.

For cell transfection, two commercial reagents are employed to deliver the plasmid, namely XfectTM Transfection Reagent (631318, TaKaRa) as well as LipofectamineTM 3000 (L3000015, InvitrogenTM), the latter one is designed in particular for hard-to-transfect cells, therefore, they are more harmful to cells compared to Xfect. In my experiments, Xfect was preferably used. The transfection protocols for both reagents are listed below.

Xfect transfection protocol:

- Thaw Xfect Polymer and reaction buffer at room temperature prior to use. Once thawed, store both of them at 4°C for up to 12 months.
- Thoroughly vortex the Xfect Polymer and reaction buffer for 10-30 s.
- Moderately vortex the plasmid for a few s.
- Add 5 μg plasmid into 100 μL reaction buffer and vortex for 5 s.
- Add 1.5 μL of the Xfect Polymer (always use 0.3 μL Xfect Polymer per 1 μg plasmid) into the eppi containing the plasmid and the reaction buffer followed by 30 s vortexing.
- Incubate the mixture for 10 min at room temperature.

- Evenly apply the above mixture to cells growing on a 24×24 mm² coverslip in one well on a standard 6-well plate (657160, Greiner CELLSTAR[®]) when the cell confluency reaches 70%. Given non-standard wells in which cells are seeded, for instance, customized PDMS wells, the amount of transfection reagent to be applied scales with the surface area.
- Change the medium 4 h after transfection.
- Image cells around 24 h post transfection when the expression efficiency approaches its maximum.

The best moment and the time window to image the cell after transfection depend on the labeling target and the FP tagged to it. An advisable way to determine the proper imaging time is to check the expression status every 12 h after transfection on an ordinary wide-field microscope. Notably, the expression level is not the only metric to evaluate transfection, as protein over-expression can be toxic to cells in several ways and thus possibly hinders cell growth[118]. A typical example is transfection-induced apoptosis despite substantial expression level in the initial post transfection stage. Either over-expression on its own or the vulnerability to the transfection lipid of a particular cell line to be transfected causes damage to cells. Therefore, one has to be cautious regarding establishing a transfection protocol especially for biological studies. It is necessary to transfect cells in an 8-well chamber with a gradient of DNA-lipid complex prepared in step 7 to find out the optimal concentration. Note that the cell generation count can also influence cell status. Thus, experiments should always be carried out with cells not older than 30 generations.

Lipofectamine transfection protocol:

- Label two eppi and add 125 μ L Opti-MEM (reduced serum medium) apiece.
- Dilute 3.75 μ L Lipofectamine 3000 reagent in eppi #1 and vortex 2-3 s.
- Dilute 2.5 μ g plasmid in eppi #2, then add 5 μ L P3000 reagent into the same eppi. Gently pipette the solution up and down to mix well. Always use 2 μ L P3000 reagent for every 1 μ g plasmid and 25 μ L Opti-MEM (A4124802, GibcoTM) for every 1 μ L P3000 reagent.
- Add the entire fluid in eppi #2 into eppi #1. The Opti-MEM volumes in two eppi should always be same.
- Incubate eppi #1 at room temperature for 10-15 min.
- The same as steps 7-9 in Xfect protocol except substituting DNA-lipid complex formed using Lipofectamine for that with Xfect.

Although transiently transfected or stably expressing FPs are more biocompatible and reliable for live cells [119] in comparison to staining with dyes, the latter one is still used in my experiment for fast labeling. In this thesis, I use CellMaskTM Deep Red plasma membrane stain (C10046, InvitrogenTM) to label cell membranes and Hoechst 33342 (H3570, InvitrogenTM) to label cell nuclei. Since dyes used for staining are susceptible to photobleaching [120] and tend to diffuse over time [121], conducting time-lapse measurements for hours with stained live cells is not recommended. The labeling protocol is as follows:

- Dilute 1000× concentrated stock solution about 100 times in 1× DPBS with calcium chloride and magnesium chloride(14040-091, GibcoTM) in an aliquot for future use.
- Prepare 400 μ L 0.5× of the concentrated solution using DPBS (+/+) for one well in standard 6-well chamber plate.
- Aspirate the culture medium out of the well and apply the prepared solution to the cells.
- Incubate cells immersed in staining solution for 5-10 min at 37°C.
- Remove the staining solution and rinse the coverslip with DPBS (+/+) three times.
- Image the cells immediately.

In multi-channel measurements, labeling methods for different channels are mainly up to the imaging modalities and research goals. When two-channel transfection is necessary, available transfection workflows are bi-transfection (simultaneous transfection with two plasmids) and stepwise transfection. Bi-transfection consists of mixing two types of plasmids together, treating them as a whole and preparing the DNA-lipid complex in one solution. Stepwise transfection is to transfect one channel followed by a second time transfection at least 6 h later. The expression windows and transfection difficulty decide the final chosen transfection protocol.

3.7.7 Cell fixation and immunolabeling

Proof of principle experiments for my SMLM algorithm were conducted by imaging immunostained microtubules with Alexa Fluor 647 (AF647) in fixed HeLa cells. The sample preparation protocol is as follows:

- Rinse cells in a standard 6-well plate twice with warm DPBS(-/-).

- Prefix and permeabilize cells for 2 min by immersing them in 200 μL cytoskeleton buffer containing 0.3% (v/v) glutaraldehyde (GA) and 0.25% (v/v) Triton X-100. The cytoskeleton buffer is a water solution of multiple components including 10 mM MES pH6.1, 150 mM NaCl, 5 mM EGTA, 5 mM D-glucose, 5 mM MgCl_2 .
- Fix cells in 200 μL 2% (v/v) GA solution in cytoskeleton buffer for 10 min.
- Immerse fixed cells in 200 μL freshly prepared 0.1% (w/v) NaBH_4 solution in DPBS(-/-) for 7 min to quench autofluorescence.
- Wash sample twice for 5 min in DPBS(-/-).
- Dilute mouse anti- α -tubulin primary antibody stock solution by 500 times in DPBS(-/-) containing 2% (w/v) BSA to get approximately 50 nM primary antibody solution.
- Flip the sample upside down in a droplet of primary antibody solution and incubate for 30 min.
- Wash the sample 3 times for 5 min. Dilute secondary antimouse antibody staining with AF647 stock solution by 500 times in DPBS(-/-) containing 2% (w/v) BSA to get approximately 25 nM secondary antibody solution.
- Flip the sample upside down in a droplet of secondary antibody solution and incubate for 1 h.
- Wash the sample 3 times for 5 min and the sample is ready for imaging.

Chapter 4

Applications

4.1 Time-lapse imaging of Wnt signaling

4.1.1 Background of Wnt signaling

Wnt signaling is a process, by which a concentration gradient of Wnt morphogen, known as a family of evolutionarily conserved glycoproteins produced by Wnt secreting cells, regulates stem cells differentiating and tissue patterning during the development of the embryo in a way that the specific target gene expression in the determination of cell fate depends on its surrounding Wnt concentration[122]. Malfunctioning of Wnt signaling will give rise to developmental defects, dysregulation of homeostasis and several types of cancers[122].

There are mainly three stages of Wnt signaling, including Wnt release from the donor cell, Wnt transport in an aqueous extracellular matrix, and activation of signal transduction in the target cell. Upon palmitoylation and glycosylation in the endoplasmic reticulum, the post-transcriptionally modified Wnt proteins bear hydrophobic properties and incline to aggregation, preventing bare Wnt proteins from free diffusing to Wnt-receiving cells in the extracellular matrix[123]. Shielding the hydrophobic structures on Wnt from the aqueous environment is a fundamental measure to facilitate paracrine signaling, regarding which several mechanisms are proposed such as lateral free diffusing with the aid of heparan sulfate proteoglycans, lipoprotein or exosome-mediated dispersing, and trafficking in the form of Wnt-chaperone protein complex[124]. Contrary to those passive transportation channels, cytoneme-mediated active transport is believed to be indispensable in long-range Wnt delivery [125].

Cytoneme refers to a special type of filopodia intended for the intercellular transport of signaling components [126]. The formation of a cytoneme is driven by the planar cell polarity pathway, by which the downstream activation of cytoskeletal regulators will trigger actin polymerization upon binding of Wnt to its coreceptors such as Ror2, Fzd7 and Dvl on the plasma membrane at the Wnt

releasing stage[127]. At the binding site, an extrusion forms and turns into out-growing filopodia approaching Wnt-recipient cells. In addition to transport at the tip of the filopodia, evidence has appeared that cytonemes act as conduits, along which packages of Wnt vesicles are continuously transported [128]. However, whether Wnt vesicles 'surf' on [129] or traffic within the conduit, also known as tunneling nanotube (TNT) [130], remains debated. To answer this question, I conducted in-vivo measurements of cytoneme-mediated Wnt signaling in live cells using the microscope described in the previous chapter.

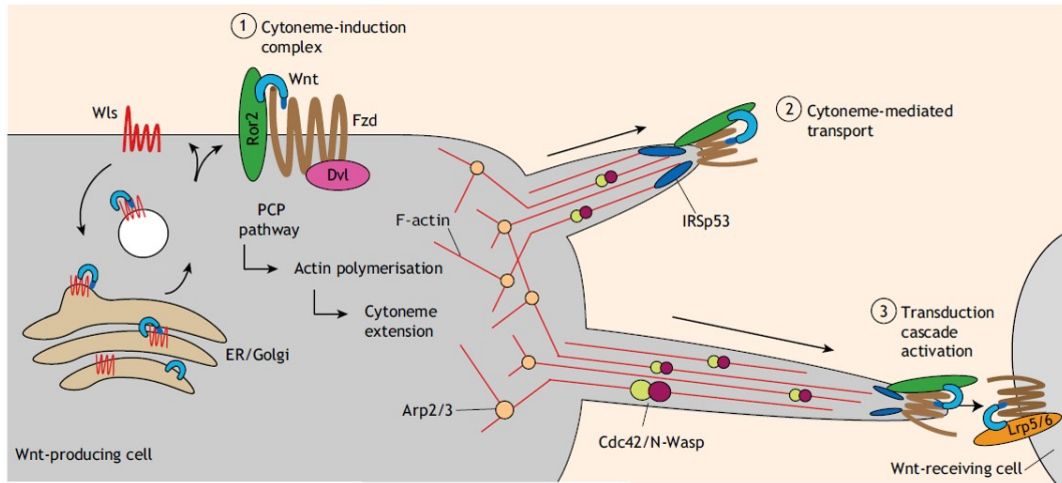


Figure 4.1: Illustration of the role of cytonemes in Wnt signaling. Reprinted with permission from [122], Copyright 2019, the Company of Biologists. Permission conveyed through Copyright Clearance Center, Inc.

4.1.2 Results of Wnt signaling measurement

Double-transfection of H1703 cells with EGFP-Wnt3a and MEM-mCherry plasmids allowed us to separately identify Wnt proteins and cytonemes with a 560 nm longpass dichroic mirror. For the Wnt channel, 473 nm excitation and 527/70 nm bandpass filter were employed, and 561 nm excitation and 617/73 nm bandpass filter for the plasma membrane channel. This configuration resulted in spectral detection efficiency of 76% and 68 % for Wnt and plasma membrane, respectively. An optimized hexagonal lattice light sheet (see section 3.2) for both channels was employed to cover a large FOV, thus adapting the microscope to arbitrary cell arrangements as the low double-transfection efficiency and low occurrence of cytoneme-mediated Wnt transporting event only renders a few cells on a coverslip suitable for our measurement purpose. Since the TNT is prone to rupturing under mechanical stress [130], cells to be measured were cultured and transfected in a commercial removable 4-well chamber (80466, ibidi Inc.) stuck to the coverslip.

Right before the measurement, the removable chamber was gently peeled off to minimize sample migration-induced disturbance.

Normally, we use a combination of 50 ms frame exposure time, 23 W/cm² 473 nm laser power and 64 W/cm² 561 nm laser power to collect sufficient numbers of photons while minimizing the photobleaching effect. According to the Nyquist sampling theorem, since the axial resolution is calibrated as 730 nm, a 400 nm z step size was configured for volumetric scanning. The cells of interest are exposed every 30 s during the course of 2 h. Multi-channel image registration is an indispensable data processing procedure in such a two-channel measurement. Here, I only considered translation, the vector of which was calibrated by cross-correlating images of fluorescence nanoparticles recorded through two cameras with excessively high excitation power such that the bleed-through signal was sufficiently high in the neighboring channel. Depending on the structural characteristics of Wnt and cell membrane, the acquired images went through different post-processing routines. To facilitate further processing, the sub-volume encompassing the most meaningful data was clipped out of the raw data. Camera dark images were subtracted from respective selected ROIs followed by full 3D Lucy-Richardson deconvolution with pre-calibrated PSFs. The WBNS method was applied to the Wnt channel right after deconvolution to get crisper 3D rendering, whereas WBNS would be too harsh and aggressive for cell membrane images featuring background-like low frequency structures. At last, the processed images were laterally 2×2 binned and visualized using appropriate software.

The $x - y$ and $x - z$ MIPs of the rendered volumetric data at three different time points are shown in Fig. 4.2, where the red channel represents the cell membrane and the green channel Wnt. In total, four vesicles transported from the cell in the upper-left corner to the cell in the lower-right corner were observed in 30 min. Zoomed-in view of the cytoneme channel at 10 mins is given in Fig. 4.2d. Two swelling nodes along the cytoneme indicate the existence of vesicles inside the cytoneme. By applying a rotational transformation to the interpolated data with isotropic pixel size, the normal of the $x - y$ plane is transformed to be parallel with respect to the cytoneme axis. Thus, we can readily localize the z positions of two nodes and plot the profiles for the cytoneme and Wnt channels.

The valley in the red cross-section (lower panel in Fig. 4.2f) indicates the hollow structure of the cytoneme, in which the Wnt vesicle was localized (peak in the green cross-section), justifying the scenario that Wnt vesicles are indeed transported inside the TNT. Although the valley of the node corresponding to the first vesicle (upper panel in Fig. 4.2f) was not resolved, the colocalization of red and green peaks support the previous conclusion. The successfully resolved TNT exemplifies the superior performance of our microscope to resolve sub-micron 3D structures.

Measuring the vesicle transport speed inside a TNT is not trivial, as the vesicle velocity appearing in the Wnt channel was influenced by both active transport

and the stretching or contracting motion of the TNT itself. Therefore, each vesicle trajectory has to be manually segmented by comparing it to the TNT channel to rule out sequences when the morphological change of TNT occurs. As with the coordinate transformation method used before, all TNTs with candidate vesicles underwent affine transformation such that TNTs were aligned to z axes. Notably, only straight TNTs were analyzed here to simplify the calculation of velocity. Only a small fraction of the raw data survived the strict screening procedure, as shown in Fig. 4.3. It can be seen that the full 3D+t data measured with SPIM agrees quite well with the 2D+t data measured with a spinning disk confocal microscope.

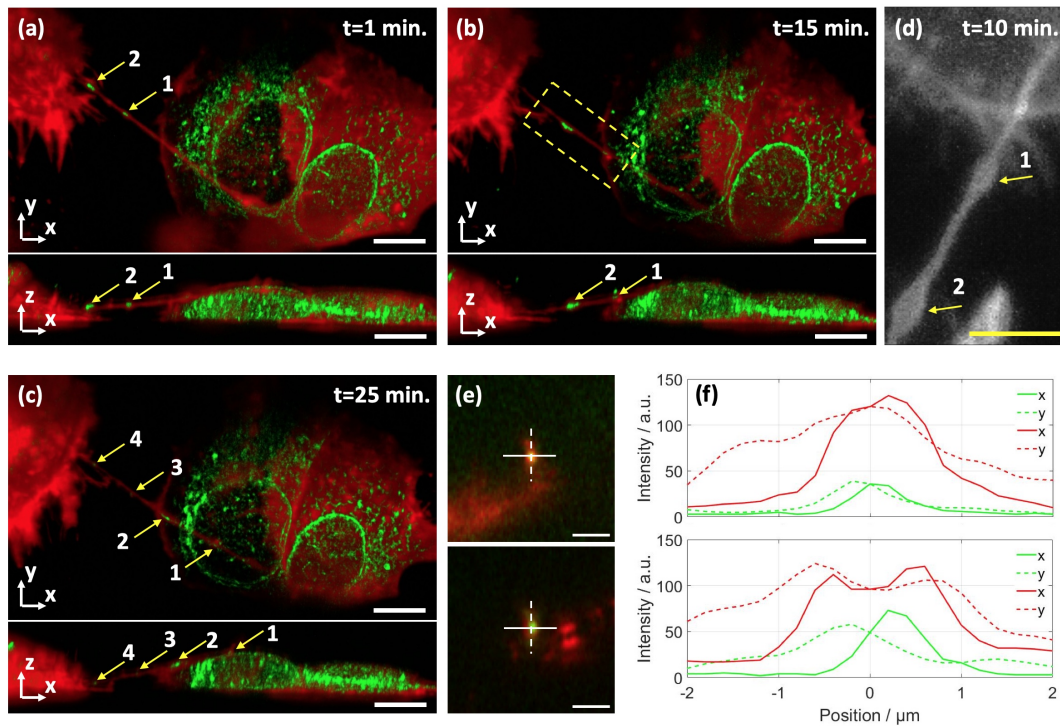


Figure 4.2: Time lapse imaging result of Wnt vesicle transport. (a)-(c) MIPs of two-channel merged volumetric visualizations to Wnt and cell membranes at different time points. The arrows and numbers mark the vesicle position and index. The cell membrane is represented by the red color and Wnt channel is represented by the green color. Scale bar, 10 μm . (d) Zoomed in view of the insert box labeled with the dashed line in (b) for the cell membrane channel. Scale bar, 5 μm . (e) The cross-section of the cytoneme at vesicle 1 (upper) and vesicle 2 (lower). Scale bar, 2 μm . (f) The profiles of cytonemes and vesicles at vesicle 1 position (upper) and vesicle 2 position (lower).

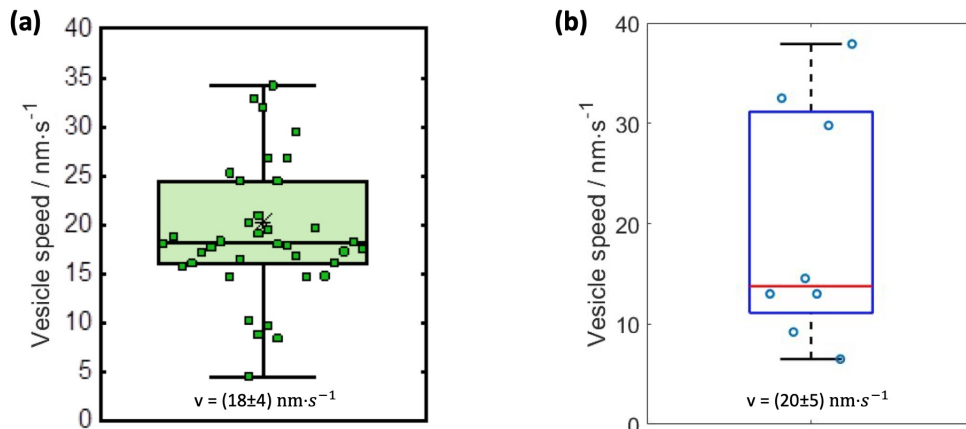


Figure 4.3: Statistics of vesicle transport speed. (a) Data measured with a spinning disk microscope. Adapted from Dr. Eckert’s report. (b) Data measured with SPIM.

4.2 Uptake of surface-modified nanoparticles

4.2.1 Background

Nanoparticles (NPs) are promising carriers of therapeutic agents through encapsulating drugs in the interior of a polymeric shell[131] or dissolving and entrapping drugs in the constituent particle matrix[132]. One possible application in the field of oncology foresees the internalization of drug-carried NPs circulating in the vasculature by the target tumor cells, the biocompatible and biodegradable polymeric material constituting NPs will be reduced to monomer and metabolized, intracellularly releasing the carried cargo to finish drug delivery and administration[133].

However, without any specificity, those nanocarriers are not only taken up by malignant cells but also by normal cells, rendering low targeting efficiency and strong non-specific toxicity [134]. Moreover, exposure to the physiological environment containing active biomolecules gives rise to conformational changes of bare NPs, which, in turn, exhibit altered physicochemical properties[135]. Among a variety of NP-biomolecule interactions, the NP-protein interaction is primarily studied[136, 137].

Nanoparticle protein corona (NP-PC) refers to the complex formed from adsorption of proteins to the NP surface[138]. Upon exposure to blood plasma, thousands of types of proteins start to associate with NPs at different rates. Over time, proteins with weak affinity are replaced by those with strong affinity[139, 140]. NP-PC complexes formed with weak/strong binding affinity proteins are called soft/hard corona. This selective exchange process will be typically established within 30 s, leaving NP-PC complex in stable composition[141].

High stability of the hard corona is favorable for the nanocarrier as the PC protects the NP from further conformational change with molecules present in biological fluids and thus maintains its intended functionality. A typical hard corona is formed from the interaction between the NP surface and transferrins, which are liver-produced glycoproteins that mediate the transport of iron in serum to cells through the endocytic pathway with the aid of transferrin receptors (TfR) ubiquitously found on cell plasma membranes. Ample evidence has indicated several-fold higher expression levels of TfR on malignant cells compared to normal cells [142–145], substantially increasing potential specificity and active targeting efficacy of Tf conjugated NP-PC complexes nanocarrier against tumor cells. Experiments using NP-PC complexes coated with Tf (NP-Tf) to deliver anti-cancer drugs either *in vitro* or *in vivo* have shown consistent enhancement in terms of uptake amount and proliferation antagonizing efficacy in comparison to control groups without Tf [146–150].

Despite the aforementioned evidence, the uptake kinetics at the cell level has so far not been fully studied, yet is of great importance for quantitatively understanding the role Tfs plays in the internalization of NP-PC complexes. In the following subsection, I will show time-lapse imaging of the intracellular accumulation of NP-Tf internalized by live HeLa cells within the SPIM modality, followed by data analysis and discussion.

4.2.2 Hard protein corona formation and characterization

Since investigating NP-Tf uptake kinetics does not impose specific requirements on NP material and the cargo it carries, standard 100 nm fluorescent polystyrene beads with sulfate modification (PS-OSO₃H) were adopted for their high affinity to the plasma membrane. To produce NP-Tfs, I first dissolved 5 mg apo-transferrin (the species without iron) powder in 500 μ L DPBS(-/-) to get a high concentration Tf stock solution, the concentration of which was measured using a spectrophotometer (NanoDrop 2000c UV-Vis, Thermo Scientific) based on the Beer-Lambert law with 87 M⁻¹cm⁻¹ extinction coefficient 78 kDa molecular weight of Tf. The stock solution was subsequently diluted by DPBS(-/-) into a concentration gradient ranging from 0.1 μ M to 80 μ M. The NP stock solution was diluted about 40 times to get a 1.4 nM solution calculated from Eq. 3.43.

A fundamental measure, from which one can deduce the structure, composition and stability of the NP-Tf, is its hydrodynamic radius R_H vary with the concentration of Tf, which was measured using the dynamic light scattering method [151, 152]. As this method is vulnerable to bias in the presence of aggregation [153], the bare NP size was measured as shown in the leftmost data point in Fig. 4.4 to confirm the solution is monodisperse before swiftly pipetting a 1.4 nM NP solution into the same volume of a Tf solution with varying concentrations for NP-Tfs formation. After 15 min incubation, the NP-Tf colloid was ready to measure.

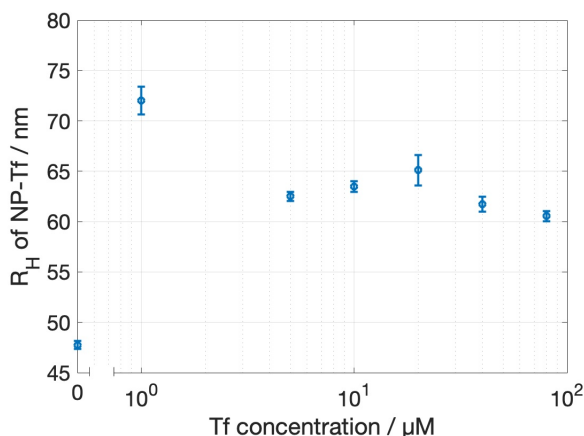


Figure 4.4: Hydrodynamic radius of NP-PC complex. The leftmost data point represents the hydrodynamic radius of bare NPs.

When the Tf concentration was lower than 1 μM , the R_H soared up to the micrometer level, implying the formation of aggregates. As the Tf concentration increased, R_H asymptotically dropped to 62.7 nm. This observation agreed well with the theoretical prediction that the NP surface will be passivated by a monolayer of PC, which measured 14.9 nm in thickness in my experiment, once the critical protein concentration is achieved[154, 155]. It was also reported that once the critical Tf concentration for the formation of the monolayer is surpassed, the Tf density on the monolayer increases with Tf concentration in the colloid while the thickness of the monolayer remains unchanged. Repeated experiments showed a variance in the critical protein concentration, which can be attributed to the variance of the actual NP concentration when pipetted out of stock solution and the variance of the Tf concentration. To overcome this uncertainty, I chose the NP-Tf produced with the critical Tf concentration as a benchmark because whatever absolute concentration the Tf or NP solution had, the NP-Tf bore the same number of Tf proteins adsorbed to the surface of NP. Such an NP-Tf colloid was used for cell uptake experiments.

Performing time-lapse measurement of NP-Tf uptake by live cells requires two channels, one of which records the cell position and morphology while the other is meant for NP-Tf. CellMaskTM Deep Red plasma membrane stain is a ready-to-use dye to indicate the cell membrane. I characterized its fluorescence properties as shown in Fig 4.5b using a Fluorolog-3 fluorescence spectrometer (HORIBA Jobin Yvon, Edison, NJ). There are two alternative PS-OSO₃H labeled with orange and red fluorophore characterized by Fig. 4.5a and c. I opted for orange PS-OSO₃H to minimize fluorescent cross-talk and bleed-through. A 640 nm dichroic mirror was employed to separate signals emitted from the dye and PS-OSO₃H. Furthermore, a 527/70 nm bandpass filter was placed in the PS-OSO₃H channel.

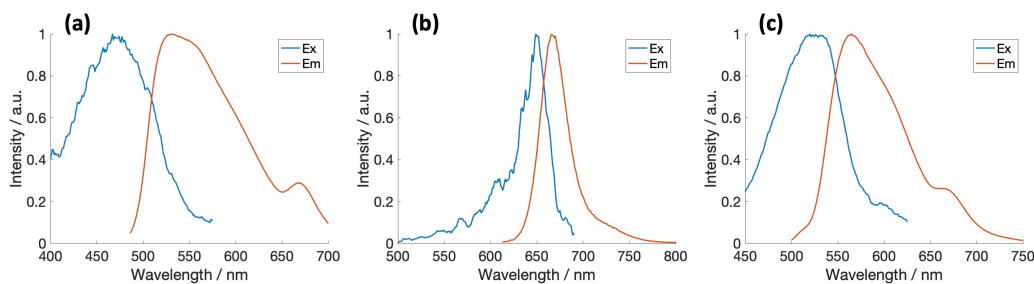


Figure 4.5: Characterization of fluorescence absorption and emission spectra. Spectra for orange PS-OSO₃H, CellMask and red PS-OSO₃H are plotted in (a), (b) and (c), respectively.

4.2.3 Time-lapse imaging

Preliminary imaging of NP-Tfs showed they were subject to photobleaching. As the resolution was not the major concern in this experiment, I opted for Gaussian light-sheet excitation with 2.2 μm waist for both channels by virtue of their minimal light dose distributed to the background. During acquisition, two light sheets were simultaneously scanned across 200 μm in the y direction and 40 μm in the z direction, rendering 6 W/cm^2 and 2 W/cm^2 power density for 473 nm and 561 nm excitation, respectively. Two cameras acquired data simultaneously with 50 ms exposure time every 30 s for 45 min. The raw data were binned internally with 2×2 pixels to save disk space. In between two consecutive acquisitions of stained live HeLa cells immersed in 2.5 mL DPBS (+/+), another 2.5 mL 5 times diluted NP-Tf colloid in DPBS (+/+) was swiftly pipetted into the sample insert. Thus, the effective NP-Tf concentration cells were in contact with was 70 pM.

As with Wnt signaling imaging experiment, the raw data went through two-channel registration, cross-correlation-based drift correction and affine transformation from laboratory to biological coordinates. At last, 400 ADU (2×2 binning also applies for background) was subtracted from processed data. Judging from extended shapes, three cells were considered healthy and selected for uptake kinetic analysis (Fig. 4.6a). No significant cell morphological change between volumes acquired at the beginning and the end of the imaging session was observed, allowing for static segmentation of intracellular spaces throughout the acquisition process using manually defined masks at $t = 0$. I delineated 8 masks for each of 3 cells at different depths from the surface of the coverslip (0 μm) to cell caps (7 μm). Three slices out of the merged volume recorded 10 min post administration are selectively shown in Fig. 4.7, where the red and green channels represent cell membranes and NP-Tf, respectively. Areas covered by masks over depth are shown in Fig. 4.6b.

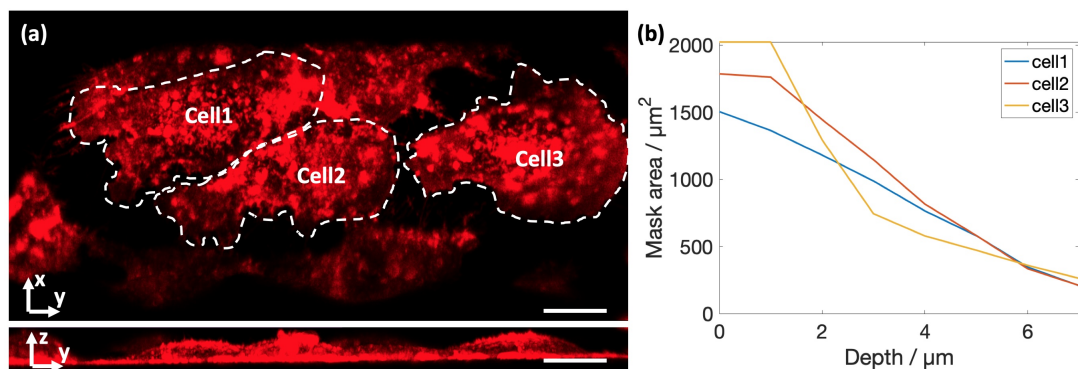


Figure 4.6: Cell segmentations. (a) MIPs of cells 3D reconstruction. (b) Segmentation mask area varies with depth. Cells of interest are labeled with white dashed lines. The rendered volume was captured at $t = 0$. The depth at the surface of the coverslip is set to $0 \mu\text{m}$. Scale bar, $20 \mu\text{m}$.

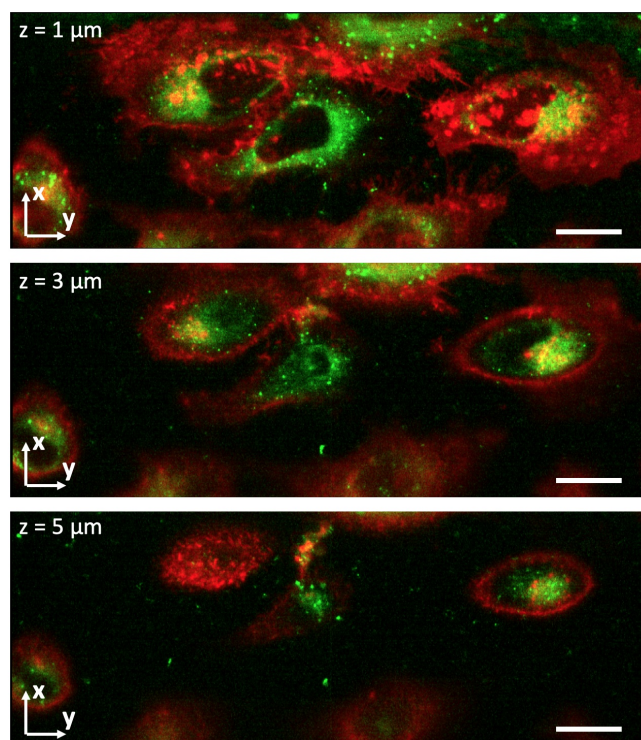


Figure 4.7: Images at different depths of HeLa cells internalizing NP-PC complexes. Three slices are selected from the volume recorded 10 min post administration. Cell membranes and NP-PC complexes are rendered in red and green, respectively. z represents the distance to the surface of the coverslip. Scale bar, $20 \mu\text{m}$.

The endocytosis density at each depth was measured by the mean voxel intensity among the 1 μm thick slice defined by the mask. In doing so, the entire cell can almost be covered by 8 slices. Thus, the overall intracellular NP-Tf level was defined as the average voxel intensity within 8 slices. In Fig. 4.8a, MIPs of merged volumes looking from a certain angle at different post-administration times are shown. Peaks emerge at around 9 min post administration in cumulative endocytosis time traces (Fig. 4.8b). Following the peak was a mild drop and rise again. One possible explanation for the drop is the photobleaching effect, which predominated over the uptake when the latter process was approaching the stationary stage. But this model cannot account for the recovery from dropping after 30 min.

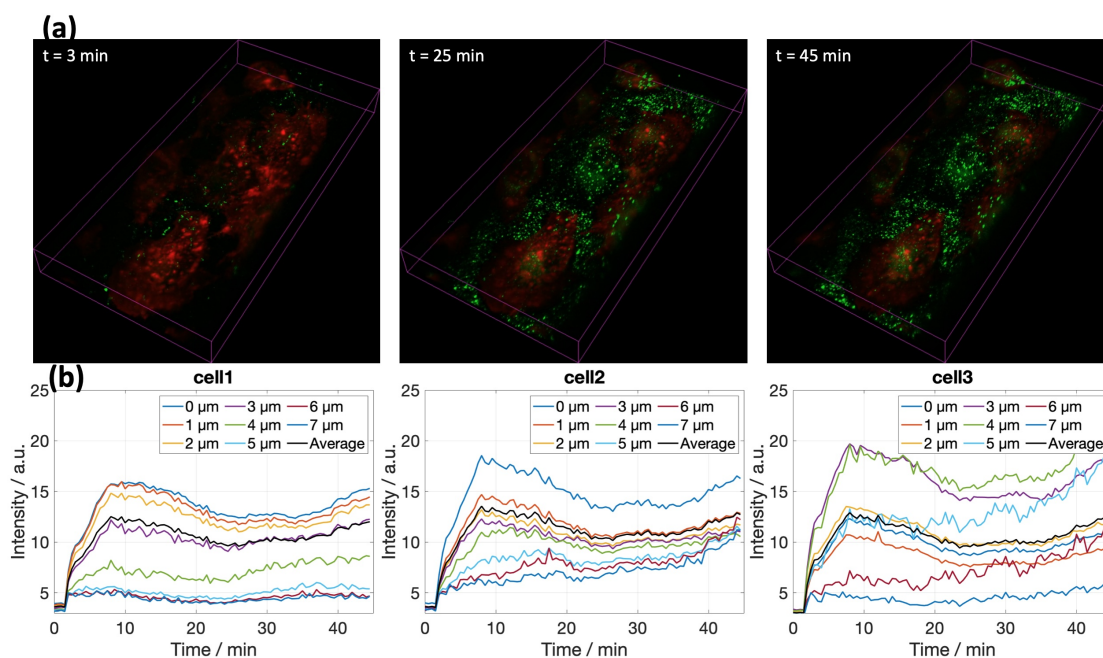


Figure 4.8: Uptake kinetics of NP-PC complexes. (a) MIPs of merged volumes looking from a perspective angle. Cell membranes and NP-PC complexes are rendered in red and green, respectively. (b) Densities of endocytosis at different depths.

Indeed, the overshooting behavior could be the implication of Tf homeostasis. In bodily fluids like blood plasma, cells actively internalize iron-rich Tfs via TfR-mediated endocytosis, unload the iron, transport Tfs back to plasma membranes and expel them through exocytosis to finish the cycle. Whereas in my experiment cells were immersed in DPBS buffer devoid of Tf, leaving all TfRs starved of Tfs. Once exposed to the Tf-coated NP-PC colloid, the high osmotic pressure contrast caused NP-Tf endocytosis to prevail over exocytosis until the condition for the feedback mechanism to take effect was met to steadily establish

Tf cycling equilibrium. Preliminary experiments done by my colleagues using a spinning disk microscope reported a high dependency of the stationary intracellular NP-Tf level on the extracellular NP-Tf concentration. Some datasets showed similar overshooting phenomena only when the extracellular NP-Tf concentration was high, which was, however, not a sufficient condition for the occurrence of overshooting in the same group of measurements. What concentration of NP-Tf would eventually lead to overshooting still remains elusive. Nevertheless, one fact was the equilibrium of NP-Tf exchange across cells membrane was not achieved in 45 min as a rising tendency was observed at the end of acquisition.

Apart from the intracellular accumulation over time, the 3D+t data also allowed for studying the spatial distribution of internalized NP-Tf. For instance, decreasing intracellular NP-Tf density with z in cell1 and cell2 indicated NP-Tfs were apt to accumulate on the bottom of the cells as though they were undergoing passive precipitation while in cell3, NP-Tfs preferentially accumulated at 3-4 μm above the coverslip. Judging from the time-lapse 3D movie, NP-Tf active transport in cell3 was featured by NP-Tfs radially swept to the center of the cell and accumulating to a core suspending over the coverslip (Fig. 4.8a $t = 45$ min). Whether this polarization discrepancy affects the drug administration efficacy is to be investigated.

4.2.4 Discussion

It is worth mentioning that the results shown in this section are intended to validate our microscope's capability. More data shall be collected in order to draw statistically significant conclusions about the endocytosis kinetics, for example, the reliance of stable intracellular NP-Tf level on extracellular NP-Tf concentration and the relationship between uptake rate and Tf density adsorbed to the NP surface. To this end, at least tens of cells from independent measurements need to be analyzed for varying parameters such as the Tf density on the monolayer coating and the NP-Tf concentration administrated to the cells. Additionally, with the fast acquisition mode in concert with the SMLM modality, it should be possible to track the trajectory of individual NP-Tf in the active transport or study the interaction between NP-Tf and endocytosis/exocytosis involved structures such as TfR, clathrin coated pit and endosome/exosome.

4.3 Imaging of microtubules

In this section, I will show the imaging of microtubules in fixed HeLa cells immunolabeled with AF647 to validate the global fitter. As discussed in chapter 2, hundreds of thousands of frames are needed for a full 3D reconstruction of a whole cell. In this process, a compromise between the number of photons per localization and the loss of fluorophores due to bleaching has to be found[99].

I typically opted for 20 ms frame exposure time and 10 kW/cm^2 640 nm laser excitation density. This configuration led to more than one hour of acquisition time, during which drifting originating from either the sample stage or the sample itself was inevitable. Therefore, fiducial markers were coated on the sample to track and correct drifting (red sulfate-modified 100 nm NPs, whose excitation and emission spectra were characterized in Fig. 4.5c). During acquisition, fluorescent light emitted from fiducial markers excited by a 532 nm laser at 1 kW/cm^2 was separated from the AF647 signal via a 640 nm dichroic mirror and subsequently went through a 582/75 bandpass filter before being collected by camera 2. In contrast, the signal from AF647 was simultaneously recorded by the other camera (camera 1) after going through a 650 nm longpass filter. Thus, every dataset containing stochastically blinking AF647 molecules was paired with a dataset, in which sparsely scattered fiducial markers persisted. The trajectories of the fiducial markers covering the whole time points over the course of acquisition can be readily constructed to characterize the dynamics of movements in the sample and stages to compensate for drifting or relative motion between the objective lens and the sample. Since the fiducial markers were bright objects, each one was visible in multiple planes and thus five slices were used to obtain the highest localization precision for fiducial markers and hence optimal drift correction. As the fast mode was deployed to record the data, the image hyperstacks created by each camera were sorted into two groups: forward scanning and backward scanning (see section 3.3.5).

In the following sub-sections, the localization precision is first examined in terms of the m0 dataset. Afterward, the movement of the piezo stage is modeled to calculate the drifting coordinates of a single molecule at any given spatio-temporal point in either m0 or m1 dataset according to the fiducial marker traces. In the end, the 3D reconstructions of microtubules are visualized and quantitatively evaluated.

4.3.1 Localization precision examination

A valid metric to reliably evaluate the localization precision is the standard deviation of a point cloud generated from a repeatedly localized stationary nanoparticle [73]. More precisely, the localization precision is defined as the average distance by which the fitted position of an emitter deviates from the true position. However, because of drifting, the repeated position estimations of a fiducial marker that should have the form of a point cloud manifest in a drifting curve modulated by the noise resulting from fitting uncertainty and mechanical jittering as shown in Fig. 4.9a-c.

The discontinuity in the y and z directions is a consequence of the sample piezo stage repositioning at the end of each hyperstack acquisition by the quasi-closed-loop control (see section 3.4.1). The piecewise application of a sliding

window filter, the output of which is simply the mean value of the time sequence covered by the window, to the trajectory of each hyperstack can approximately extract the drifting curve (Fig. 4.9d-f). The difference between the raw and the smoothed drifting curves gives a fluctuating curve around the origin (Fig. 4.9g-i), the standard deviation of which measures the localization precision.

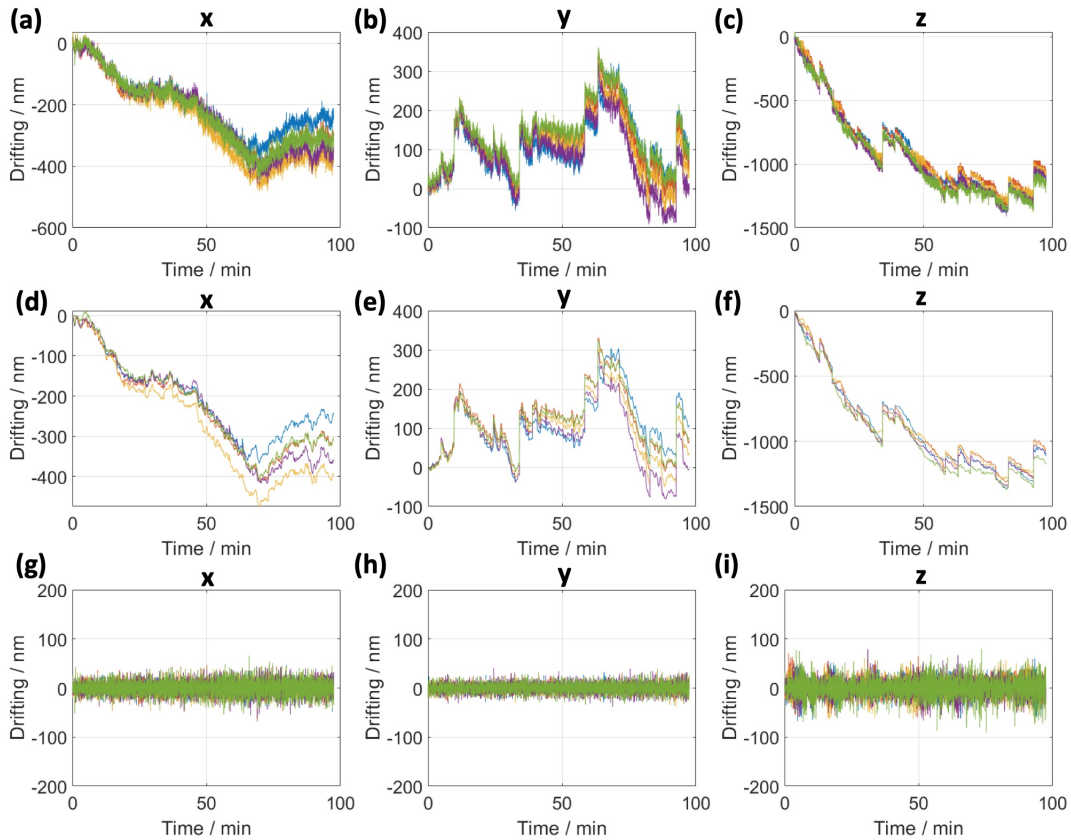


Figure 4.9: Trajectories of fiducial markers. Five fiducial markers randomly scattered among the volume of interest were tracked and encoded in different colors. (a)-(c)Raw drifting traces of fiducial markers. (d)-(f)Smoothed drifting traces of fiducial markers. (g)-(i)Drift-corrected fiducial marker traces represented by the differences between raw and smoothed traces.

The effect of localization precision varying with the changing sliding window was investigated to avoid either overestimating with too narrow a window or underestimating with too wide a window. As shown in Fig. 4.10, the localization precision dramatically degrades with extending window, which smoothes out an increasingly wider noise spectrum in the drifting curves. As a result, the corresponding noise fraction in the raw drifting curves will survive the subtraction. A sliding window with a width beyond 20 not only smoothes the noise but also distorts the drifting curve, giving rise to a systematically biased estimation of

localization precision. Therefore, the localization precision steadily increases with sliding window width as opposed to converging to a constant value. For conservative estimation, the sliding window width was set to 30 volumes in the following discussion if not otherwise specified.

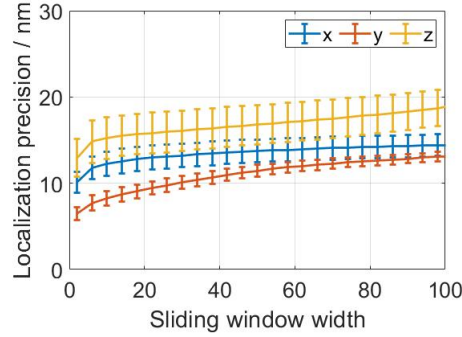


Figure 4.10: Localization precision for different sliding window widths. The localization precision degradation can be classified into two domains. Selectively eliminated noise is responsible for the variation in localization precision when the sliding window width is below 20 while the steady increment of localization precision with a sliding window wider than 20 can be explained by the intrinsic distortion of noise trace due to sliding window smoothing.

Despite the seemingly eliminated jittering, we can not guarantee the succeeding experiments are completely free from jittering due to sporadic occurrences of environmental perturbations that result in 0.1 to 10 Hz jittering noise and the electrical perturbation in the grid contributing to 100 to 200 Hz jittering noise. While the high-frequency jittering deteriorated the recorded PSFs with a 20 ms frame exposure time, the low-frequency noise eventually emerged in the raw drifting curves, blended in the fitting noise and became inseparable. In any case, the measured localization precision from the fiducial marker traces was expected to be no better than the one calculated from the CRLB.

To characterize the dependence of localization precision on the number of photons in the laboratory condition, the corrected localization traces in Fig. 4.9g-i were segmented with respect to the number of photons per localization in photo-bleaching curves shown in Fig. 4.11a. Trace segments, whose numbers of photons fell into the same bin (with size 100), were grouped and treated as a whole when calculating the localization precision.

In the end, the localization precision varying with the number of photons was plotted in Fig. 4.11(b). The localization precision slowly dropped from 12 nm to 8 nm (y) and 18 nm to 11 nm (x and z), whereas the simulation results (Fig. 3.27) reported below 5 nm in all directions when the number of photons is higher than 1000. Although a narrower sliding window will yield a higher localization precision, it will also risk leaving localization noise either from ambient

disturbance or fitting noise of a specific fiducial marker in the smoothed drifting traces that will be used later to correct for global drifting. More importantly, as the low-frequency jittering induced noise cannot be decomposed from the fitting noise, a small sliding window will result in artificially high localization precision. In this regard, Fig. 4.11b can be considered to reflect the realistic localization precision.

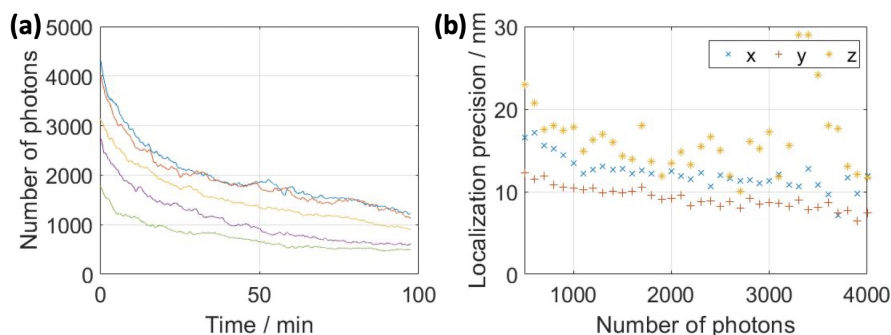


Figure 4.11: Localization precision characterization using bleaching fiducial marker traces. (a) Number of photons time traces of fiducial markers. (b) Localization precision to the number of photons.

To illustrate the advantage of multiple slices fitting over one-slice fitting, I analyzed in the same outlined method the localization precision to the number of photons by fitting the fiducial marker segments with a varying number of slices (Fig. 4.12). Compared to the dataset shown in Fig. 4.11, the dataset used here was obtained on a different day when a 0.1 Hz noise identified as an environmental perturbation occurred in x and y drifting curves with different amplitude. The overall localization precisions deteriorated in response to the jittering noise coupled with the localization noise. Since x and y localizations suffer from the jittering differently by amplitude, a discrepancy in lateral localization precisions can be noticed. The improving localization with the number of slices in x can be presumably explained by the jittering components with frequency as high as the acquisition frame rate that asynchronously displaced the individual slices within the segment. This effect deteriorates the lateral localization precision while can be mitigated by multi-slices fitting. Contrary to the simulated result, 5-slice fitting exhibits remarkable improvement in z localization precision compared to 3-slice fitting as a consequence of greater FWHM of excitation PSF ($1.17\ \mu\text{m}$ as shown in Fig. 3.17b) than $0.56\ \mu\text{m}$ used for simulation.

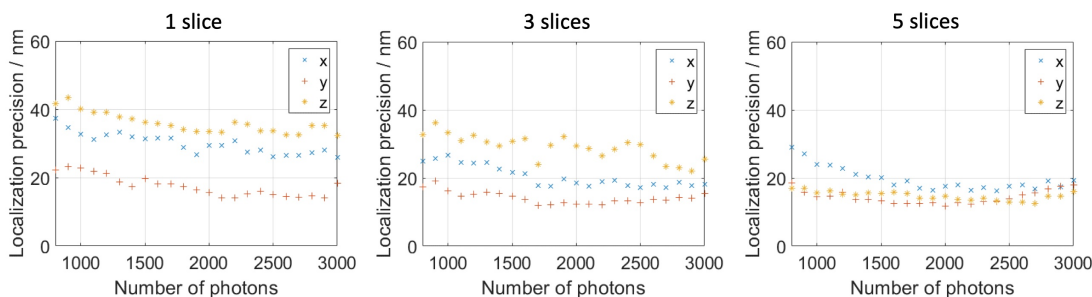


Figure 4.12: Localization precisions with a varying number of slices.

4.3.2 Piezo stage movement modeling

In principle, all fiducial markers should share the identical drifting curve independent of their positions within the imaged volume provided the sample coated with fiducial markers does not deform when drifting. Even though some fiducial markers might be loosely bound to the sample and were performing random movement around binding sites, the noise arising from it should only be of a few nanometers scale. However, a regular splitting of fiducial marker traces in tens of nanometers scale Fig. 4.9d-e was observed, indicating the drifting was systematically coupled by an underlying movement source that brought difficulty in correcting for drifting.

It was not sufficient to depict the movement model based on this single piece of evidence. So far all the discussions only focused on the m0 dataset while a question to be answered is if the fiducial markers present in the m1 dataset were drifting in the same way when speaking of merging m0 and m1 datasets. By taking the difference between smoothed fiducial marker traces of m0 and m1 datasets, one can visualize the discrepancy of drifting curves as shown in Fig 4.13.

Unsurprisingly, fiducial markers were drifting inconsistently in m0 and m1 datasets. The task is to put forward a movement model that accounts for the features of the drifting curve. One can notice that the drifting trace difference denoted by Diff in Fig. 4.13a-b is correlated with the z coordinate of its corresponding fiducial marker. In fact, the slope of the approximately linear curve is linearly related to z and the intercept is a quadratic function of z , which happens to be the scanning direction of the objective piezo stage. It is reasonable to attribute the non-zero Diff to elastic hysteresis of the piezo stage.

Considering that a complete scanning loop of the piezo stage follows the routes illustrated in Fig. 4.14, where the green and orange curves represent the m0 and m1 scanning directions, the lateral position of a static fiducial marker in the m0 image will differ from the position in the m1 image by the distance that m0 and m1 routes are separated at the z position the fiducial marker is located. The intercepts of linear curves in Fig. 4.13a-b can then be fitted to the difference between m0 and m1 routes, which is a Gaussian-like curve asymptotically converging to zero

at two ends. Nevertheless, it is convenient yet rational to do quadratic fitting as most fiducial markers were populated around the top of the Gaussian bell.

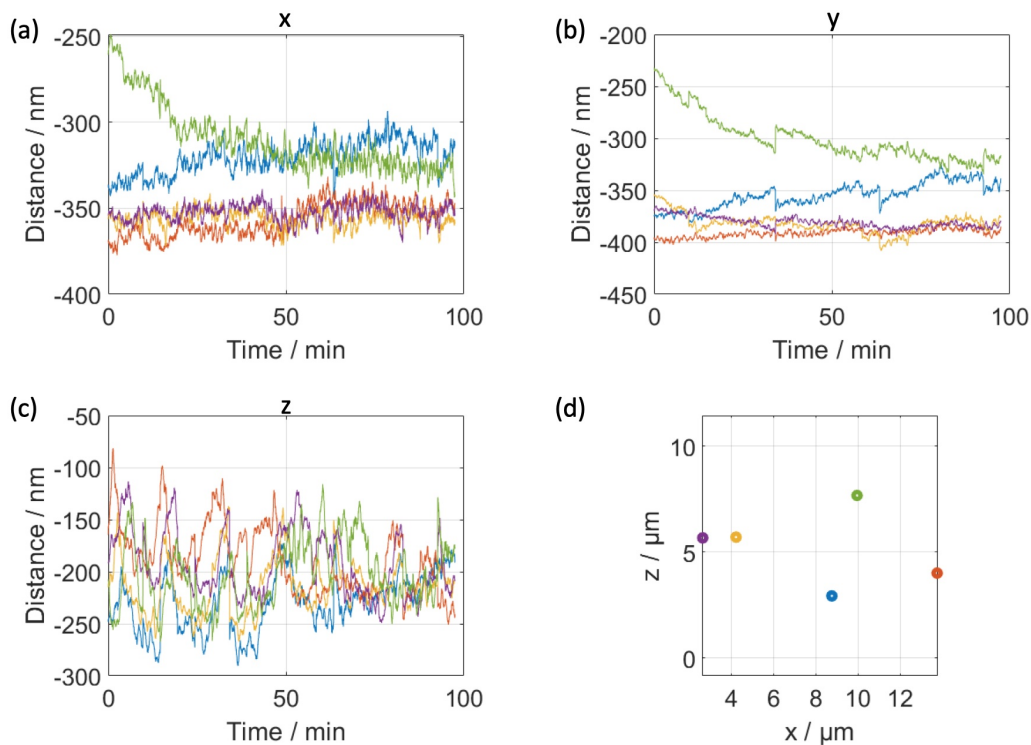


Figure 4.13: Comparison of drifting curves in m0 and m1 datasets. (a)-(c) Differences between smoothed fiducial marker traces in m0 and m1 datasets. (d) Scatter plot of fiducial markers in the volume of interest. All subplots in this figure share the same color map.

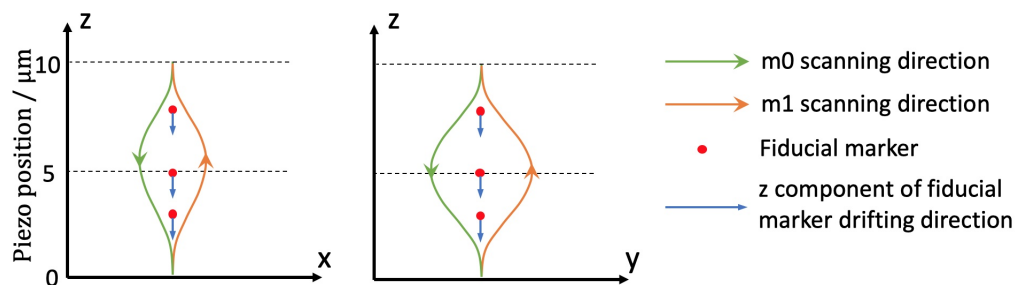


Figure 4.14: Schematic diagram of piezo stage movement with hysteresis.

Since fiducial markers continuously undergo drift especially in z as marked by blue arrows in Fig. 4.14, the Diff is not a constant number but rather an ascending or descending line if the fiducial marker is found above or below 5 μm .

Indeed the slope of the Diff is characterized by the drifting velocity in z and the first derivative of the quadratic curve with respect to z . As a result, the Diff can be written as a function of z and t ,

$$\begin{aligned} \text{Diff}_x(t, z) &= t \cdot \text{slp}_x(z) + \text{intp}_x(z) \\ \text{Diff}_y(t, z) &= t \cdot \text{slp}_y(z) + \text{intp}_y(z), \end{aligned} \quad (4.1)$$

where slp is a linear function of z and intp is a quadratic function of z . Notably, Eq. 4.1 holds only in a limited time interval when the drifting velocity in z is constant. This requirement can be met by piecewise fitting slp and intp for each hyperstack under the condition that the acquisition time for one hyperstack is not excessively long to experience a substantial drift velocity change.

Fitting of the first hyperstack to slp and intp in both x and y directions were plotted in the first column of Fig. 4.15. The poles of two quadratic fits were located near $5 \mu\text{m}$, meaning the hysteresis culminated in the middle of the travel range. The parallel slp and almost overlapping intp indicate that the piezo is traveling along the perimeter of a narrow ellipse on a plane as shown in Fig. 4.14. The time-dependent fitting results validate the necessity of piecewise fitting.

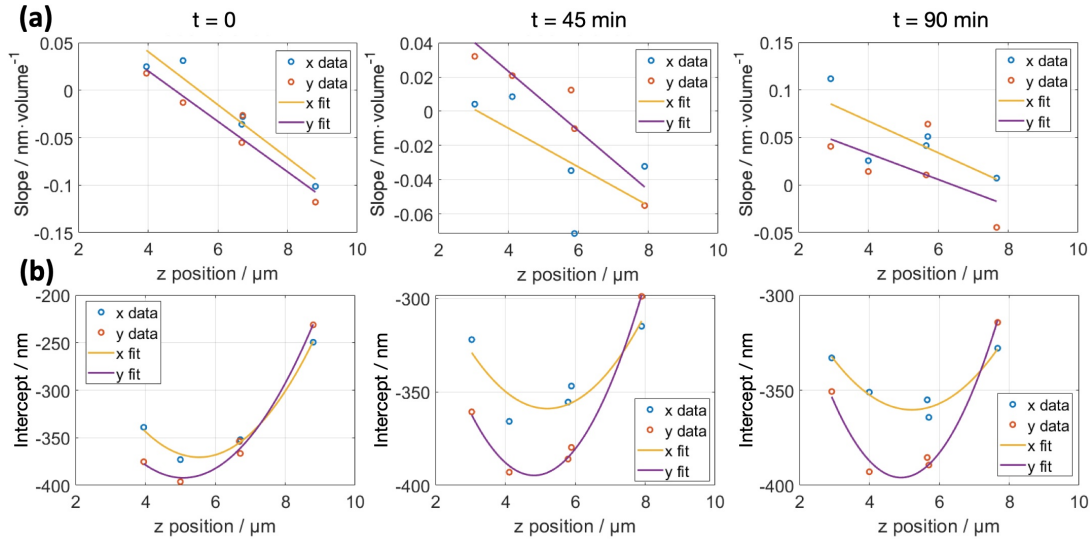


Figure 4.15: Hysteresis characterization of the piezo stage. (a) Linear fits to slope. (b) Quadratic fits to intercept.

As with the Diff evolution with time, the splitting of fiducial marker traces in Fig. 4.9d-e can be explained by drifting in z . Take the m_0 path in the left panel of Fig. 4.14 for example, the curvature of the route does not affect the x drifting curve for the fiducial marker located at $5 \mu\text{m}$ because the lateral drifting contribution of hysteresis is proportional to the first derivative of the m_0 path

with respect to z , which is zeros at the pole. Regarding this drifting curve as a reference, hysteresis and constant drifting in z will cause the fiducial marker traces to diverge away from the reference curve at the velocity proportional to the product of drifting velocity in z and the first derivative of the m0 path with respect to z . Given that the drifting velocity is slow and the scanning path curvature is small such that a constant first derivative governs the area a fiducial marker is traveling across throughout the measurement, the cross-section of the splitting trace at any given time t can be fitted to a linear curve about the z position of fiducial markers,

$$\begin{aligned}\text{Drift}_x(t, z) &= z \cdot \text{slp}_{x,t} + \text{intp}_{x,t} \\ \text{Drift}_y(t, z) &= z \cdot \text{slp}_{y,t} + \text{intp}_{y,t}\end{aligned}\tag{4.2}$$

where $\text{slp}_{.,t}$ and $\text{intp}_{.,t}$ denote the time-dependent slope and intercept, respectively. With these two parameters, one can calculate the drifting curve of a virtual fiducial marker in arbitrary depth, which is useful in drift correction for single molecules.

4.3.3 Data correction pipeline

Correcting drift for a single molecule involves calculating a virtual drifting trace, according to which the single molecule drifts. While the lateral component of the virtual trace can be computed through the piezo stage movement model and fiducial marker traces, the axial component has not been decided yet. Unfortunately, no regular pattern can be recognized from the fluctuating z traces of fiducial markers. A simple method I take here to estimate the axial component is calculating the distance from each fiducial marker to the concerned single molecule. The z trajectory of the fiducial marker closest to the concerned single molecule depicts how the single molecule drifts axially. Thus, the volume of interest is divided into as many segments as the fiducial markers. The fiducial marker in the center of the segment controls z drifting behaviors of all the single molecules found in it. The same treatment was employed to figure out the drifting difference in z Fig. 4.13c for each individual molecule captured at any given spatiotemporal point. Pipelines for drift correction of single molecules in m0 datasets and for merging m0 and m1 are given as illustrated in the flow chart.

For the m0 dataset, the z coordinates for all fiducial markers at the beginning of acquisition (t_0) are used as independent variables in the fits for all slp_t and intp_t at each time point. Single molecules are enumerated and individually corrected in terms of z by the drifting curve of the fiducial marker closest to it. The corrected z position at t_0 is then substituted into Eq. 4.2 to calculate the lateral drifting in x and y at time t .

As for merging m0 and m1 datasets, the procedure generally consists of two parts, registration of the m1 dataset at time t into the m0 dataset and drift

correction. The second step is the same as drift correction for the m0 dataset.

In contrast, the first step involves modeling the piezo stage movement for each time interval covered by hyperstack acquisition when Diff_x^i , Diff_y^i , and Diff_z^i are calculated, where the superscript i represents the i^{th} hyperstack. In the fits for slp^i and intp^i , the benchmark z coordinates of fiducial markers are selected to be those in the m0 dataset at the beginning of the hyperstack t_0^i . The z coordinate of a particular single molecule captured at time t with arbitrary spatial coordinate undergoes two steps of correction to obtain its z position at t_0^i in the m0 dataset, *i.e.*, registration and drift correction. Upon fitting and registration are done, t and z_0^i are substituted into Eq. 4.1 to calculate the lateral values for the concerned molecule in the registration correction. Subtracting the calculated difference between the m0 and m1 datasets from the raw spatial coordinate of the single molecule in the m1 dataset registers it into the m0 dataset. At last, the registration corrected data can be equally treated as the data in m0 in terms of drift correction.

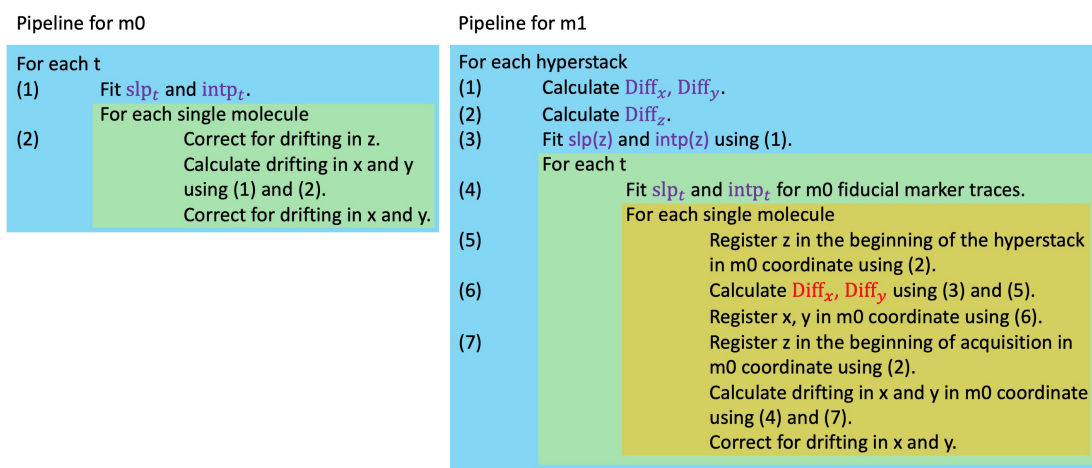


Figure 4.16: Drift correction pipelines for m0 and m1 datasets. Symbols in violet and red represent fiducial marker and single molecule objects, respectively.

4.3.4 Visualization and evaluation of the 3D reconstruction of the microtubules

An open source 3D rendering software ViSP [156] is employed to reconstruct the microtubule structure generated from 6.35×10^5 localizations of the merged dataset (Fig. 4.17a) with hysteresis correction and 3.21×10^5 localizations of the m0 dataset alone (Fig. 4.17b). The affine transformation is applied to each individual localization so that the rendered volumes are presented in biological

coordinates. Microtubule networks on the top (cyan) and bottom (orange) of the cell can be clearly discerned. By virtue of the fast acquisition mode and adaptive correction routine, a high volume acquisition rate of 1 volume per second and 50 slices per volume was achieved.

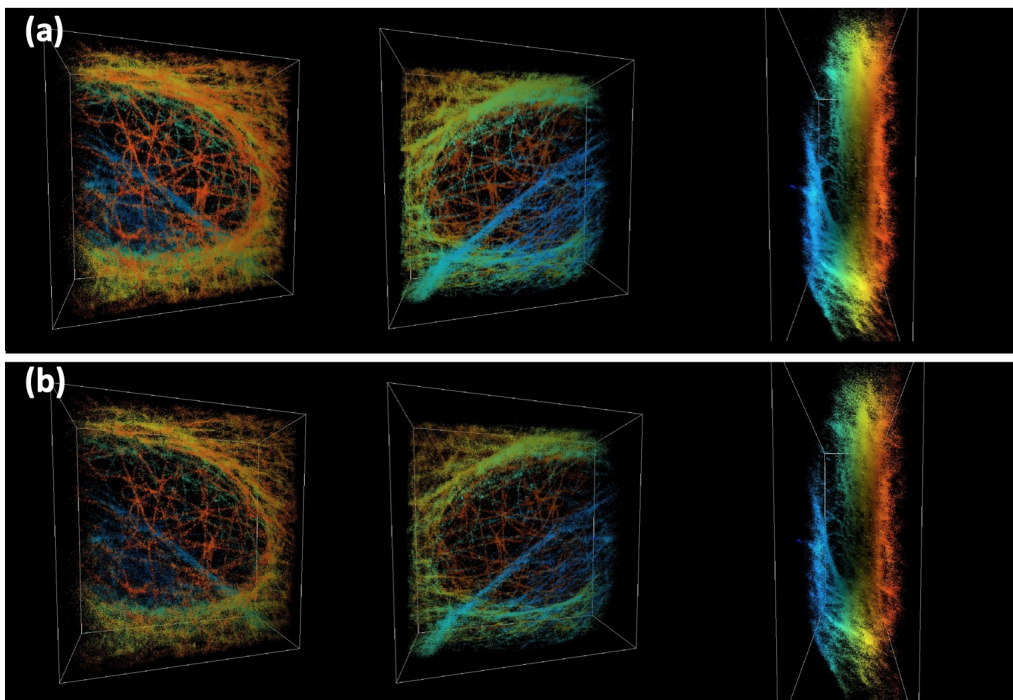


Figure 4.17: Microtubule reconstruction rendered using ViSP. The merged structure (a) of m0 and m1 datasets is made up of 6.35×10^5 localizations within $22 \times 22 \times 8 \mu\text{m}^3$ volume in comparison to 3.21×10^5 localizations in the m0 dataset alone (b). The three images from left to right are viewed from the bottom (the coverslip plane), top and side of the cell, respectively.

In order to verify the drift correction method adapted to the hysteresis model, I generated a control group simply by merging m0 and m1 datasets and correcting for drift with mean difference and drift curves. Localizations falling into a $1.7 \mu\text{m}$ slice close to the coverslip were projected onto a $22 \times 22 \mu\text{m}^2$ image with 5 nm pixel size. This highly pixelized image was then convolved with a Gaussian PSF, whose FWHM was heuristically selected to be 40 nm in light of uncertainty synergically decided by drift correction induced error and localization precision. There are 3 slices per segment of the single molecule dataset and the median number of photons per single molecule is 900, the localization precisions at this region according to Fig. 4.12 are 25 nm , 20 nm and 38 nm for x , y , and z respectively. Therefore, a 40 nm isotropic Gaussian kernel is a conservative estimation of the total uncertainty.

Overall, the reconstructed image using the hysteresis correction method (Fig. 4.18a) is crisper than that with the mean correction method (Fig. 4.18b), however, similarly crisp structures can be found in the latter image (to the right of the image center). This is because, in a certain region, the mean drift curve happens to coincide with the calculated drift curve using the hysteresis model. To quantitatively assess the reconstruction qualities, profiles were plotted across the selected ROIs. The microtubule strands are well-defined by the peaks in hysteresis correction profiles whereas the peaks are less significant in mean correction profiles, especially for microtubules 1 and 6 in profile 2 (Fig. 4.18c).

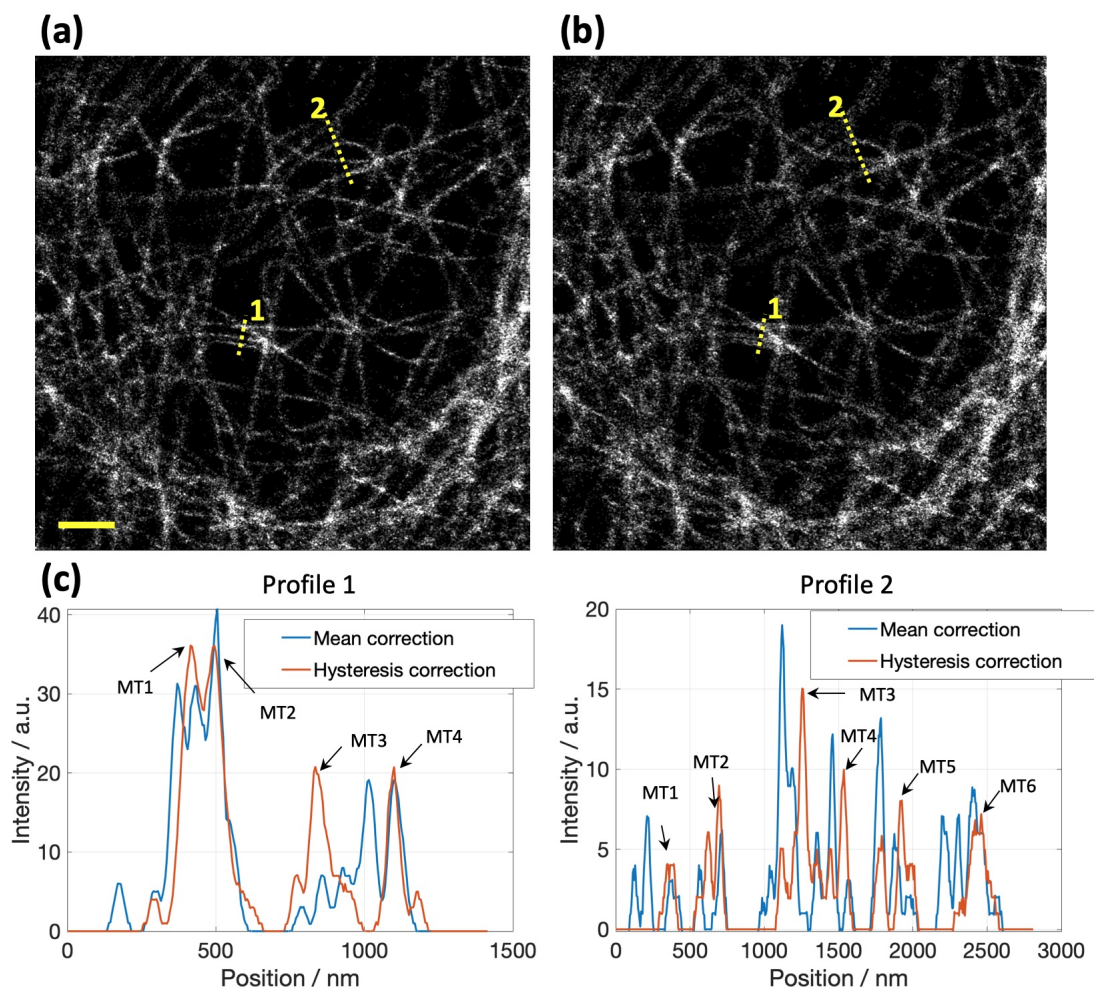


Figure 4.18: Verification of piezo stage movement model. (a)-(b) Localizations found in $1.7 \mu\text{m}$ slice close to the coverslip are projected into 2D images followed by convolution with a Gaussian blur kernel. Hysteresis correction (a) and mean correction (b) methods were used to generate the merged localization dataset. Scale bar, $2 \mu\text{m}$. (c) Profile plots of microtubules in the selected ROIs of (a) and (b).

Decorrelation analysis is a parameter-free method to determine the global resolution of generic super-resolution images based on image partial phase autocorrelation[157]. Applying this analysis to the pixelized image of Fig. 4.18a (*i.e.* without convolution) yields 389 nm resolution, implying the image was undersampled. Sequentially convolving the pixelized image with Gaussian kernels ranging from 10 to 100 nm in FWHM followed by decorrelation analysis showed the resultant resolutions were strongly affected by the Gaussian kernel size, possibly because decorrelation analysis is apt to mistake sparsely isolated localizations for a real biological structure with the spatial frequency defined by the Gaussian kernel size. Therefore the resolution estimation using such analysis is unreliable.

An alternative and straightforward metric to evaluate the resolution is the FWHM of the reconstructed microtubules. Localizations are preferentially visualized in the laboratory coordinate to decouple lateral and axial resolution. As shown in Fig. 4.19a, a representative ROI of $16 \times 10 \times 7 \mu\text{m}^3$ around the cell cap is projected on the lateral plane with color-coded depth information.

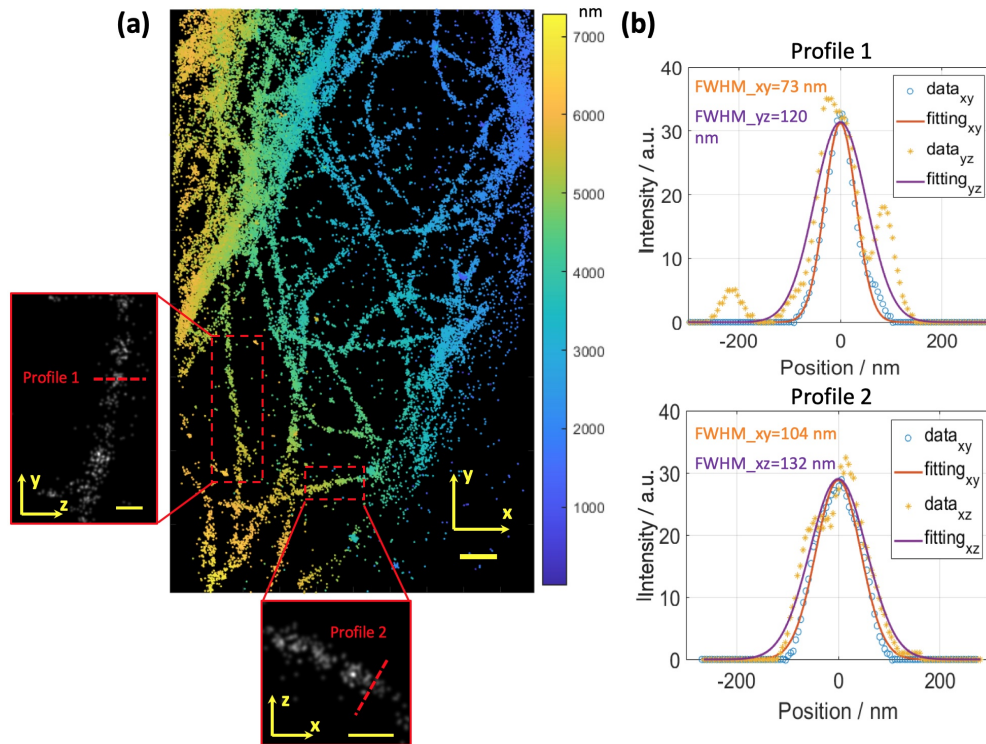


Figure 4.19: Image resolution assessment. (a) Localizations are projected on a plane with color-coded depth information. Projections of selected microtubules on axial planes are shown in the zoom-in boxes. Scale bars, $2 \mu\text{m}$ (main figure) and 500 nm (zoom-in boxes). (b) Profile plots of selected microtubules, which are fitted with 1-D Gaussian curves.

Profiles of two microtubules, whose constituent localizations were convolved with previously defined Gaussian kernel and projected in lateral and axial planes, are plotted and fitted with Gaussian lineshapes. As microtubules were indirectly probed via the fluorophores tagged to the secondary IgG antibodies, which were linked to the epitopes of microtubules through primary IgG antibodies, the apparent diameter of microtubules is the bare diameter of 24 nm plus linkage error. For IgG antibodies, the distance from the Fab end to the Fc end typically measures 10.8 nm [158]. Considering all the possible spatial conformations arising from rotating about binding hinges [159], the average thickness of the fluorophore shell shielding the microtubule is 10.5 nm [160]. As a result, the apparent diameter of the strand structure measures 45 nm on average. Assuming plotted profiles are the stepwise convolutions between the physical structure and localization uncertainty determined Gaussian kernel σ_{loc} and predefined Gaussian kernel with σ_{def} (FWHM = 40 nm), according to associative law of convolution, the localization uncertainty σ_{loc} can be written

$$\sigma_{\text{loc}} = \sqrt{\sigma_{\text{tot}}^2 - \sigma_{\text{def}}^2}, \quad (4.3)$$

where σ_{tot} can be estimated by deconvolving microtubule profiles. Except for FWHM_{xy} that yielded an overestimated localization precision possibly owing to undersampling or the minimized linkage error by chance, FWHM_{yz} in profile1, FWHM_{xy} and FWHM_{xz} in profile2 gave 70 nm, 54 nm and 85 nm localization precisions, respectively.

In terms of quasi-isotropic features, the presented results are consistent with the conclusion drawn from fiducial marker results (Fig. 4.12). However, absolute localization precisions, especially in z direction, are poorer than calibrated from fiducial markers. It has been proven that mean correction, which was used for drift correction in z direction, blurred reconstructed structures (Fig. 4.18). Likewise, the mean correction in z can also account for the large discrepancy in localization precision. Another possible explanation is the sampling rate as shown in the zoom-in boxes of Fig. 4.19a was not sufficiently high to yield a continuous and homogenous structure. In fact, in the middle of the acquisition for the data presented here, the localization events per volume had dropped by 90% compared to the beginning. Improving the image buffer performance with respect to stability and oxygen scavenging efficacy could protect single molecules from photobleaching.

4.3.5 Discussion and conclusion

The superior localization performance of my global fitting algorithm has been experimentally proven by imaging fluorescent beads and microtubule structures. In virtue of fiducial marker-guided drift correction and fast acquisition mode, the

microscope can record at a volume rate of 1 Hz. Given shorter exposure time and fewer slices per volume, an even higher volume rate can be achieved, which is in favor of observing fast processes in live cells using SMLM.

Compared to the simulated results, the capacity of the fitter is not fully exploited as the bottleneck preventing us from obtaining higher resolution is mechanical instability-induced jittering and drift correction errors originating from irregular fluctuations in drift curves. A plausible explanation for this phenomenon is the local RI density flux induced focal plane fluctuation resulting from kinetic equilibrating RI against water and β ME loss by slowly replenishing water at the corner of the sample insert. There is a large room for resolution enhancement such as employing a more stable imaging buffer, improving the airtightness of our homemade incubator and thoroughly isolating mechanical jittering.

Chapter 5

Summary and outlook

5.1 Summary

In this thesis, I presented a 3D fluorescence microscope with tailor-made data analysis software. The versatile microscope features two imaging modalities, *i.e.*, SPIM and SMLM.

SPIM mainly aims at observing cells and tissues in large ROIs and long time spans with a widefield resolution of $380 \text{ nm} \times 380 \text{ nm} \times 730 \text{ nm}$. A fast acquisition mode is developed and characterized, allowing for up to 10 Hz volumetric acquisition rate, which is useful for capturing transient processes where high temporal resolution is required. Five laser lines and two SLMs in the excitation path render great flexibility so that users can customize the illumination strategy in terms of light sheet type, axial resolution, covered FOV, tolerance to background excitation and photobleaching *etc.*, to meet task-oriented requirements.

With minimal effort, the microscope can be switched to SMLM for super-resolution imaging. I developed a global segmentation and localization algorithm particularly suitable for the data obtained using the fast acquisition mode under light sheet illumination, in which a single emitter can be found in consecutive slices within the volume. Repetitive fitting of the same emitter is avoided by fitting 3D emitters in one stroke while the localization precision is promoted to quasi-isotropic 20 nm with less than 1000 photons per emitter. Thus, fluorophores once thought to be inapplicable because of low photon counts per on-off switch event are suitable for the introduced microscope, substantially broadening the alternative pool for multichannel labeling and the spectrum of biological problems that can be studied with the microscope.

In the results chapter, I showed two biological applications of my microscope. For the Wnt signaling topic, intercellular transportation of Wnt vesicles inside a hollow tube of the filopodia network of live H1703 cells was resolved by virtue of the high widefield 3D resolution. The active transport velocity was examined. The cell-to-matter interaction between nanoparticles and live HeLa cells was in-

investigated and the uptake kinetics of nanoparticles with critical coating density revealed the regulation of Tf to reach homeostasis. Spatially inhomogeneous accumulation of nanoparticles within cells implied active transporting and polarizing of nanoparticles. Proof-of-principle experiments by imaging microtubules in SMLM modality demonstrated the high capability of my fitter in resolving subcellular structures.

5.2 Outlook

By the time the thesis is submitted, multiple biological projects based on the reported microscope are starting to unfold. A systematic investigation into the uptake rate and the stationary plateau height with a range of Tf coating density will be carried out. With the aid of the fast acquisition mode and the global localization algorithm, we are able to track the trajectory of individual nanoparticles throughout their lifetime. The whole 4D cell-nanoparticles interaction map can then be created. Multi-channel measurements, for instance, the colocalization of nanoparticles and clathrin coated pit, will help to elucidate the exact pathway involved in nanoparticles endocytosis [161]. Other planned biological projects are examining the affinity of Wnt and its chaperon Evi using light sheet imaging fluorescence correlation spectroscopy [162] and studying the roles of caveolae and dysferlin in cell membrane reparation [163, 164].

In addition to biological applications, technical research and development on the established microscope are ongoing. One of the ongoing projects is the implementation of the segmentation and fitting algorithms to the controlling software, which will enable live fitting and visualization in the future. Furthermore, the real-time fitting feature and piezo-actuated mirrors can automate the routine alignment work with a click, potentially rendering our equipment accessible to inexperienced users. To meet requirements imposed by imaging thick samples such as tissues or entire embryos, adaptive optics [105] will eventually be implemented in the detection path for sample-induced aberration correction. A deformable mirror with a large dynamic range and a broad operation bandwidth can foreseeably replace the scanning of the piezo stage of the detection objective lens, considerably improving its mechanical stability. As a result, an enclosed environmental chamber can be employed to meet the physiological demands of the organisms to be imaged, rendering high resolution *in vivo* studies accessible.

Zusammenfassung

In dieser Arbeit habe ich ein 3D-Fluoreszenzmikroskop mit maßgeschneiderter Datenanalysesoftware vorgestellt. Dabei wurden zwei Bildgebungsmodalitäten vorgestellt und weiterentwickelt, Single-Plane-Illumination-Microscopy (SPIM) und Single-Molecule-Localization-Microscopy (SMLM). SPIM zielt hauptsächlich auf die Beobachtung von Zellen und Geweben in großen räumlichen und Zeitlichen Bereichen mit einer räumlichen Auflösung von $380 \text{ nm} \times 380 \text{ nm} \times 730 \text{ nm}$. Es wurde ein schneller Aufnahmemodus entwickelt und charakterisiert, der eine volumetrische Aufnahmezeit von bis zu 10 Hz ermöglicht, was für die Erfassung von transienten Prozessen nützlich ist, bei denen eine hohe zeitliche Auflösung von Bedeutung ist. Im Gegensatz dazu dient SMLM der Maximierung der räumlichen Auflösung durch sequenzielle Detektion einzelner Fluorophore.

Fünf Laserlinien und zwei räumliche Lichtmodulatoren im Anregungspfad bieten eine hohe Flexibilität, so dass der Benutzer die Beleuchtungsstrategie in Bezug auf den Lichtblatttyp, die axiale Auflösung, den abgedeckten Bildbereich, die Toleranz gegenüber Hintergrundanregung und Photobleichen an die jeweiligen Anforderungen anpassen kann. Das Mikroskop kann mit minimalem Aufwand auf SMLM umgeschaltet werden, um hochauflösende Bilder zu erhalten.

Ich habe einen globalen Segmentierungs- und Lokalisierungsalgorithmus entwickelt, der sich besonders für Daten eignet, bei denen ein einzelner Emitter in aufeinanderfolgenden Schichten innerhalb des Volumens detektiert wird. Durch Kenntnis der dreidimensionalen Punktpreisfunktion des Systems lässt sich die Lokalisierungsgenauigkeit auf quasi-isotrope 20 nm mit weniger als 1000 Photonen pro Emitter erhöhen. Somit sind Fluorophore, von denen man früher dachte, sie seien wegen der geringen Photonenausbeute nicht für Einzelmolekülmikroskopie verwendbar, für das vorgestellte Mikroskop nutzbar. Im Kapitel über die Ergebnisse habe ich zwei Anwendungen aus dem Bereich der Biologie vorgestellt. So habe ich im Kontext des Wnt-Signalwegs der interzelluläre Transport von Wnt-Vesikeln in interzellulären Nanotunneln von lebenden Lungenepithelzellen dargestellt und die aktive Transportgeschwindigkeit ermittelt. Desweiteren habe ich die hohe 3D Auflösung des Systems am Zytoskelett von fixierten Epithelzellen demonstriert.

Appendix

Cell culture

Two cell lines were used in this thesis, NCI-H1703 cells and HeLa cells, respectively cultured in $1\times$ 1640 RPMI medium (11835-030, GibcoTM) with 10% qualified FBS (10270-106, GibcoTM) and 1% sodium pyruvate (S8636, Sigma-Aldrich[®]) and in $1\times$ DMEM medium (21063-029, GibcoTM) with 10% FBS. Briefly, cells were incubated in cell flasks (10062-868, VWR[®]) in 37 °C and 5% CO₂ concentration milieu and split in an air flow hood twice a week while confluency reached 100%. The cell splitting protocols are as follows:

- Wash cells using 5 mL pre-heated $1\times$ DPBS without calcium chloride and magnesium chloride (14190-144, GibcoTM) for two times.
- Aspirate DPBS(-/-) from the flask and apply 250 μ L $10\times$ trypsin (59418C, Sigma-Aldrich[®]) to cells.
- Gently shake the flask such that cells are fully immersed in trypsin and incubate at room temperature for 3 min.
- Inject 4 mL cell-culture medium into the cell flask and repeatedly pipette 2 mL medium out of the previously added 4 mL medium against the flask surface 30-40 times using a 5 mL pipette tip (with large opening) until cells are monodisperse in medium.
- Take 250 μ L mixture to a new flask and add 4.75 mL fresh medium.
- Take out 500 μ L mixture and aspirate the remaining liquid out of the flask. Add the mixture back to the old flask and replenish the flask up to 5 mL fluid as a backup.
- Gently shake flasks to uniformly seed cells and move them to the incubator.

In case cells are not attaching to the flask 24 h after splitting, residual trypsin might be the reason. One can sediment cells by centrifuging the cell-medium mixture in a centrifuge tube after procedure 4 at $10\times$ g for 3 min. Afterward, the

supernatant has to be carefully aspirated out of the centrifuge tube and re-suspend cells in 4 mL fresh medium.

Cell freezing and thawing

Cells can be frozen and stored at liquid nitrogen temperature for long times. Typically, multiple aliquots of one cell line should be kept in stock to allow for restarting a new cycle of cell culturing upon needed. The cell freezing protocol is as follows:

- Grow cells in two standard cell flasks. Proceed on to next step by the time the confluency achieves 70%.
- Mix 0.75 mL dimethyl sulfoxide (D8418, Sigma-Aldrich®) in 8.9 mL cell culture medium intended for cells to be frozen.
- Add the mixture into 1.1 mL FBS and gently mix them up to get the final freezing medium with around 10% Dimethyl sulfoxide in volume. Put the freezing medium on ice.
- Split cells in two flasks in the same way as described in cell culture protocol steps 1-3.
- Re-suspend detached cells in 5 mL cell culture medium and moderately pipette.
- Collect cells from two flasks together with cell culture medium in one 15 mL centrifugation tube and centrifuge for 3 min at $100\times g$.
- Carefully aspirate supernatant without touching the sedimented cells.
- Re-suspend cells in 6 mL freezing medium, aliquot 4 labeled cryo vials. Tightly close the lids.
- Put cryo vials in the freezing container and put the container in the $-80\text{ }^{\circ}\text{C}$ freezer overnight. Make sure the 100% isopropyl alcohol in the container underwent less than 5 times cooling and warming cycles or otherwise refill isopropanol.
- Move cryo vials in the liquid nitrogen tank.

The protocol for cell thawing is as follows:

- Take out the vial from liquid nitrogen tank and put it on ice when transferring.
- Fast defrost vial in $37\text{ }^{\circ}\text{C}$ water bath for 2 min.

- Transfer cells together with freezing medium into 15 mL centrifuge tube and centrifuge at $300\times$ g or 1780 rpm for 3 min.
- Aspirate supernatant and re-suspend cells in 5 mL corresponding cell culture medium.
- Incubate cells in flask and change medium 6 h later to remove dead cells.
- Grow at least one generation before using the cells in routine biological measurement.

List of Abbreviations

ADU	Analog to Digital Unit
AF647	Alexa Fluor 647
BFA	Back Focal Aperture
CRLB	Cramer-Rao Lower Bound
DAQ	Data AcQuisition
FOV	Field Of View
FP	Fluorescence Protein
FWHM	Full Width at Half Maximum
GFP	Green Fluorescence Protein
GPU	Graphics Processing Unit
GUI	Graphic User Interface
HOMO	Highest Occupied Molecular Orbital
LCOS	Liquid Crystal On Silicon
LUMO	Lowest Unoccupied Molecular Orbital
LUT	Look-Up Table
MIP	Maximum Intensity Projection
MLE	Maximum Likelihood Estimation
NA	Numerical Aperture
NPs	Nano Particles
NP-PC	Nano Particle Protein Corona
PALM	PhotoActivated Localization Microscopy
PDF	Probability Density Function

PSF	P oint S pread F unction
QY	Q uantum Y ield
RI	R efractive I ndex
ROI	R egion O f I nterest
SBR	S ignal to B ackground R atio
sCMOS	scientific C omplementary M etal- O xide S emiconductor
SIM	S tructured I llumination M icroscopy
SLM	S patial L ight M odulator
SMLM	S ingle M olecule L ocalization M icroscopy
SNR	S ignal to N oise R atio
SPIM	S elective P lane I llumination M icroscopy
STED	S Timulated E mission D epletion
STORM	S Tochastic O ptical R econstruction M icroscopy
Tf	T ransferrin
TfR	T ransferrin R eceptors
TNT	T unneling N ano T ube
WBNS	W avelet-based B ackground and N oise S ubtraction

Bibliography

- [1] Rafael Fernandez-Leiro and Sjors HW Scheres. “Unravelling biological macromolecules with cryo-electron microscopy”. In: *Nature* 537.7620 (2016), pp. 339–346.
- [2] Philipp J Keller et al. “Reconstruction of zebrafish early embryonic development by scanned light sheet microscopy”. In: *science* 322.5904 (2008), pp. 1065–1069.
- [3] Raju Tomer et al. “Quantitative high-speed imaging of entire developing embryos with simultaneous multiview light-sheet microscopy”. In: *Nature methods* 9.7 (2012), pp. 755–763.
- [4] Liang Gao et al. “Noninvasive imaging beyond the diffraction limit of 3D dynamics in thickly fluorescent specimens”. In: *Cell* 151.6 (2012), pp. 1370–1385.
- [5] Bi-Chang Chen et al. “Lattice light-sheet microscopy: imaging molecules to embryos at high spatiotemporal resolution”. In: *Science* 346.6208 (2014), p. 1257998.
- [6] Jun Abe et al. “Light sheet fluorescence microscopy for in situ cell interaction analysis in mouse lymph nodes”. In: *Journal of immunological methods* 431 (2016), pp. 1–10.
- [7] Alex T Ritter et al. “Actin depletion initiates events leading to granule secretion at the immunological synapse”. In: *Immunity* 42.5 (2015), pp. 864–876.
- [8] Misha B Ahrens et al. “Whole-brain functional imaging at cellular resolution using light-sheet microscopy”. In: *Nature methods* 10.5 (2013), pp. 413–420.
- [9] Ludovico Silvestri et al. “Quantitative neuroanatomy of all Purkinje cells with light sheet microscopy and high-throughput image analysis”. In: *Frontiers in neuroanatomy* 9 (2015), p. 68.
- [10] Tomoyuki Mano et al. “Whole-brain analysis of cells and circuits by tissue clearing and light-sheet microscopy”. In: *Journal of Neuroscience* 38.44 (2018), pp. 9330–9337.

- [11] Fabian F Voigt et al. “The mesoSPIM initiative: open-source light-sheet microscopes for imaging cleared tissue”. In: *Nature methods* 16.11 (2019), pp. 1105–1108.
- [12] Hiroki R Ueda et al. “Whole-brain profiling of cells and circuits in mammals by tissue clearing and light-sheet microscopy”. In: *Neuron* 106.3 (2020), pp. 369–387.
- [13] Andrei Y Kobitski et al. “An ensemble-averaged, cell density-based digital model of zebrafish embryo development derived from light-sheet microscopy data with single-cell resolution”. In: *Scientific reports* 5.1 (2015), p. 8601.
- [14] Adam K Glaser et al. “Light-sheet microscopy for slide-free non-destructive pathology of large clinical specimens”. In: *Nature biomedical engineering* 1.7 (2017), p. 0084.
- [15] David Twapokera Mzinza et al. “Application of light sheet microscopy for qualitative and quantitative analysis of bronchus-associated lymphoid tissue in mice”. In: *Cellular & molecular immunology* 15.10 (2018), pp. 875–887.
- [16] S Abadie et al. “3D imaging of cleared human skin biopsies using light-sheet microscopy: A new way to visualize in-depth skin structure”. In: *Skin Research and Technology* 24.2 (2018), pp. 294–303.
- [17] Alistair N Boettiger et al. “Super-resolution imaging reveals distinct chromatin folding for different epigenetic states”. In: *Nature* 529.7586 (2016), pp. 418–422.
- [18] Ke Xu, Guisheng Zhong, and Xiaowei Zhuang. “Actin, spectrin, and associated proteins form a periodic cytoskeletal structure in axons”. In: *Science* 339.6118 (2013), pp. 452–456.
- [19] Yaron M Sigal, Ruobo Zhou, and Xiaowei Zhuang. “Visualizing and discovering cellular structures with super-resolution microscopy”. In: *Science* 361.6405 (2018), pp. 880–887.
- [20] Jarrod B French et al. “Spatial colocalization and functional link of purinosomes with mitochondria”. In: *Science* 351.6274 (2016), pp. 733–737.
- [21] Bogdan Bintu et al. “Super-resolution chromatin tracing reveals domains and cooperative interactions in single cells”. In: *Science* 362.6413 (2018), eaau1783.
- [22] Francesca Cella Zanacchi et al. “Live-cell 3D super-resolution imaging in thick biological samples”. In: *Nature methods* 8.12 (2011), pp. 1047–1049.
- [23] Felix Wäldchen et al. “Whole-cell imaging of plasma membrane receptors by 3D lattice light-sheet dSTORM”. In: *Nature communications* 11.1 (2020), pp. 1–6.

- [24] Jun John Sakurai and Eugene D Commins. *Modern quantum mechanics, revised edition*. 1995.
- [25] William W Parson. *Modern optical spectroscopy*. Vol. 2. Springer, 2007.
- [26] Anunay Samanta. “Dynamic stokes shift and excitation wavelength dependent fluorescence of dipolar molecules in room temperature ionic liquids”. In: *The Journal of Physical Chemistry B* 110.28 (2006), pp. 13704–13716.
- [27] Gerd Binnig and Heinrich Rohrer. “Scanning tunneling microscopy”. In: *IBM Journal of research and development* 44.1/2 (2000), p. 279.
- [28] Marc Adrian et al. “Cryo-electron microscopy of viruses”. In: *Nature* 308.5954 (1984), pp. 32–36.
- [29] Joseph W Goodman. *Introduction to Fourier optics*. Roberts and Company publishers, 2005.
- [30] Monica Monici. “Cell and tissue autofluorescence research and diagnostic applications”. In: *Biotechnology annual review* 11 (2005), pp. 227–256.
- [31] Julian M Menter. “Temperature dependence of collagen fluorescence”. In: *Photochemical & Photobiological Sciences* 5.4 (2006), pp. 403–410.
- [32] Alexey Sharonov and Robin M Hochstrasser. “Wide-field subdiffraction imaging by accumulated binding of diffusing probes”. In: *Proceedings of the National Academy of Sciences* 103.50 (2006), pp. 18911–18916.
- [33] Georgeta Crivat and Justin W Taraska. “Imaging proteins inside cells with fluorescent tags”. In: *Trends in biotechnology* 30.1 (2012), pp. 8–16.
- [34] Murat Sunbul et al. “Super-resolution RNA imaging using a rhodamine-binding aptamer with fast exchange kinetics”. In: *Nature Biotechnology* 39.6 (2021), pp. 686–690.
- [35] Richard A Zsigmondy. “Properties of colloids”. In: *Nobel lecture* 11 (1926).
- [36] Arne H Voie, DH Burns, and FA Spelman. “Orthogonal-plane fluorescence optical sectioning: Three-dimensional imaging of macroscopic biological specimens”. In: *Journal of microscopy* 170.3 (1993), pp. 229–236.
- [37] Jan Huisken et al. “Optical sectioning deep inside live embryos by selective plane illumination microscopy”. In: *Science* 305.5686 (2004), pp. 1007–1009.
- [38] Feifei Wang et al. “Light-sheet microscopy in the near-infrared II window”. In: *Nature methods* 16.6 (2019), pp. 545–552.
- [39] Matthew Jemielita et al. “Comparing phototoxicity during the development of a zebrafish craniofacial bone using confocal and light sheet fluorescence microscopy techniques”. In: *Journal of biophotonics* 6.11-12 (2013), pp. 920–928.

- [40] Tony Wilson. “Confocal microscopy”. In: *San Diego* (1990).
- [41] Akihiko Nakano. “Spinning-disk confocal microscopy—a cutting-edge tool for imaging of membrane traffic”. In: *Cell structure and function* 27.5 (2002), pp. 349–355.
- [42] Lothar Schermelleh et al. “Subdiffraction multicolor imaging of the nuclear periphery with 3D structured illumination microscopy”. In: *science* 320.5881 (2008), pp. 1332–1336.
- [43] Philipp J Keller et al. “Fast, high-contrast imaging of animal development with scanned light sheet-based structured-illumination microscopy”. In: *Nature methods* 7.8 (2010), pp. 637–642.
- [44] Christoph J Engelbrecht and Ernst H Stelzer. “Resolution enhancement in a light-sheet-based microscope (SPIM)”. In: *Optics letters* 31.10 (2006), pp. 1477–1479.
- [45] B. Amos, G. McConnell, and T. Wilson. “2.2 Confocal Microscopy”. In: *Comprehensive Biophysics*. Ed. by Edward H. Egelman. Amsterdam: Elsevier, 2012, pp. 3–23. ISBN: 978-0-08-095718-0.
- [46] Max Born and Emil Wolf. *Principles of optics: electromagnetic theory of propagation, interference and diffraction of light*. Elsevier, 2013.
- [47] Orazio Svelto and David C Hanna. *Principles of lasers*. Vol. 4. Springer, 1998.
- [48] JJJM Durnin, JJ Miceli Jr, and Joseph H Eberly. “Diffraction-free beams”. In: *Physical review letters* 58.15 (1987), p. 1499.
- [49] Georgios A Siviloglou and Demetrios N Christodoulides. “Accelerating finite energy Airy beams”. In: *Optics letters* 32.8 (2007), pp. 979–981.
- [50] Liang Gao et al. “3D live fluorescence imaging of cellular dynamics using Bessel beam plane illumination microscopy”. In: *Nature protocols* 9.5 (2014), pp. 1083–1101.
- [51] Eugen Baumgart and Ulrich Kubitscheck. “Scanned light sheet microscopy with confocal slit detection”. In: *Optics express* 20.19 (2012), pp. 21805–21814.
- [52] Florian O Fahrbach and Alexander Rohrbach. “Propagation stability of self-reconstructing Bessel beams enables contrast-enhanced imaging in thick media”. In: *Nature communications* 3.1 (2012), pp. 1–8.
- [53] Eric Betzig. “Sparse and composite coherent lattices”. In: *Physical Review A* 71.6 (2005), p. 063406.
- [54] Stefan W Hell and Jan Wichmann. “Breaking the diffraction resolution limit by stimulated emission: stimulated-emission-depletion fluorescence microscopy”. In: *Optics letters* 19.11 (1994), pp. 780–782.

- [55] Mats GL Gustafsson. “Surpassing the lateral resolution limit by a factor of two using structured illumination microscopy”. In: *Journal of microscopy* 198.2 (2000), pp. 82–87.
- [56] Mickaél Lelek et al. “Single-molecule localization microscopy”. In: *Nature Reviews Methods Primers* 1.1 (2021), pp. 1–27. URL: <http://www.nature.com/articles/s43586-021-00038-x/>.
- [57] Eric Betzig et al. “Imaging intracellular fluorescent proteins at nanometer resolution”. In: *science* 313.5793 (2006), pp. 1642–1645.
- [58] Michael J Rust, Mark Bates, and Xiaowei Zhuang. “Sub-diffraction-limit imaging by stochastic optical reconstruction microscopy (STORM)”. In: *Nature methods* 3.10 (2006), pp. 793–796.
- [59] Konstantin A Lukyanov et al. “Photoactivatable fluorescent proteins”. In: *Nature Reviews Molecular Cell Biology* 6.11 (2005), pp. 885–890.
- [60] Mariano Bossi et al. “Multicolor far-field fluorescence nanoscopy through isolated detection of distinct molecular species”. In: *Nano letters* 8.8 (2008), pp. 2463–2468.
- [61] Jonathan B Grimm et al. “Bright photoactivatable fluorophores for single-molecule imaging”. In: *Nature methods* 13.12 (2016), pp. 985–988.
- [62] Jörg Wiedenmann et al. “EosFP, a fluorescent marker protein with UV-inducible green-to-red fluorescence conversion”. In: *Proceedings of the National Academy of Sciences* 101.45 (2004), pp. 15905–15910.
- [63] Karin Nienhaus and Gerd Ulrich Nienhaus. “Fluorescent proteins of the EosFP clade: intriguing marker tools with multiple photoactivation modes for advanced microscopy”. In: *RSC Chemical Biology* 2.3 (2021), pp. 796–814.
- [64] Manuel Alexander Mohr et al. “Rational Engineering of Photoconvertible Fluorescent Proteins for Dual-Color Fluorescence Nanoscopy Enabled by a Triplet-State Mechanism of Primed Conversion”. In: *Angewandte Chemie International Edition* 56.38 (2017), pp. 11628–11633.
- [65] Russell E Thompson, Daniel R Larson, and Watt W Webb. “Precise nanometer localization analysis for individual fluorescent probes”. In: *Biophysical journal* 82.5 (2002), pp. 2775–2783.
- [66] Wesley R Legant et al. “High-density three-dimensional localization microscopy across large volumes”. In: *Nature methods* 13.4 (2016), pp. 359–365.
- [67] Hari Shroff et al. “Live-cell photoactivated localization microscopy of nano-scale adhesion dynamics”. In: *Nature methods* 5.5 (2008), pp. 417–423.

- [68] James E Fitzgerald, Ju Lu, and Mark J Schnitzer. “Estimation theoretic measure of resolution for stochastic localization microscopy”. In: *Physical review letters* 109.4 (2012), p. 048102.
- [69] Fang Huang et al. “Video-rate nanoscopy using sCMOS camera-specific single-molecule localization algorithms”. In: *Nature methods* 10.7 (2013), pp. 653–658.
- [70] Anna-Karin Gustavsson et al. “3D single-molecule super-resolution microscopy with a tilted light sheet”. In: *Nature communications* 9.1 (2018), pp. 1–8.
- [71] Carlas S Smith et al. “Fast, single-molecule localization that achieves theoretically minimum uncertainty”. In: *Nature methods* 7.5 (2010), pp. 373–375.
- [72] Jeongmin Kim et al. “Oblique-plane single-molecule localization microscopy for tissues and small intact animals”. In: *Nature methods* 16.9 (2019), pp. 853–857.
- [73] Yiming Li et al. “Real-time 3D single-molecule localization using experimental point spread functions”. In: *Nature methods* 15.5 (2018), pp. 367–369.
- [74] Manuel F Juetten et al. “Three-dimensional sub-100 nm resolution fluorescence microscopy of thick samples”. In: *Nature methods* 5.6 (2008), pp. 527–529.
- [75] Bo Huang et al. “Three-dimensional super-resolution imaging by stochastic optical reconstruction microscopy”. In: *Science* 319.5864 (2008), pp. 810–813.
- [76] Bo Huang et al. “Whole-cell 3D STORM reveals interactions between cellular structures with nanometer-scale resolution”. In: *Nature methods* 5.12 (2008), pp. 1047–1052.
- [77] Sri Rama Prasanna Pavani et al. “Three-dimensional, single-molecule fluorescence imaging beyond the diffraction limit by using a double-helix point spread function”. In: *Proceedings of the National Academy of Sciences* 106.9 (2009), pp. 2995–2999.
- [78] Yoav Shechtman et al. “Precise three-dimensional scan-free multiple-particle tracking over large axial ranges with tetrapod point spread functions”. In: *Nano letters* 15.6 (2015), pp. 4194–4199.
- [79] Osamu Shimomura, Frank H Johnson, and Yo Saiga. “Extraction, purification and properties of aequorin, a bioluminescent protein from the luminous hydromedusan, *Aequorea*”. In: *Journal of cellular and comparative physiology* 59.3 (1962), pp. 223–239.

- [80] Douglas C Prasher et al. “Primary structure of the *Aequorea victoria* green-fluorescent protein”. In: *Gene* 111.2 (1992), pp. 229–233.
- [81] Martin Chalfie et al. “Green fluorescent protein as a marker for gene expression”. In: *Science* 263.5148 (1994), pp. 802–805.
- [82] Mats Ormö et al. “Crystal structure of the *Aequorea victoria* green fluorescent protein”. In: *Science* 273.5280 (1996), pp. 1392–1395.
- [83] Dmitriy M Chudakov et al. “Fluorescent proteins and their applications in imaging living cells and tissues”. In: *Physiological reviews* 90.3 (2010), pp. 1103–1163.
- [84] James AJ Arpino, Pierre J Rizkallah, and D Dafydd Jones. “Crystal structure of enhanced green fluorescent protein to 1.35 Å resolution reveals alternative conformations for Glu222”. In: (2012).
- [85] GM Cooper. “The Cell: A Molecular Approach 2nd edition Boston University”. In: *Sunderland (MA): Sinauer Associates.[Google Scholar]* (2000).
- [86] Bryan T MacDonald et al. “Disulfide bond requirements for active Wnt ligands”. In: *Journal of Biological Chemistry* 289.26 (2014), pp. 18122–18136.
- [87] Malea Kneen et al. “Green fluorescent protein as a noninvasive intracellular pH indicator”. In: *Biophysical journal* 74.3 (1998), pp. 1591–1599.
- [88] Sean A McKinney et al. “A bright and photostable photoconvertible fluorescent protein”. In: *Nature methods* 6.2 (2009), pp. 131–133.
- [89] Graham T Dempsey et al. “Evaluation of fluorophores for optimal performance in localization-based super-resolution imaging”. In: *Nature methods* 8.12 (2011), pp. 1027–1036.
- [90] Siyuan Wang et al. “Characterization and development of photoactivatable fluorescent proteins for single-molecule-based superresolution imaging”. In: *Proceedings of the National Academy of Sciences* 111.23 (2014), pp. 8452–8457.
- [91] Mike Heilemann et al. “Subdiffraction-resolution fluorescence imaging with conventional fluorescent probes”. In: *Angewandte Chemie International Edition* 47.33 (2008), pp. 6172–6176.
- [92] Sebastian van de Linde et al. “Photoinduced formation of reversible dye radicals and their impact on super-resolution imaging”. In: *Photochemical & Photobiological Sciences* 10.4 (2011), pp. 499–506.
- [93] Graham T Dempsey et al. “Photoswitching mechanism of cyanine dyes”. In: *Journal of the American Chemical Society* 131.51 (2009), pp. 18192–18193.

- [94] Sebastian Van de Linde et al. “Direct stochastic optical reconstruction microscopy with standard fluorescent probes”. In: *Nature protocols* 6.7 (2011), pp. 991–1009.
- [95] Honglin Li and Joshua C Vaughan. “Switchable fluorophores for single-molecule localization microscopy”. In: *Chemical reviews* 118.18 (2018), pp. 9412–9454.
- [96] Markus Sauer and Mike Heilemann. “Single-molecule localization microscopy in eukaryotes”. In: *Chemical reviews* 117.11 (2017), pp. 7478–7509.
- [97] Philip Schaefer et al. “Methylene blue-and thiol-based oxygen depletion for super-resolution imaging”. In: *Analytical chemistry* 85.6 (2013), pp. 3393–3400.
- [98] Ursula Burner, Walter Jantschko, and Christian Obinger. “Kinetics of oxidation of aliphatic and aromatic thiols by myeloperoxidase compounds I and II”. In: *FEBS letters* 443.3 (1999), pp. 290–296.
- [99] Robin Diekmann et al. “Optimizing imaging speed and excitation intensity for single-molecule localization microscopy”. In: *Nature methods* 17.9 (2020), pp. 909–912.
- [100] Bernard Richards and Emil Wolf. “Electromagnetic diffraction in optical systems, II. Structure of the image field in an aplanatic system”. In: *Proceedings of the Royal Society of London. Series A. Mathematical and Physical Sciences* 253.1274 (1959), pp. 358–379.
- [101] Kathleen S Youngworth and Thomas G Brown. “Focusing of high numerical aperture cylindrical-vector beams”. In: *Optics Express* 7.2 (2000), pp. 77–87.
- [102] Omar E Olarte et al. “Light-sheet microscopy: a tutorial”. In: *Advances in Optics and Photonics* 10.1 (2018), pp. 111–179.
- [103] S Grill and EHK Stelzer. “Method to calculate lateral and axial gain factors of optical setups with a large solid angle”. In: *JOSA A* 16.11 (1999), pp. 2658–2665.
- [104] Patrick Terrier, Jean-Michel Charbois, and Vincent Devlaminck. “Fast-axis orientation dependence on driving voltage for a Stokes polarimeter based on concrete liquid-crystal variable retarders”. In: *Applied optics* 49.22 (2010), pp. 4278–4283.
- [105] Tsung-Li Liu et al. “Observing the cell in its native state: Imaging subcellular dynamics in multicellular organisms”. In: *Science* 360.6386 (2018), eaaq1392.
- [106] Thomas Pengo, Seamus J Holden, and Suliana Manley. “PALMsiever: a tool to turn raw data into results for single-molecule localization microscopy”. In: *Bioinformatics* 31.5 (2015), pp. 797–798.

- [107] Claudia Geisler et al. “Drift estimation for single marker switching based imaging schemes”. In: *Optics express* 20.7 (2012), pp. 7274–7289.
- [108] Yina Wang et al. “Localization events-based sample drift correction for localization microscopy with redundant cross-correlation algorithm”. In: *Optics express* 22.13 (2014), pp. 15982–15991.
- [109] S Ritter et al. “Emission properties and photon statistics of a single quantum dot laser”. In: *Optics Express* 18.10 (2010), pp. 9909–9921.
- [110] Nils Gustafsson et al. “Fast live-cell conventional fluorophore nanoscopy with ImageJ through super-resolution radial fluctuations”. In: *Nature communications* 7.1 (2016), pp. 1–9.
- [111] Ted A Laurence and Brett A Chromy. “Efficient maximum likelihood estimator fitting of histograms”. In: *Nature methods* 7.5 (2010), pp. 338–339.
- [112] Donald W Marquardt. “An algorithm for least-squares estimation of non-linear parameters”. In: *Journal of the society for Industrial and Applied Mathematics* 11.2 (1963), pp. 431–441.
- [113] Hazen P Babcock and Xiaowei Zhuang. “Analyzing single molecule localization microscopy data using cubic splines”. In: *Scientific reports* 7.1 (2017), pp. 1–9.
- [114] Steven M Kay. *Fundamentals of statistical signal processing: estimation theory*. Prentice-Hall, Inc., 1993.
- [115] William Hadley Richardson. “Bayesian-based iterative method of image restoration”. In: *JoSA* 62.1 (1972), pp. 55–59.
- [116] Manuel Hüpfel et al. “Wavelet-based background and noise subtraction for fluorescence microscopy images”. In: *Biomedical optics express* 12.2 (2021), pp. 969–980.
- [117] Alvaro Mata, Aaron J Fleischman, and Shuvo Roy. “Characterization of polydimethylsiloxane (PDMS) properties for biomedical micro/nanosystems”. In: *Biomedical microdevices* 7.4 (2005), pp. 281–293.
- [118] Benedetta Bolognesi and Ben Lehner. “Protein overexpression: reaching the limit”. In: *Elife* 7 (2018), e39804.
- [119] Graeme Ball et al. “A cell biologist’s guide to high resolution imaging”. In: *Methods in enzymology*. Vol. 504. Elsevier, 2012, pp. 29–55.
- [120] Nathan C Shaner et al. “Improving the photostability of bright monomeric orange and red fluorescent proteins”. In: *Nature methods* 5.6 (2008), pp. 545–551.

- [121] Panchanan Maiti, Jayeeta Manna, and Michael P McDonald. “Merging advanced technologies with classical methods to uncover dendritic spine dynamics: a hot spot of synaptic plasticity”. In: *Neuroscience research* 96 (2015), pp. 1–13.
- [122] Daniel Routledge and Steffen Scholpp. “Mechanisms of intercellular Wnt transport”. In: *Development* 146.10 (2019), dev176073.
- [123] Ritsuko Takada et al. “Monounsaturated fatty acid modification of Wnt protein: its role in Wnt secretion”. In: *Developmental cell* 11.6 (2006), pp. 791–801.
- [124] Eliana Stanganello and Steffen Scholpp. “Role of cytonemes in Wnt transport”. In: *Journal of cell science* 129.4 (2016), pp. 665–672.
- [125] Eliana Stanganello et al. “Filopodia-based Wnt transport during vertebrate tissue patterning”. In: *Nature communications* 6.1 (2015), p. 5846.
- [126] Felipe-Andrés Ramírez-Weber and Thomas B Kornberg. “Cytonemes: cellular processes that project to the principal signaling center in *Drosophila* imaginal discs”. In: *Cell* 97.5 (1999), pp. 599–607.
- [127] Désirée Spiering and Louis Hodgson. “Dynamics of the Rho-family small GTPases in actin regulation and motility”. In: *Cell adhesion & migration* 5.2 (2011), pp. 170–180.
- [128] Ana-Citlali Gradilla et al. “Exosomes as Hedgehog carriers in cytoneme-mediated transport and secretion”. In: *Nature communications* 5.1 (2014), p. 5649.
- [129] Wolf Heusermann et al. “Exosomes surf on filopodia to enter cells at endocytic hot spots, traffic within endosomes, and are targeted to the ER”. In: *Journal of Cell Biology* 213.2 (2016), pp. 173–184.
- [130] Amin Rustom et al. “Nanotubular highways for intercellular organelle transport”. In: *Science* 303.5660 (2004), pp. 1007–1010.
- [131] Irene Brigger, Catherine Dubernet, and Patrick Couvreur. “Nanoparticles in cancer therapy and diagnosis”. In: *Advanced drug delivery reviews* 64 (2012), pp. 24–36.
- [132] Kevin Letchford and Helen Burt. “A review of the formation and classification of amphiphilic block copolymer nanoparticulate structures: micelles, nanospheres, nanocapsules and polymersomes”. In: *European journal of pharmaceuticals and biopharmaceutics* 65.3 (2007), pp. 259–269.
- [133] Catarina Pinto Reis et al. “Nanoencapsulation I. Methods for preparation of drug-loaded polymeric nanoparticles”. In: *Nanomedicine: Nanotechnology, Biology and Medicine* 2.1 (2006), pp. 8–21.

- [134] Tracy R Daniels et al. “The transferrin receptor and the targeted delivery of therapeutic agents against cancer”. In: *Biochimica et Biophysica Acta (BBA)-General Subjects* 1820.3 (2012), pp. 291–317.
- [135] Claudia Corbo et al. “The impact of nanoparticle protein corona on cytotoxicity, immunotoxicity and target drug delivery”. In: *Nanomedicine* 11.1 (2016), pp. 81–100.
- [136] Gabriele Maiorano et al. “Effects of cell culture media on the dynamic formation of protein- nanoparticle complexes and influence on the cellular response”. In: *ACS nano* 4.12 (2010), pp. 7481–7491.
- [137] Carl D Walkey and Warren CW Chan. “Understanding and controlling the interaction of nanomaterials with proteins in a physiological environment”. In: *Chemical Society Reviews* 41.7 (2012), pp. 2780–2799.
- [138] Tommy Cedervall et al. “Understanding the nanoparticle–protein corona using methods to quantify exchange rates and affinities of proteins for nanoparticles”. In: *Proceedings of the National Academy of Sciences* 104.7 (2007), pp. 2050–2055.
- [139] Andre E Nel et al. “Understanding biophysicochemical interactions at the nano–bio interface”. In: *Nature materials* 8.7 (2009), pp. 543–557.
- [140] Tommy Cedervall et al. “Detailed identification of plasma proteins adsorbed on copolymer nanoparticles”. In: *Angewandte Chemie International Edition* 46.30 (2007), pp. 5754–5756.
- [141] Stefan Tenzer et al. “Rapid formation of plasma protein corona critically affects nanoparticle pathophysiology”. In: *Nano-Enabled Medical Applications*. Jenny Stanford Publishing, 2020, pp. 251–278.
- [142] Ding Cheng Yang et al. “Expression of transferrin receptor and ferritin H-chain mRNA are associated with clinical and histopathological prognostic indicators in breast cancer.” In: *Anticancer research* 21.1B (2001), pp. 541–549.
- [143] Reinhard Prior, Guido Reifenberger, and Wolfgang Wechsler. “Transferrin receptor expression in tumours of the human nervous system: relation to tumour type, grading and tumour growth fraction”. In: *Virchows Archiv A* 416 (1990), pp. 491–496.
- [144] VI Shah et al. “Correlation of transferrin receptor expression with histologic grade and immunophenotype in chronic lymphocytic leukemia and non-Hodgkin’s lymphoma.” In: *Hematologic pathology* 4.1 (1990), pp. 37–41.
- [145] Kazuya Kondo et al. “Transferrin receptor expression in adenocarcinoma of the lung as a histopathologic indicator of prognosis”. In: *Chest* 97.6 (1990), pp. 1367–1371.

- [146] Sanjeeb K Sahoo, Wenxue Ma, and Vinod Labhasetwar. “Efficacy of transferrin-conjugated paclitaxel-loaded nanoparticles in a murine model of prostate cancer”. In: *International journal of cancer* 112.2 (2004), pp. 335–340.
- [147] Sanjeeb K Sahoo and Vinod Labhasetwar. “Enhanced antiproliferative activity of transferrin-conjugated paclitaxel-loaded nanoparticles is mediated via sustained intracellular drug retention”. In: *Molecular pharmaceutics* 2.5 (2005), pp. 373–383.
- [148] Geneviève Gaucher et al. “Block copolymer micelles: preparation, characterization and application in drug delivery”. In: *Journal of controlled release* 109.1-3 (2005), pp. 169–188.
- [149] Neha Shah et al. “Paclitaxel-loaded PLGA nanoparticles surface modified with transferrin and Pluronic® P85, an in vitro cell line and in vivo biodistribution studies on rat model”. In: *Journal of drug targeting* 17.7 (2009), pp. 533–542.
- [150] Wei-hua Ren et al. “Development of transferrin functionalized poly (ethylene glycol)/poly (lactic acid) amphiphilic block copolymeric micelles as a potential delivery system targeting brain glioma”. In: *Journal of Materials Science: Materials in Medicine* 21 (2010), pp. 2673–2681.
- [151] Bruno H Zimm. “Molecular theory of the scattering of light in fluids”. In: *The Journal of Chemical Physics* 13.4 (1945), pp. 141–145.
- [152] Bruno H Zimm. “Apparatus and methods for measurement and interpretation of the angular variation of light scattering; preliminary results on polystyrene solutions”. In: *The Journal of Chemical Physics* 16.12 (1948), pp. 1099–1116.
- [153] Peter N Pusey et al. “Intensity fluctuation spectroscopy of laser light scattered by solutions of spherical viruses. R17, Q. beta., BSV, PM2, and T7. I. Light-scattering technique”. In: *Biochemistry* 13.5 (1974), pp. 952–960.
- [154] Haixia Wang et al. “The protein corona on nanoparticles as viewed from a nanoparticle-sizing perspective”. In: *Wiley Interdisciplinary Reviews: Nanomedicine and Nanobiotechnology* 10.4 (2018), e1500.
- [155] Haixia Wang et al. “Formation of a monolayer protein corona around polystyrene nanoparticles and implications for nanoparticle agglomeration”. In: *Small* 15.22 (2019), p. 1900974.
- [156] Mohamed El Beheiry and Maxime Dahan. “ViSP: representing single-particle localizations in three dimensions”. In: *Nature methods* 10.8 (2013), pp. 689–690.
- [157] A Descloux, Kristin Stefanie Größmayer, and Aleksandra Radenovic. “Parameter-free image resolution estimation based on decorrelation analysis”. In: *Nature methods* 16.9 (2019), pp. 918–924.

- [158] Yih Horng Tan et al. “A nanoengineering approach for investigation and regulation of protein immobilization”. In: *ACS nano* 2.11 (2008), pp. 2374–2384.
- [159] L Bongini et al. “Freezing immunoglobulins to see them move”. In: *Proceedings of the National Academy of Sciences* 101.17 (2004), pp. 6466–6471.
- [160] Susanna M Früh et al. “Site-specifically-labeled antibodies for super-resolution microscopy reveal in situ linkage errors”. In: *ACS nano* 15.7 (2021), pp. 12161–12170.
- [161] Sara A Jones et al. “Fast, three-dimensional super-resolution imaging of live cells”. In: *Nature methods* 8.6 (2011), pp. 499–505.
- [162] Thorsten Wohland et al. “Single plane illumination fluorescence correlation spectroscopy (SPIM-FCS) probes inhomogeneous three-dimensional environments”. In: *Optics express* 18.10 (2010), pp. 10627–10641.
- [163] Bidisha Sinha et al. “Cells respond to mechanical stress by rapid disassembly of caveolae”. In: *Cell* 144.3 (2011), pp. 402–413.
- [164] Volker Middel et al. “Dysferlin-mediated phosphatidylserine sorting engages macrophages in sarcolemma repair”. In: *Nature communications* 7.1 (2016), p. 12875.

Acknowledgements

Many years later, as I recollect the past living in Karlsruhe, I shall be grateful for the blessing of working in an extraordinary biophysics group with brilliant and interesting colleagues. How banal the pursuit of doctoral research would become without countless yet constructive discussions in weekly group seminars. First and foremost, I want to thank Prof. Nienhaus for the opportunity to work in his group. His insight into biology and physics has reshaped my cognition about the meaning of scientific research and the obligation of a scholar, which will have a lifelong influence on my career. His rigorous attitude toward knowledge forced me to dive into the very details of fundamental theories such that I could better understand the essence of nature. Many thanks go to Prof. Lemmer for reviewing my thesis and attending my defense as the first referee.

As my closest coworker, I appreciate Dr. Flatten's kindness in the preparation of biological samples for my experiments. I miss the pleasure moments when we strolled through the little forest and obliviously stopped somewhere, debating about the meaning of existence. I will be proud of those days when we talked about science and social issues, waiting for the running experiment until the next day before dawn. I would like to give credit to all current and ex members of AG Nienhaus for their inspiring advice and help in my research. Special gratitude goes to Dr. Haixia Wang for her dedication and patience in our intensive discussions on the nanoparticle project, which directly led to my fruitful research in the last year. Working on an interdisciplinary topic, I would not have finished the work without enormous hands-on experience in biology, chemistry, and programming, the training of which was given by Dr. Rui Ma, Dr. Antonia Ecker, Ms. Julia Kuhlmann, and Dr. Andrei Kobitski. Many thanks to them.

Apart from my passionate colleagues, I would also give thanks to the technician teams and secretary team in APH. I was amazed by the exquisite mechanical fabrication skills of Mr. Frank Landhauer and the fellows in his workshop. Many thanks for their consistent patience in satisfying my harsh requirements on the quests in four years. Great thanks to Mr. Michael Hippe and his colleagues for helping me out with electronic and IT problems. Whenever I look at the neat artwork of the homemade cell incubation system, it reminds me of the days when I worked together with Frank and Michael. Thanks to Ms. Petra Bauer and her colleagues for the efficiency in processing administrative work.

Life in Karlsruhe is not only about research. Private talking about art, music, and literature during lunchtime with Dr. Gernot Guigas and the tendency of science and technology and their influence on the future of humanity with Manuel Heupfel in the evening was always enjoyable and thought-provoking. The routine rehearsal each Saturday morning with enthusiastic amateur musicians made up my major recreation. Thanks to their encouragement and support, I was able to independently play a part in a small orchestra. I learned how to reconcile with myself, to be humble, and to forgive people in the routine gathering of evangelisch church each Sunday afternoon. I will always take with me wherever I go the graceful hand-transcript poetry advent calendar gifted by my pen pals when I was a lonely nomad in the Nordic wild as it used to be the shimmery light in the endless darkness of the polar night that guide my broken soul to peaceful habitat.

As an expatriate living in Germany, I want to express gratitude to my landlord Mr. and Mrs. Bestek, who treated me with great kindness like their own. While good cares make my daily life at ease, the right direction and decision will assure a prosperous future. Dr. Franco Weth is such a benefactor and mentor I have the privilege to know. His professional and valuable suggestions regarding research and career planning for academia have consolidated my faith in pursuit of a Ph.D. and guided me through the toughest days.

In the end, I want to give special thanks to my reliable and generous friends Sven, Ajarree, and Miyase. The best time I have had throughout those years was with you. I shall never forget the surprise birthday party you organized for me on an ordinary, gloomy Thursday evening. I cherish the tranquil grass picnic on those midsummer afternoons, the delightful Kneipenquartett tours, and the pub crawls we shared together. I cannot appreciate too much your hearkening, and your emotional support, which are always right there. Long live our friendship.

Last but not least, I would like to express my deepest gratitude to my parents Jinwen and Shujing. Without your unconditional love, lifelong support, and encouragement, I could not have gone far. You are the best.

"Love is patient, love is kind. It is not jealous, is not pompous, it is not inflated. It bears all things, believes all things, hopes all things, endures all things."

– 1 Corinthians 13:4, 7. The Bible –